RICE UNIVERSITY

The characterization of coupled plasmonic systems

by

Britain Willingham

A Thesis Submitted
in Partial Fulfillment of the
Requirements for the Degree

Doctor of Philosophy

Approved, Thesis Committee:

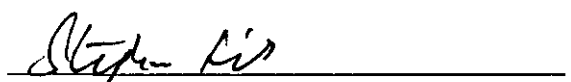

Stephan Link, Chair
Associate Professor of Chemistry,
Associate Professor of Electrical and
Computer Engineering

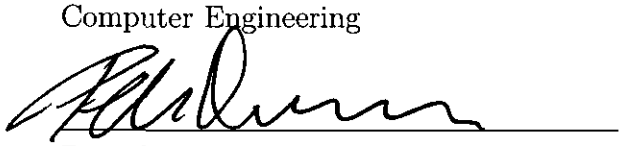

Peter Nordlander
Professor of Physics and Astronomy,
Professor of Electrical and Computer
Engineering

Jason Hafner
Associate Professor of Physics and
Astronomy,
Associate Professor of Chemistry

Houston, Texas

January, 2013

ABSTRACT

The characterization of coupled plasmonic systems

by

Britain Willingham

In this thesis numerical methods are used to understand the individual and collective optical response of metal nanoparticles (MNPs). In particular, finite 1D assemblies of MNPs are characterized by analytical solutions to Maxwell's equations. Small particle solutions such as the well-established *plasmon hybridization* scheme as well as a novel circuit model explaining the intrinsic mechanisms of free electron dynamics help to characterize the optical response of single and coupled MNPs. Complex systems of closely spaced MNPs with small interparticle gaps are studied with the help of full scattering solutions to Maxwell's equations. It is shown that higher order plasmon modes facilitate strong near-fields between MNPs, and in linear chains foster specific optical attributes which are present in more complex systems, playing a key role in energy propagation along practical MNP waveguides.

ACKNOWLEDGEMENTS

I would like to thank the members of my thesis committee: Stephan Link, Peter Nordlander and Jason Hafner. I will always be indebted to Stephan Link for his encouragement, guidance and patience. I would also like to thank Liane Slaughter and the members of Stephan Link's group for providing me with a wonderful and insightful work environment while at Rice.

Finally, my love is extended to Rochelle, Boudicca, Otto, my parents, and last but not least, my sister Bethany. I would not have known what to do without their support.

Contents

Illustrations

Tables

Chapter 1

Introduction

1.1 Motivation

Metal nanoparticles (MNPs) have been around for some time [1,2] and their properties have been well studied and documented within the literature [3,4]. Substantial efforts have shown that MNPs stand as promising components in future optical devices [5,6] with a broad range of applications [7]. From chemical [8] and biological sensing [9] to imaging [10], metamaterials [11–14] and waveguiding [15, 16], the rapid expansion of research in the field of nanophotonics has given rise to an unquestionable need for the optical characterization of MNPs [17]. As experimental techniques capable of systematically imaging and spectroscopically identifying individual [18] as well as collections [19] of MNPs of varying size [20] and shape [21, 22] become better established, a need for theoretical calculations [23] which act to quantify or predict a system's optical properties is necessary.

1.2 Background

Within solid-state physics, the optical response of a metal can be viewed as one which results from intrinsic properties [3] like density [24], static conductivity [25] or the

relaxation of conduction electrons [26]. Absent microscopic theories based upon the atomic morphology of metals [27,28] or the periodic nature of its crystallinity [29,30], our knowledge of a metal's internal structure is predominantly phenomenological [31]. Optical measurements on thin metallic films [32–35] have helped to establish the bulk metallic or macroscopic variables which on average represent these microscopic properties. Surprisingly, when considering a cluster of the same atoms forming a MNP of sufficient size (larger than about 10 nm) [3], the representation of intrinsic mechanisms by the use of bulk properties has resulted in remarkable agreement between experimental measurements and theoretical predictions [17, 21, 36]. As MNP sizes diminish [37], the macroscopic picture must give way to more appropriate quantum descriptions [38–40]. Nevertheless, the difficulty in deciphering optical measurements which include artifacts from quantum mechanical effects [41] is unnecessary when an accurate depiction of a MNP's optical response can be produced by purely classical means [42]. Therefore, development of simple classical models [43, 44] and solutions [2, 4] that result in optical spectrum consistent with experimental measurements, yet which sidestep the difficulties surrounding self-consistent solutions to Schrödinger's equation, is of substantial use for future studies.

Though the importance of a metal's intrinsic response to light cannot be stressed enough, in the fields of nanophotonics and plasmonics a large interest is in the design of MNPs to redirect [45] and harness [46] light at specific wavelengths. Extrinsic effects [3] which occur by tuning a MNP's size and shape as well as its local en-

vironment [47–49] allow for variable usability in materials and applications. Prime examples are well known, one of which is stained glass [50], where color variations occur due to viewing scattered light at angles different from light transmission, where wavelengths are absorbed by an embedded MNP matrix. Photo-thermal cancer treatments [51, 52] also take advantage of MNP's unique extrinsic properties. Here, large absorption cross-sections [53] lead to heat generation [54], precise targeting, and subsequent destruction of harmful tissue.

A common theme underlying the optical properties of MNPs of different shape, size, and composition is the established notion that they are dominated by the collective response of the metal's conduction electrons [24]. Electromagnetic waves incident on a MNP surface act to set up coherent oscillations of loosely bound electrons, analogous to a periodically driven damped harmonic oscillator [55], or the current response of an RLC-circuit [56]. These resonance phenomena, termed *plasmons* [32, 57], efficiently convert optical energy to mechanical motion [15] and when driven at the correct frequency lead to peaks in the absorption spectrum which has a profile determined by the intrinsic structure of the MNP in question.

A simple classical model of a MNP is to consider its size to be much smaller than the incident wavelength of light [58], and for its intrinsic mechanisms to be governed by the bulk metallic response. Here, phase retardation due to the finite size of the MNP as well as radiative reaction forces [59] due to the momentum of emitted photons [60] play an insignificant role, whereby the energy contained within magnetic

fields is completely neglected. The electrostatic equations [61] which govern the optical properties of MNPs within this quasi-static or Rayleigh regime [4] result in a picture of plasmons painted as self-sustained deformations of an incompressible and irrotational electron gas [62]. Owing to this incompressible nature, the effect of such deformations results in the appearance of a finite charge density at the MNP surface. When driven by optical means, these localized surface plasmons are responsible for the electric fields located near MNP boundaries. As will be shown in chapter 2, Coulombic interactions between oscillating surface charges resulting from MNP plasmon modes placed in close proximity to one another facilitates strong absorption of light, often at multiple frequencies corresponding to *hybridization* between the primitive plasmon modes [44, 62, 63]. At MNP junctions this strong absorption precludes intense electromagnetic near-fields which show a strong dependence upon junction size, interparticle distance as well as MNP shape [64].

As will be shown in chapter 3, small particle solutions based on the electrostatic limitations [65] previously mentioned offer keen insight into factors which can dictate the dynamics of both single and coupled MNP plasmons. However, as MNP sizes grow the quasi-static assumptions, where near-fields constitute the only means of interaction, begin to lose their validity [66]. Oscillating charge gives rise to time-dependent current density which varies spatially. Finite dipoles [67] as well as higher order electric and magnetic modes now occur, and have amplitudes that depend not only on the MNP shape but also size. Coulomb fields are replaced with full vec-

tor wave functions [68] which describe propagating transverse waves emanating from each MNP [69]. These radiative interactions enable many of todays nanophotonic applications under study. Fano line-shapes [70,71] seen in ring-disk structures [72,73] (among others) [74] are thought to rely on the interaction of a localized plasmon mode with that of the hybridized structure's scattering pseudo-continuum while gaps within split-ring resonators [75] and satellite structures [76] result in circular displacement current [77], giving rise to optical moments able to magnetically couple to incident light. In chapter 4, scattered fields will also be shown to play a key role in receiving and transporting optical information below light's diffraction limit [78]. Here, transmission lines composed of MNPs propagate energy via evanescent near-fields by maximizing the hybridization between higher order modes [63], while suppressing the loss due to far-field scattering from a waveguide's dipole response [79].

Many practical applications, such as surface enhanced spectroscopies [80], derive from a nanostructure's ability to localize energy and enhance fields between junctions formed by constituent MNPs. To maximize the advantage of this unique artifact, experiments which include a bottom-up [81–83] approach are used to place closely spaced, chemically synthesized MNPs into complex structures. Using templates constructed by top-down methods [84, 85], pre-designed formations of MNPs can then harness the strong plasmonic coupling and unique optical properties [19] of self-assembled [86–88], closely packed MNP systems. To quantify the plasmonic nature of these systems, dark-field scattering [89] and photo-thermal absorption ex-

periments [90] are used to measure their optical response. Numerical methods such as grid based solutions to Maxwell's equations like the finite-difference-time-domain (FDTD) method [91] are often looked upon to predict or characterize the nature of spectral peaks, scattering intensities, or near-field enhancements within MNP assemblies [92]. For systems of limited size and complexity FDTD often well describes their observed optical response, but for larger systems is incapable of performing such calculations due to the large amount of resources required for their execution. Here, analytical scattering solutions [93], which have been proven to be robust within single MNP studies [17] offer swift solutions to Maxwell's equations, and in chapters 4 and 5 will be used to optically characterize large ensembles of MNPs [94] as well as perform full waveguiding simulations of energy transport along collections numbering in the thousands of MNPs [6].

1.3 Specific aims

The objective of this work is to characterize the optical properties of finite 1D assemblies of MNPs of different size, shape and arrangement using classical methods based upon analytical solutions to Maxwell's equations.

1.4 Overview

This thesis contains chapters that are based on journal publications/submissions relevant to the research topic. In chapter 2 a quasi-static solution to the dynamics of

surface plasmons within the *plasmon hybridization* scheme is used to characterize the optical properties of single and coupled nanorods. In chapter 3, a circuit model of MNPs is presented and used to further identify dynamic parameters such as the decay time of surface plasmons as well as a brief example of proximity effects on the optical response of touching MNPs. In chapter 4 we consider the effects of scattering on larger MNPs arranged in linear chains and in positions determined by experiment, identifying optical characteristics which shape the outcome of a MNP waveguide's response. Finally, in chapter 5 we identify the mechanism which leads to long propagation lengths along linear 1D chains and determine the effects of local disorder on the transfer of energy via near-fields within waveguiding structures.

Chapter 2

Plasmon hybridization of nanorod dimers[1]

In this chapter we first review the general theory behind the plasmon hybridization (PH) scheme for a MNP. We then investigate the dynamics of a tunable nanorod which we define as an ellipsoidal of revolution with both longitudinal and transverse plasmons. Using these primitive plasmon modes, we characterize the optical response of a nanorod dimer in both parallel and axial arrangments, showing excellent agreement with the grid based, finite-difference-time-domain (FDTD) method. The dimer plasmon modes are found to depend sensitively on separation between the nanorods and on their relative spatial orientation. Electric fields are calculated and show sensitivity to geometry, with stronger hybridization leading to larger enhancements of the near-field.

2.1 Why do we need tunable MNPs?

An important topic in plasmonics is the design of MNPs capable of providing large electric field enhancements, i.e. "hot spots", for Surface Enhanced Spectroscopies (SES) [95]. The two major physical mechanisms contributing to the electric field

[1] This chapter is based upon the manuscript entitled "Plasmon hybridization in nanorod dimers" by Britain Willingham, Daniel Brandl, and Peter Nordlander, published in Appl. Phys. B **93,** 209-216 (2008).

enhancements are plasmonic and lightning rod effects [96]. The plasmonic enhancement occurs only for wavelengths near the plasmon energies of the MNP, while the lightning rod contributions take place at long wavelengths where metallic screening effectively expels electric fields from the interior of the nanostructure, concentrating them onto their surfaces [96]. In designing efficient substrates for SES applications one must consider tuning the plasmon energies to wavelengths where the spectroscopy and analyte are optically active, and optimizing the structure for the largest possible electric field enhancements.

A metallic nanorod (NR) is an example of a highly tunable MNP [97–99], with surface plasmon energies which depend upon the aspect ratio of the NR, i.e. the ratio of the major to minor axes [100]. NRs possess plasmon resonances in both the longitudinal and transverse directions and give rise to large field enhancements at their tips [101]. By considering a simple nanoparticle dimer system [102, 103], hot spots [104] resulting from strong plasmonic coupling between two adjacent MNPs can be easily studied.

2.2 Theory

The PH method [62] along with several applications has been well established [105], and applied to particles that can be defined in general curvilinear coordinates [106]. Briefly, the plasmons of an individual nanoparticle are considered to be incompressible deformations of the conduction electron distribution with respect to the particle's

oppositely charged positive background. The charge densities, n_o, are assumed uniform and the positive background is polarizable with a high-frequency permittivity, ε_∞. The nanoparticle is thought to be embedded in a dielectric medium with permittivity ε_m. With the displacement of the conduction fluid, surface charges are induced. These provide an electrostatic restoring force which together with the kinetic energy of the electrons determine the plasmon energies. The deformation fields of the conduction electrons can be obtained from a hydrodynamic scalar potential η which satisfies Laplace's equation in a suitable coordinate system. For nanoparticles that can be described in completely separable curvilinear coordinates η can be written as [106],

$$\eta = \sum_{i,j} \left[\dot{S}_{ij}(t) F^1_{ij}(r_1) + \dot{C}_{ij}(t) G^1_{ij}(r_1)\right] F^{23}_{ij}(r_2, r_3) \tag{2.1}$$

with r_1, r_2, and r_3 representing the three curvilinear coordinates, and where i, j label the primitive plasmon modes. The time-dependent variables S_{ij} and C_{ij} describe the amplitudes of the deformation field associated with primitive solid particle and cavity plasmon modes, respectively. In the present application solid particles will be considered, and for this case there is no hybridization between core and cavity plasmons. Therefore the plasmonic eigenmodes of the system are only described by the amplitudes, S_{ij}.

As a consequence of the incompressibility of the electron gas, its deformation gives rise to surface charges. For a nanoparticle with an outer surface that can be defined

as $r_1 = r_o$, the surface charge takes the form,

$$\sigma(r_{23}, t) = \frac{n_o e}{h_1(r_o)} \sum_{i,j} \left. \frac{\partial F^1_{ij}}{\partial r_1} \right|_{r_1 = r_o} F^{23}_{ij}(r_{23}) S_{ij}(t) \tag{2.2}$$

where e is the electronic charge, r_{23} denotes the combination of the r_2 and r_3 coordinates, and h_1 is defined by the metric of the coordinate system [107]. The induced electrostatic potential has the form

$$\Phi_{tot} = \sum_{i,j} \left[A_{ij} F^1_{ij}(r_1) + B_{ij} G^1_{ij}(r_1) \right] F^{23}_{ij}(r_{23}), \tag{2.3}$$

where the coefficients A_{ij} and B_{ij} can be calculated from the continuity of the electrostatic potential at the surface and the discontinuity of the displacement field at a dielectric interface,

$$\sigma = \frac{1}{4\pi h_1} \Big(\varepsilon_\infty \left. \frac{\partial \Phi_{in}}{\partial r_1} \right|_{r_1 = r_o} - \varepsilon_m \left. \frac{\partial \Phi_{out}}{\partial r_1} \right|_{r_1 = r_o} \Big). \tag{2.4}$$

The Lagrangian for the primitive plasmon modes can be expressed in terms of renormalized plasmon amplitudes, $x_{ij} \propto S_{ij}$, as [106],

$$L = \frac{1}{2} n_o m_e \sum_{i,j} \left[\dot{x}^2_{i,j} - \omega^2_{i,j} x^2_{i,j} \right], \tag{2.5}$$

where the energy of the plasmon resonances have the form,

$$\omega^2_{i,j} = \omega^2_B \frac{G^1_{ij}(r_o) \frac{\partial F^1_{ij}}{\partial r_o}}{\varepsilon_\infty G^1_{ij}(r_o) \frac{\partial F^1_{ij}}{\partial r_o} - \varepsilon_m F^1_{ij}(r_o) \frac{\partial G^1_{ij}}{\partial r_o}}. \tag{2.6}$$

In this expression $\omega_B = \sqrt{4\pi e^2 n_0 / m_e}$ is the bulk plasmon frequency of the metal expressed in terms of the effective mass m_e of the conduction electrons.

For an ensemble of interacting nanoparticles the total Lagrangian is equal to the sum of the Lagrangian for each nanoparticle plus an interaction term, $V_{int} = \sum_{q \neq k} V_{kq}$ where

$$V_{kq} = \frac{1}{2} \iint_S \Phi_k \sigma_q \, \mathrm{dS}_q \tag{2.7}$$

describes the Coulomb interaction between the primitive plasmons on particles q and k. In the presence of this interaction, the individual nanoparticle plasmons are no longer eigenmodes of the system but can be considered as primitive plasmon modes that will interact, hybridize, and form collective normal modes.

2.3 Results

In this section we present results for individual NRs and interacting NR dimers. The NRs are modeled using a bulk plasma frequency of $\hbar\omega_B = 9.5$ eV and a dielectric background of $\varepsilon_\infty = 5.0$, as appropriate for silver. Except where otherwise stated, the nanoparticles have a constant ratio of major ($= a$) to minor ($= b$) axis, $\zeta = 10/3$, and are embeded in vacuum, i.e. $\varepsilon_m = 1.0$.

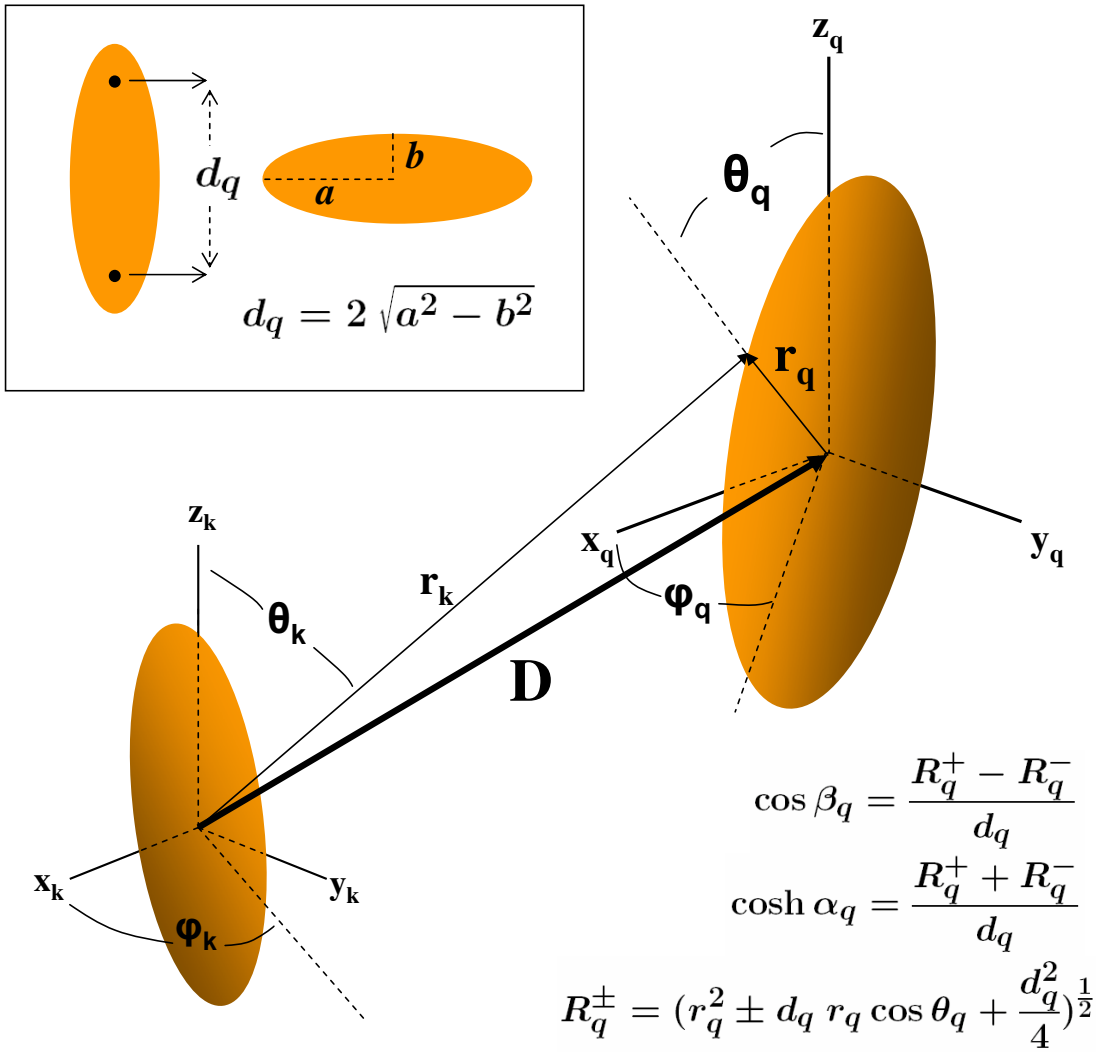

Figure 2.1 : Schematic showing two NRs k and q in a general configuration. The equations show how spherical coordinates for NR q $(r_q, \theta_q, \varphi_q)$ are related to their respective prolate coordinates $(\alpha_q, \beta_q, \varphi_q)$, where φ is the same in both prolate and spherical representations.

2.3.1 Plasmonic properties of individual nanorods

As shown in Fig. 2.1, in prolate spheroidal coordinates the Cartesian coordinates of the q^{th} MNP can be expressed as

$$\begin{aligned} x_q &= \tfrac{1}{2} d_q \sinh\alpha_q \sin\beta_q \cos\phi_q \quad 0 \le \alpha_q < \infty \\ y_q &= \tfrac{1}{2} d_q \sinh\alpha_q \sin\beta_q \sin\phi_q \quad 0 \le \beta_q \le \pi \\ z_q &= \tfrac{1}{2} d_q \cosh\alpha_q \cos\beta_q \qquad\quad 0 \le \phi_q \le 2\pi. \end{aligned}$$

By setting $\alpha_q = \alpha_q^o$, a surface is defined by a set of parametric equations in β_q and ϕ_q which are obtained from

$$\frac{x_q^2 + y_q^2}{b_q^2} + \frac{z_q^2}{a_q^2} = 1, \tag{2.8}$$

where a_q and b_q are related to the inter-focal distance d_q by the relations:

$$a_q = \tfrac{1}{2} d_q \cosh\alpha_q^o, \quad b_q = \tfrac{1}{2} d_q \sinh\alpha_q^o, \quad d_q = 2\sqrt{a_q^2 - b_q^2}.$$

For a solid prolate particle, the functions in Eq. (2.3) are spheroidal harmonics and Legendre functions of the first and second kind, i.e. $F_{ij}^1(r_1) = P_l^m(\cosh\alpha)$, $G_{ij}^1(r_1) = Q_l^m(\cosh\alpha)$ and $F_{ij}^{23}(r_{23}) = \mathrm{Y}_{lm}(\beta, \phi)$. With these substitutions, the plasmon modes of an individual NR can be evaluated directly from Eq. (2.6).

Fig. 2.2 shows the $l = 1 - 5$ plasmon energies of an individual NR for longitudinal ($m = 0$) and transverse ($m = 1$) polarization as a function of aspect ratio. For the longitudinal mode we observe a large monotonous redshift with increasing aspect ratio. For the dipole mode ($l = 1$), this redshift can be understood simply as a reduction in magnitude and an increased separation of the surface charges on the opposite ends of the NR with increasing aspect ratio [106].

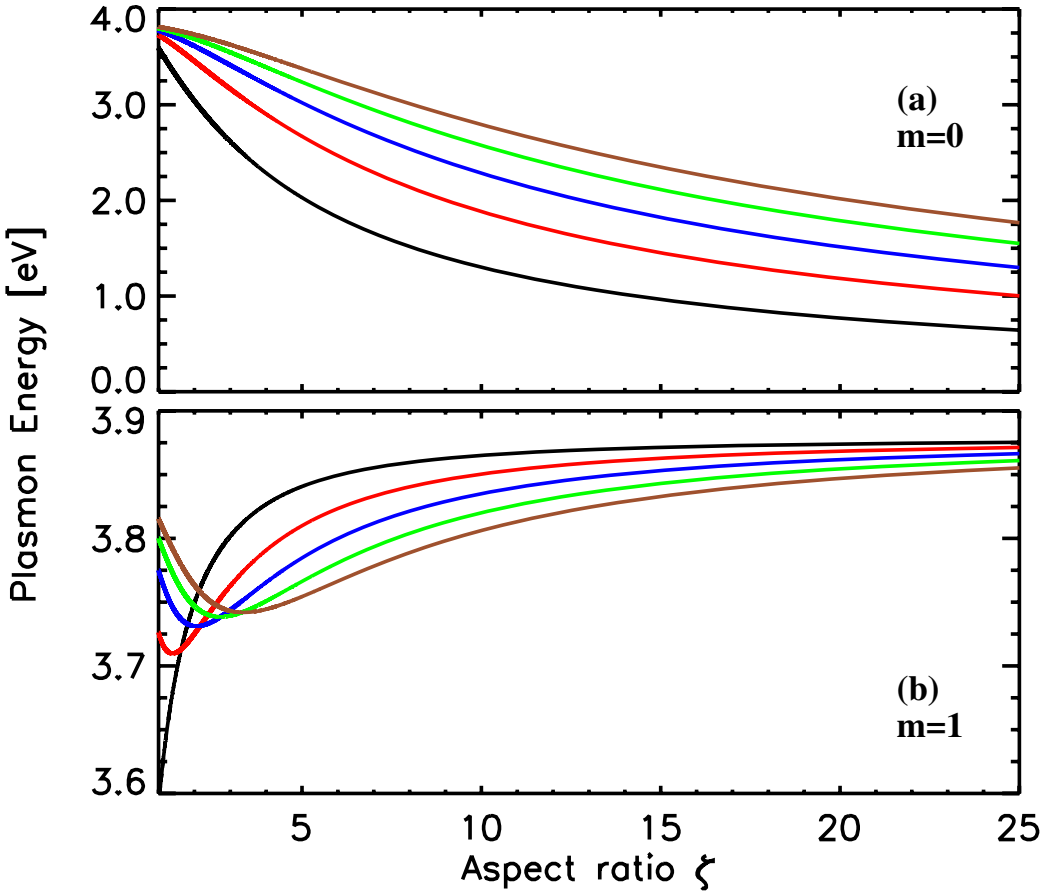

Figure 2.2 : Longitudinal **(a)** and transverse **(b)** plasmon resonances of a prolate silver NR for $l = 1$ (black), 2 (red), 3 (blue), 4 (green), 5 (brown) as a function of aspect ratio.

For transverse polarization, the plasmon modes exhibit a weaker dependence on aspect ratio and show a qualitatively different trend. The dipolar mode exhibits a steady blueshift for increasing aspect ratio which can be physically understood using the same argument as for the longitudinal mode. The higher multipolar modes $l \geq 2$ show a more complex behavior with initial redshifts and then blueshifts as a function of aspect ratio. This behavior is due to the more complex surface charge distributions associated with multipolar NR plasmons.

2.3.2 Plasmonic properties of nanorod dimers

In this section we consider two NRs at arbitrary positions whose respective origins are separated by a distance D as shown in Fig. 2.1. We will discuss the plasmonic properties of a NR dimer in an axially symmetric (AS) configuration where the dimer exhibits cylindrical symmetry with an interparticle junction of lateral width $2b$ and thickness $D-2a$. We will also study a NR dimer in parallel alignment (PA) where the NRs are placed next to each other with a junction of lateral width $2a$ and thickness $D-2b$. Only NRs of identical aspect ratio will be considered, where each Lagrangian contains primitive plasmon modes up to $l_{max} = 25$ from the expansion of Eq. (2.1), insuring sufficient convergence of all quantities considered.

For two NRs in arbitrary positions, the total electrostatic potential can be expressed as a sum of the individual potentials from each NR, $\Phi = \sum_{k=1,2} \Phi_k$ where

$$\Phi_k = \frac{4\pi}{\sinh \alpha_k^o} \sum_{l,m} \frac{R_l^m(\alpha_k^o, \alpha_k)}{W_l^m(\alpha_k^o)} \mathrm{Y}_{lm}(\Omega_k) \tilde{\tau}_{lm,k} \tag{2.9}$$

and

$$R_l^m(\alpha^o,\alpha) = \begin{cases} Q_l^m(\cosh\alpha^o)P_l^m(\cosh\alpha), & \alpha \le \alpha^o \\ P_l^m(\cosh\alpha^o)Q_l^m(\cosh\alpha), & \alpha \ge \alpha^o. \end{cases}$$

The total surface charge distribution for the k^{th} NR, $\tilde{\tau}_{lm,k}$ can be obtained from the discontinuity of the displacement field across the boundaries of the prolate given by Eq. (2.2) and Eq. (2.4). By projecting the continuity equation onto the multipolar components [108] we obtain,

$$\begin{aligned} \tilde{\sigma}_{n\mu,q} &= [\varepsilon_\infty Q_n^\mu(\alpha_q^o)\frac{\partial P_n^\mu}{\partial\alpha_q^o} - \varepsilon_m P_n^\mu(\alpha_q^o)\frac{\partial Q_n^\mu}{\partial\alpha_q^o}]\frac{\tilde{\tau}_{n\mu,q}}{W_n^\mu(\alpha_q^o)} \\ &+ \frac{(\varepsilon_\infty-\varepsilon_m)}{\sinh^2(\alpha_k^o)}\sum_{l,m}\frac{P_l^m(\alpha_k^o)}{W_l^m(\alpha_k^o)}(\frac{\partial}{\partial\alpha_q}J_{ln}^{m\mu})\tilde{\tau}_{lm,k} \end{aligned} \tag{2.10}$$

where $W_l^m(\alpha^o)$ is the Wronskian of the Legendre functions of the first and second kind [109] and $J_{ln}^{m\mu}$ is an interaction term given by,

$$J_{ln}^{m\mu} = \iint_\Omega Q_l^m(\gamma_k)\mathrm{Y}_{lm}(\Omega_k)\mathrm{Y}_{n\mu}(\Omega_q)\,d\Omega_q \tag{2.11}$$

The arguments of the k^{th} NR, $\gamma_k = \cosh(\alpha_k(\Omega_q))$ and $\Omega_k = \Omega_k(\Omega_q)$ are functions of the given solid angle of the q^{th} NR, which the integral of the surface charge is taken over. From Eq. (2.2), the induced surface charge on particle q is given by

$$\begin{aligned} \sigma_q &= \sum_{n,\mu}\tilde{\sigma}_{n\mu,q}\mathrm{Y}_{n\mu}(\Omega_q) \\ &= \sum_{n,\mu}\beta_n^\mu x_{n\mu,q}\mathrm{Y}_{n\mu}(\Omega_q) \end{aligned} \tag{2.12}$$

Using Eqs. (2.7), (2.9) and (2.12) we can write the electrostatic interaction between

particles k and q as a superposition of oscillating modes [108].

$$V_{kq} = \sum_{l,m} \sum_{n,\mu} x_{n\mu,q} \beta_n^\mu A_{ln}^{m\mu} \tilde{\tau}_{lm,k} \tag{2.13}$$

with

$$\beta_n^\mu = \; n_o e \sqrt{\frac{2\frac{\partial P_n^\mu}{\partial \alpha_q^o}}{d_q P_n^\mu(\alpha_q^o)}} \tag{2.14}$$

and

$$A_{ln}^{m\mu} = \; 2\pi d_q \, \frac{\sinh \alpha_q^o}{\sinh \alpha_k^o} \frac{P_l^m(\alpha_k^o)}{W_l^m(\alpha_k^o)} \, J_{ln}^{m\mu} \tag{2.15}$$

Here $l(n)$ and $m(\mu)$ are the multipolar indices of each individual particle $k(q)$ in the system, while $\alpha_{k(q)}^o$ represents evaluation at $\cosh(\alpha_{k(q)}^o)$.

2.3.3 Axially symmetric configuration

For the AS orientation, the Lagrangian is diagonal in the azimuthal index m. Hence, the interaction term given by Eq. (2.11) is simplified by setting $m = \mu$ for all primitive modes.

Fig. 2.3 shows the NR dimer plasmon energies as a function of interparticle separation for longitudinal and transverse polarization. For large separations, the effective coupling between NRs is weak, and the dimer modes are essentially bonding and antibonding combinations of NR plasmons of the same index, l. Since the interparticle interactions decrease rapidly with multipolar index l, the splitting between bonding and antibonding modes decrease with increasing l. As the dimer separation decreases, the interactions between primitive modes of different l increase resulting in significantly hybridized dimer modes. We will refer to such hybridized dimer modes with

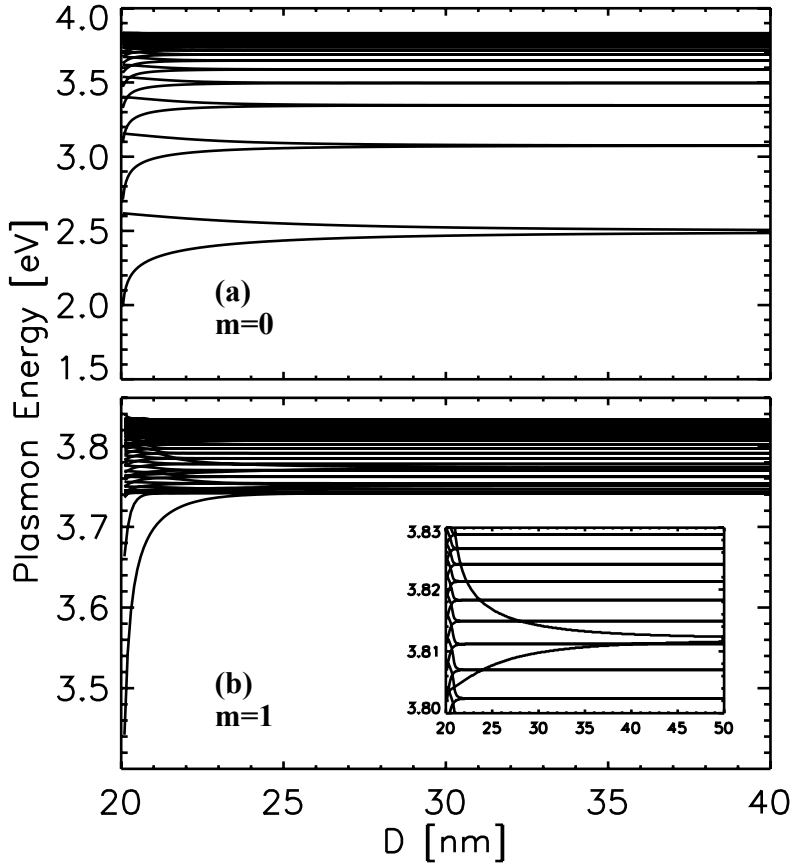

Figure 2.3 : Calculated longitudinal **(a)** and transverse **(b)** plasmon energies as a function of interparticle separation for a silver NR dimer for the AS configuration. The curves illustrate the bonding and anti-bonding dimer plasmons derived from individual primitive plasmon energies of a single NR. The inset in **(b)** is a close-up around the l=1, m=1 hybridized modes.

the multipolar index l to which they correspond in the limit of large separation. The hybridization with higher l modes can most clearly be seen for the dipolar dimer plasmon for longitudinal polarization where the bonding-antibonding splitting becomes noticeable asymmetric for short separation. However, the asymmetry is lower than for a nanosphere or nanoshell dimer [108], indicating that the hybridization with higher l modes is weaker in the NR system. As in the case for a nanosphere dimer the bonding resonance has parallel orientation of the dipole moments while the antisymmetric mode has anti-parallel alignment making this mode dark [108].

For transverse polarization $m = 1$ (Fig. 2.3b), the NR dimer behaves quite differently from a nanosphere dimer. For the aspect ratio $\zeta = 10/3$, the dipolar NR mode is not the lowest energy mode (Fig. 2.2) but lies between the $l = 16$ and $l = 17$ modes. The lowest energy NR mode is the l=5. The interactions with the $2 < l < 16$ modes thus blueshifts the hybridized dipolar dimer modes causing an upward asymmetry of the dipolar bonding and antibonding dimer modes. As in the case of a sphere dimer the plasmonic interactions for transverse polarization are weaker than for longitudinal polarization and the bonding plasmons are dark [48].

In Fig. 2.4 we compare the optical absorption $\sigma(\omega)$ calculated using PH and FDTD [110] for different dimer separations. The curves agree very well. For longitudinal polarization, the major absorption feature is the bonding dipolar resonance discussed in Fig. 2.3a. The weak feature that appears around 3 eV for the shortest dimer separation is the quadrupolar dimer resonance which become dipole active due to the

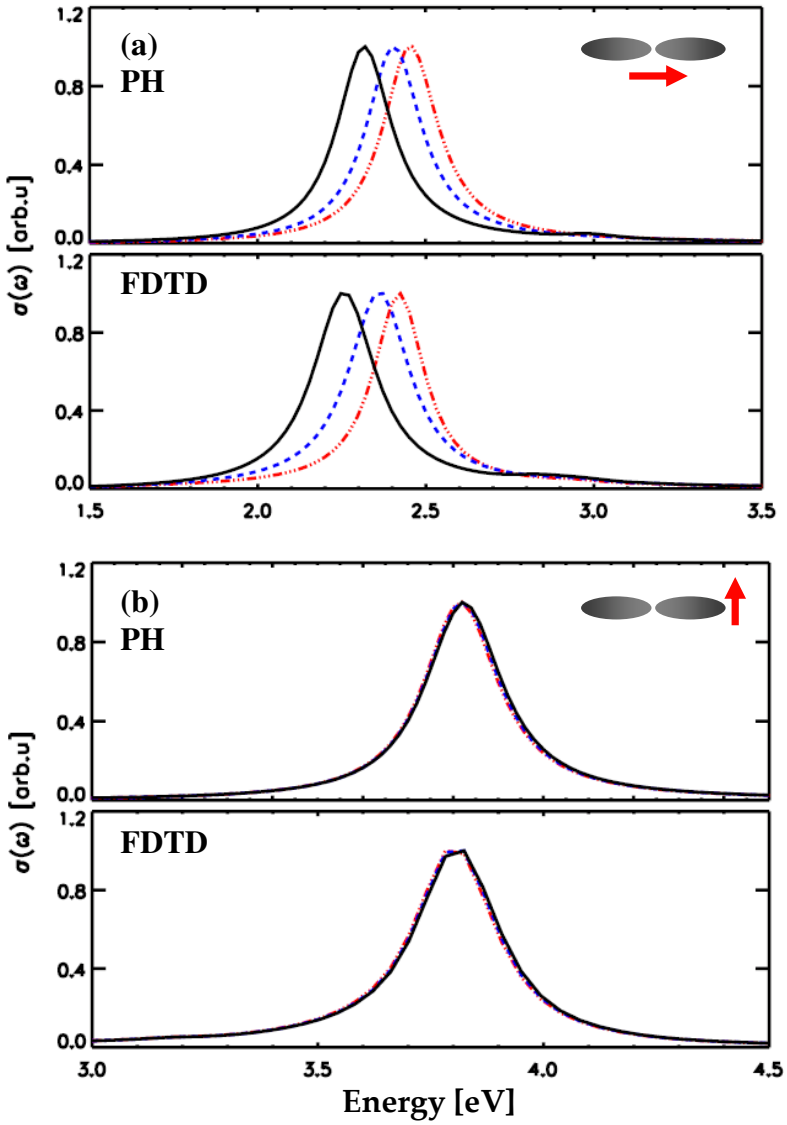

Figure 2.4 : Comparison of the optical absorption for a silver NR dimer in the AS configuration calculated using PH and FDTD for longitudinal **(a)** and transverse **(b)** polarizations as denoted by the arrows. The dimer separations are $D = 21$ nm (solid), $D = 23$ nm (dashed) and $D = 27$ nm (dot-dashed). The absorption curves are calculated using a damping δ=0.1 eV and have been normalized.

hybridization with the dipolar modes. For transverse polarization, the peak is the antibonding dipolar transverse mode shown in the inset in Fig. 2.3b.

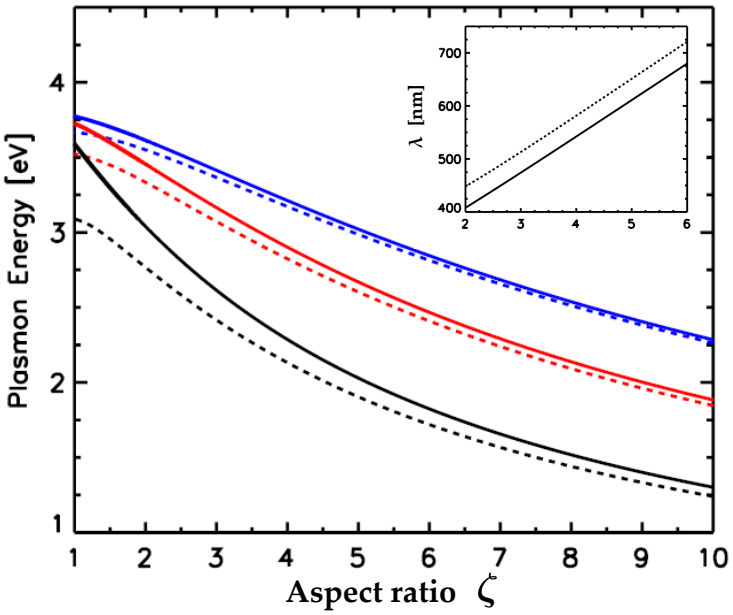

Figure 2.5 : Comparison of the longitudinal $l = 1$ (black), 2 (red), and 3 (blue) modes for an individual silver NR (solid) and a NR dimer in the AS configuration (dashed) as a function of aspect ratio. The major axis is kept constant at a=10 nm, and for the dimer the separation is D=21 nm. The inset is a plot of the wavelengths of the l=1 modes for smaller spans of ζ.

To further investigate how the hybridization in a NR dimer is influenced by the aspect ratio of the NR, in Fig. 2.5 we compare the lowest order longitudinal dimer resonances with the corresponding individual NR modes for a fixed dimer separation but different aspect ratios. The figure shows that the hybridization decreases for higher order multipolar l modes and with increasing aspect ratio, with the sphere dimer $\zeta = 1$ exhibiting the largest shifts. The reduction of the hybridization for a NR of large aspect ratio is due to the reduction of the surface charges at their tips

with increasing aspect ratio. The inset in Fig. 2.5 is a close-up of the wavelengths of the dipolar NR and NR dimer modes as a function of aspect ratio and shows a linear trend in agreement with previous studies. [100].

2.3.4 Parallel configuration

The plasmon hybridization for the PA configuration of two NRs is quite complicated due to the fact that primitive plasmons of different azimuthal m can interact and hybridize. Thus the interaction term Eq. (2.11) is no longer diagonal in m and μ. The optical properties will be determined by the admixture of the primitive dipolar plasmons in the hybridized NR dimer modes. As shown in Fig. 2.2, for an aspect ratio of $\zeta = 10/3$ the three lowest energy primitive plasmon modes are the longitudinal $l = 1-3$ NR modes. These modes lie significantly below the transverse modes and will therefore predominantly interact with each other and determine the optical spectra for longitudinal polarization.

In Fig. 2.6 we show the energy of the hybridized $l = 1 - 3$ modes as a function of dimer separation. For longitudinal polarization the strongest optically active modes are the antibonding dipolar NR dimer modes which blueshift with decreasing dimer separation. These modes are mostly longitudinal ($m = 0$) in nature. As will be discussed below, the bonding $l = 2$ NR dimer mode contains a small admixture of primitive $m = 1$, $l = 1$ plasmons.

For transverse polarization, light will couple into the NR dimer through the prim-

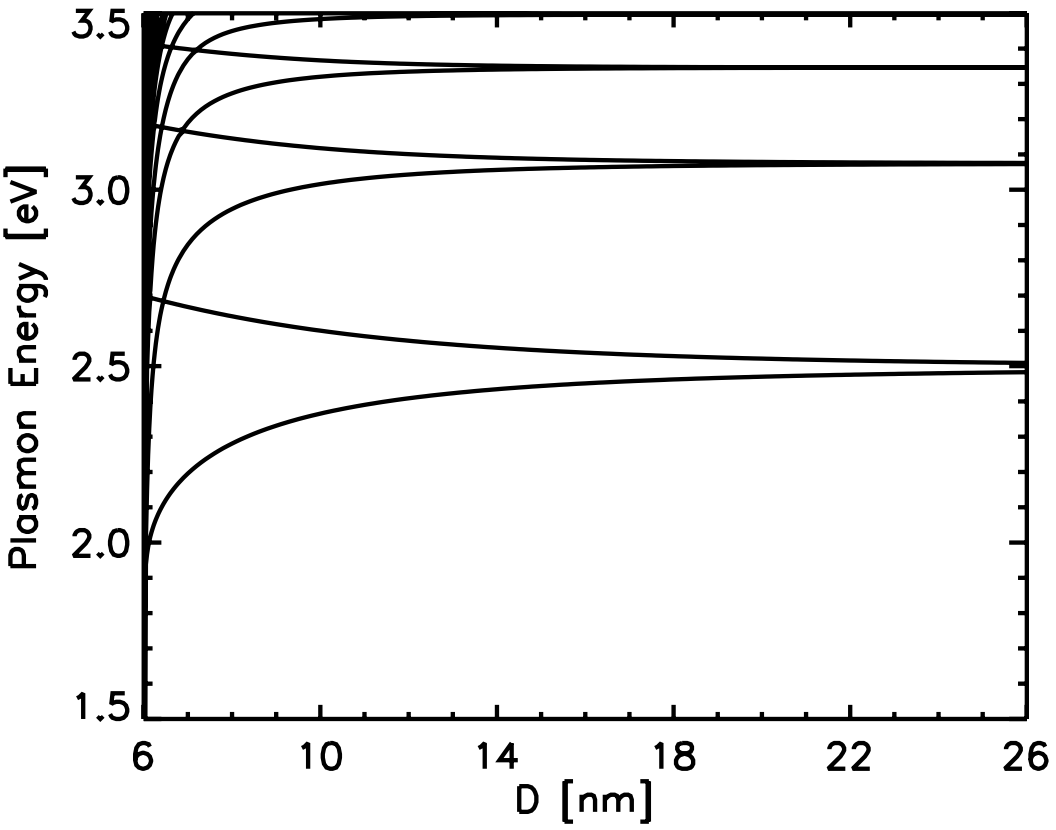

Figure 2.6 : Calculated dimer plasmon energies for a silver NR dimer as a function of interparticle separation for the PA configuration. The curves show the $l = 1 - 3$ bonding and anti-bonding longitudinal dimer plasmons derived from individual primitive plasmon energies of an individual NRs for polarization parallel to the long-axis.

itive $m = 1$, $l = 1$ plasmons around 3.8 eV. Due to the enlarged lateral width of the junction compared to the AS configuration, the interaction between the primitive plasmons on the two NRs will be much stronger and result in a multitude of dipole-active, higher order, multipolar NR dimer modes.

In Fig. 2.7 we compare the optical absorption calculated using PH and FDTD for different dimer separations and polarizations. As for the AS configuration the curves agree very well with each other. For longitudinal polarization, the major absorption feature is the antibonding dipolar resonance discussed in Fig. 2.6.

For transverse polarization the hybridization is more complex. For the largest separations, the peak is a pure bonding $m = 1$ dipolar dimer mode. As D is decreased this mode redshifts and exhibits significant avoided crossings with many of the $l > 2$, $m = 1$ modes. For the shortest separation, the spectrum displays two features. The weak resonance around 2.8 eV is the hybridized bonding $l = 2$ mode mentioned in Fig. 2.6. As illustrated in the inset, the primitive $m = 0$, $l = 2$ mode can interact with the primitive $m = 1$, $l = 1$ mode of an adjacent NR. The resulting hybridization makes this mode excitable also for transverse polarization. The broad asymmetrical feature around 3.7 eV consists of several strongly hybridized dimer modes as illustrated by the dotted line. The three dominant peaks at 3.6, 3.7, and 3.8 eV all contain significant admixtures of primitive $m = 1$, $l = 1 - 5$ modes.

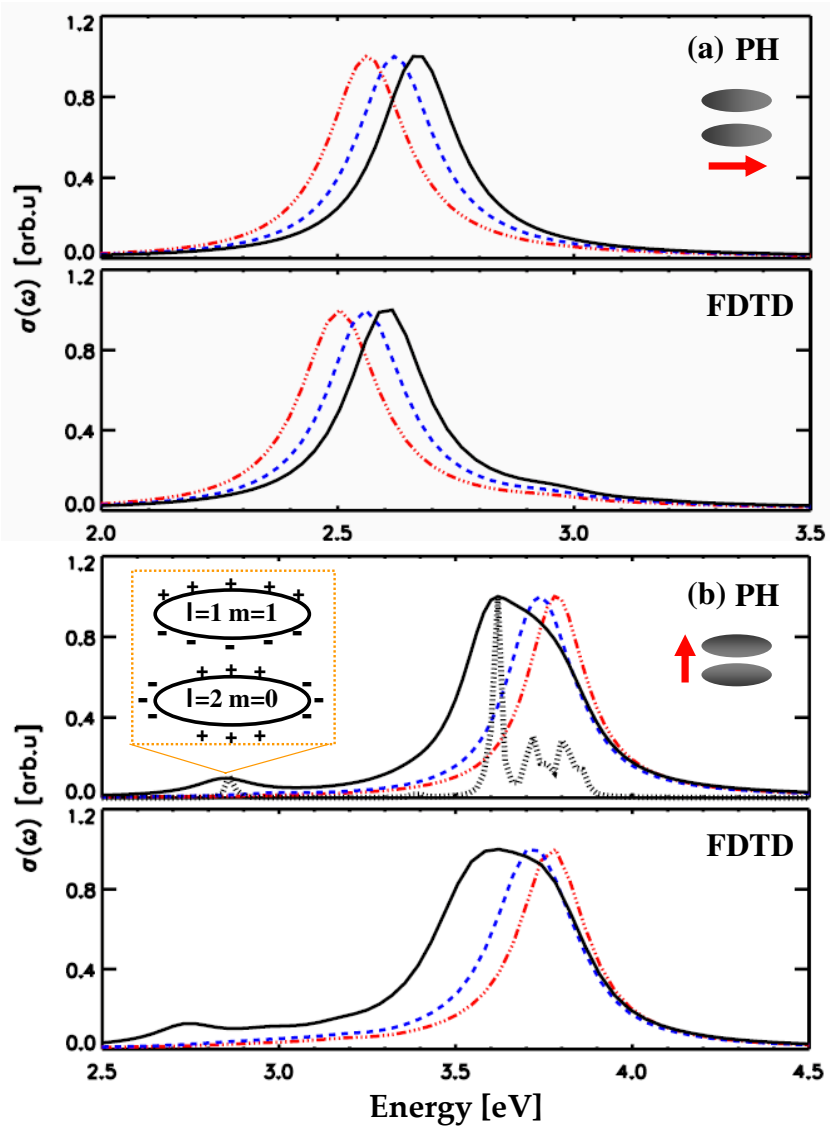

Figure 2.7 : Optical absorption spectra of the silver NR dimer in the PA configuration calculated using PH and FDTD and a damping $\delta = 0.1$ eV. Panel **(a)** is for longitudinal polarization and **(b)** is for transverse polarization as indicated by the arrows. Dimer separations are $D = 7$ nm (solid), $D = 9$ nm (blue dashed) and $D = 13$ nm (red dot-dashed). The dotted line in panel **(b)** is calculated using a damping $\delta = 0.01$ eV. The inset illustrates the coupling between primitive $m = 0$, $l = 2$ and $m = 1$, $l = 1$ plasmons on adjacent NRs.

2.4 Electric field enhancements

Here we will discuss how the PH method can be extended to the calculation of the local electric field enhancements. To simplify the description we employ a vector notation [111]. For a NR dimer interacting with an incident dipolar field of strength $E_0 \exp[-i\omega t]$, the Lagrangian takes the form,

$$L_{tot} = \frac{1}{2}\dot{\vec{X}}^T \hat{T} \dot{\vec{X}} - \vec{X}^T \hat{V} \vec{X} - E_0 \exp[-i\omega t] \vec{D}^T \hat{\chi} \hat{\beta} \vec{X}. \tag{2.16}$$

The vector $\vec{X}$ is the scaled primitive plasmon amplitude, $\hat{T}$ and $\hat{V}$ are the kinetic and potential energy matrices, $\hat{\chi}$ is the matrix relating the total charge vector $\vec{\tau}$ to the free charge $\vec{\sigma}$, $\hat{\beta}$ is the matrix relating $\vec{\sigma}$ and $\vec{X}$, and $\vec{D}$ is the vector with the dipole moments of the primitive plasmon modes [106]. Using the Euler-Lagrange equations the primitive plasmon amplitudes can be obtained as,

$$\vec{X} = E_0[\omega^2 \hat{T} - (\hat{V} + \hat{V}^T]^{-1} (\hat{\chi}\hat{\beta})^T \vec{D}. \tag{2.17}$$

Using $\vec{\tau} = \hat{\chi}\hat{\beta}\vec{X}$, the total charges can then be calculated as a function of the frequency and polarization of the incident light. Using Eq. (2.9) the total electrostatic potential can be expressed as the product $\Phi = \vec{Y}^T \hat{H} \vec{\tau}$, where the matrix $\hat{H}$ is defined by Eq. (2.9) and $\vec{Y}$ is a vector representing the basis of spherical harmonics. The local electric field enhancements are then simply obtained from the gradient of Φ.

In Fig. 2.8 we compare the local field enhancements for a nanosphere dimer calculated using PH and FDTD. As can be seen the calculations agree very well. The maximum field enhancement are around 300. The large field enhancements induced

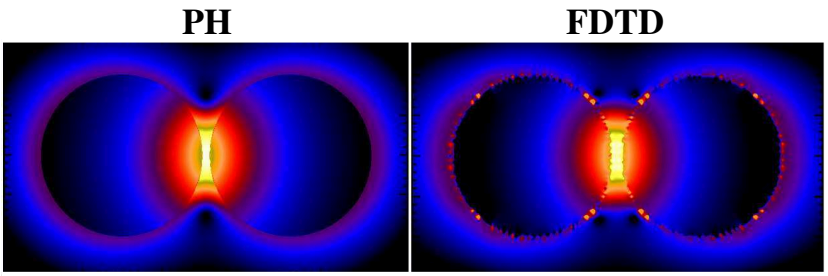

Figure 2.8 : Electric field enhancements for a silver nanosphere dimer for longitudinal polarization of the incident light calculated using the PH and FDTD method. The radii of the spheres are 10 nm and their separation is D=21 nm. The frequency of the incident light is 3.09 eV for PH and 2.95 eV for FDTD, corresponding to resonant excitation of the dipolar longitudinal dimer plasmon. The damping is $\delta = 0.1$.

in the nanosphere dimer are caused by the strong hybridization and admixture of higher primitive multipolar modes in the longitudinal dimer plasmon resonance [108].

In Fig. 2.9, we show the electric field enhancements for the NR dimer for different orientations and polarizations. The largest field enhancement for the PA configuration 100 is obtained for transverse excitation. The largest field enhancement for the AS configuration 300 is obtained for the longitudinal excitation. This field enhancement is similar to that found for the nanosphere dimer shown in Fig. 2.8.

The electric field enhancement in a NR dimer will obviously depend on the aspect ratio of the individual NR. To illustrate this we have calculated the maximum field enhancements for a NR dimer with a fixed junction width 1 nm for NRs of different aspect ratios. For a NR dimer with $a = 10$ nm the maximum field enhancement increases monotonously from 190 for $b = 1$ nm to 300 for $b = 10$ nm (sphere). The physical reason why the field enhancements for the NR dimer are smaller than those

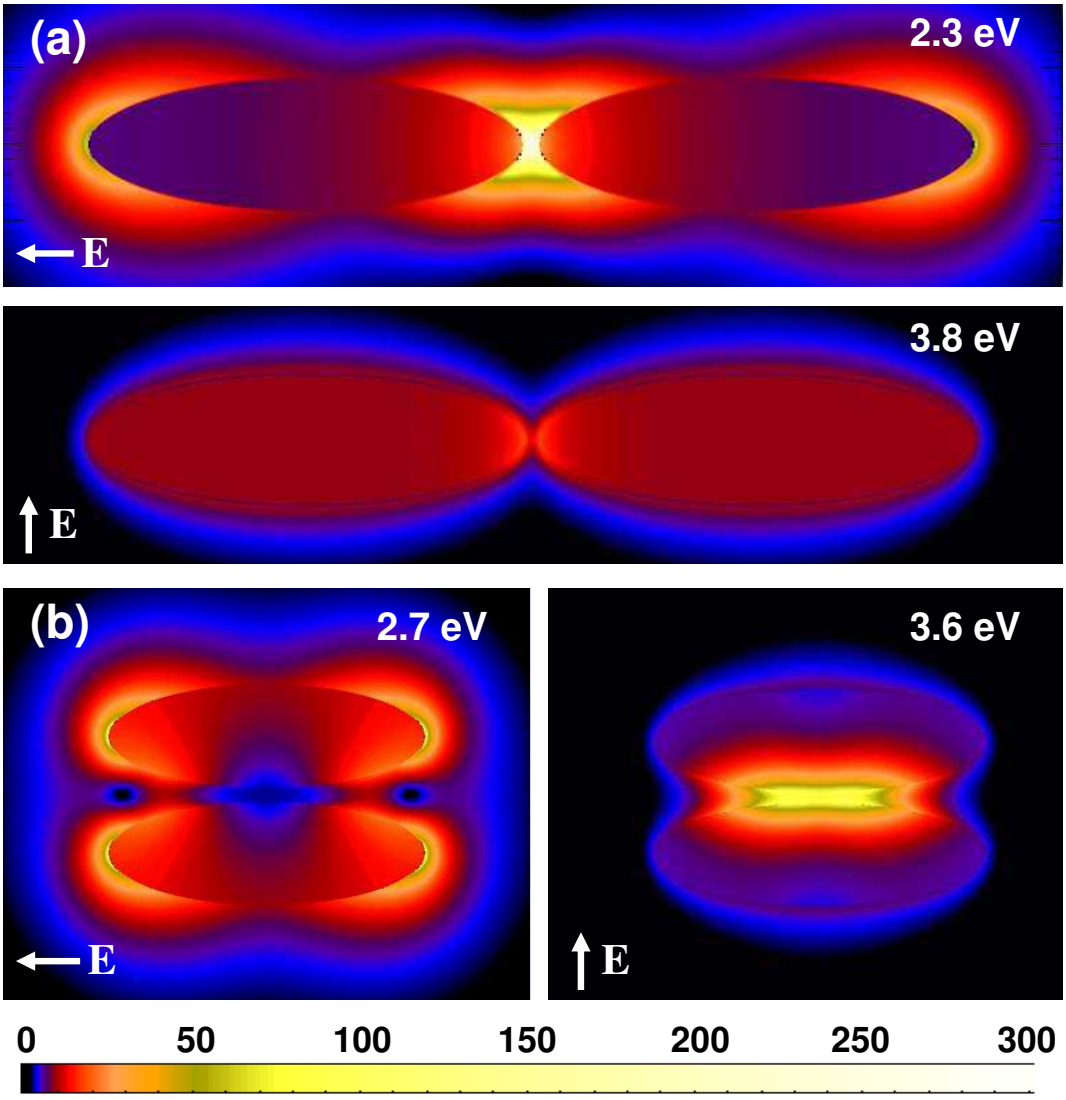

Figure 2.9 : Electric field enhancements in the silver NR dimer system for the AS **(a)** and PA **(b)** configurations for different polarizations of the incident light as indicated by the white arrows. The geometry of the NR is $a = 15$ nm and $b = 4.5$ nm. The dimer separations are 31 nm (AS) and 10 nm (PA). The frequencies correspond to resonant excitation and are shown in the panels. The damping used is $\delta = 0.1$.

for a sphere of radius $R = a$ is that the hybridization is smaller for a NR dimer as is also illustrated in Fig. 2.5. Although the primitive longitudinal dipolar NR plasmons provide larger field enhancements than the primitive dipolar nanosphere modes, fewer higher order multipolar modes are mixed into the hybridized dimer mode. For a NR dimer of fixed minor axis $b = 10$ nm, the maximum field enhancements increase monotonously with increasing major axis, a.

2.5 Conclusions

We have extended the plasmon hybridization method to NR dimers in symmetric and asymmetric situations. The NR dimer plasmons are formed from hybridization of the individual NR plasmon modes. The plasmonic interactions between the two NRs depend strongly on the relative orientations of the particles. The largest electric field enhancements are induced for a NR dimer in a symmetric axial configuration. The magnitude of the field enhancements depend on the aspect ratio of the NRs. For a NR dimer in an axial configuration and fixed overall length, the largest field enhancements are obtained for aspect ratios equal to 1, i.e. spheres. Our approach can easily be applied to heterodimer situations in which two NRs of arbitrary spatial orientation and size couple to an incident electromagnetic field.

Chapter 3

A Kirchhoff solution to metal nanoparticles[2]

In this chapter we continue our description of MNPs within the quasi-static approximation and show that within the Rayleigh size regime, the optical response of metal nanoparticles is governed by Kirchhoff's equations. Changes to the conductivity upon excitation of a surface plasmon result in dynamics which allow one to differentiate between the relaxation rate of a collective response and the average collision time of free electrons. Finally, by including spatial dispersion within the free electron gas of two capacitively coupled MNPs, a classical picture of the charge transfer regime is formed.

3.1 The advantage of small particle models

In future optical devices amplified electromagnetic fields [5, 63] resulting from sustained plasmons [15, 16] within MNPs will play a crucial role in experimental design. Applications using strongly coupled plasmons at MNP surfaces [112,113] benefit from models that can identify proximity effects such as conductive contact [102], which can alter the intended response of a plasmonic device.

[2] This chapter is based upon the manuscript entitled "A Kirchhoff solution to metal nanoparticles" by Britain Willingham and Stephan Link, currently under review.

Numerical implementations of Maxwell's equations well describe the optical response of MNPs observed experimentally [36, 114] but often hide the inner workings of MNPs. Instead, small particle solutions offer keen insight into factors which can dictate the dynamics of surface plasmons such as a MNP's shape [21,115,116], surface irregularities [117] or material anisotropy [118]. A consistent method to determine parameters such as the relaxation time τ^* of surface plasmons [119], composed of free electrons of lifetime $\tau \neq \tau^*$, would facilitate the separation of the radiative decay channel upon implementation into full scattering solutions [69].

In this chapter, we show that Ohm's law results in passive circuit components representing the optical response of intrinsic mechanisms within MNPs [120]. Kirchhoff's equations then govern the dynamics of free electrons within Drude's theory. By considering conductivity changes within the intraband, an analytical equation for the decay rate of quasi-free electrons shows an $(\hbar\omega)^2$ dependence on the photon energy. By considering the spatial dispersion of free electrons within MNP dimers, calculated optical absorption trends help bridge the quantum and classical description of surface plasmons within the charge transfer regime [102, 121].

3.2 Circuit model of a MNP

Fig. 3.1 shows a MNP situated in a harmonic field, $\mathbf{E_0}e^{-i\omega t}$, originating from charge on a remote AC-fed capacitor. The metallic state is described by a Drude model [122], where the conduction of quasi-free electrons is governed by Ohm's law $\boldsymbol{j} = \hat{\boldsymbol{\sigma}}\mathbf{E}$. Here,

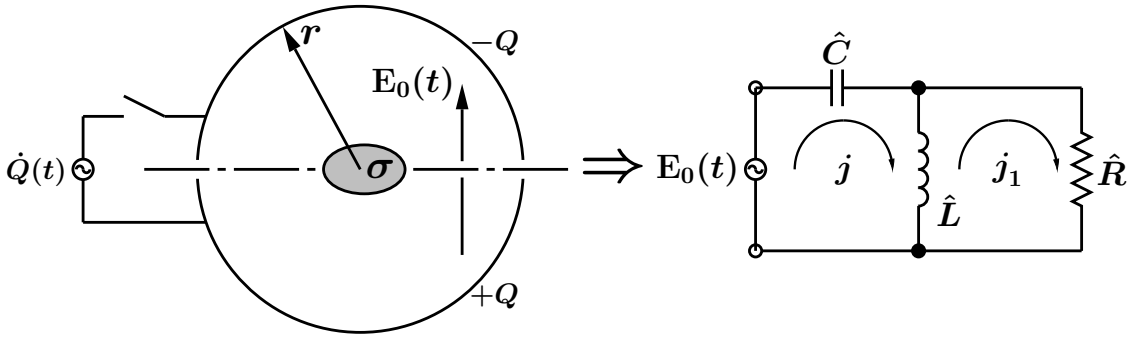

Figure 3.1 : A MNP of conductivity, $\sigma = \sigma_0[1 - i\omega\tau]^{-1}$, placed within a cylindrical capacitor fed by an AC current. As $r \to \infty$, the incident field, $\mathbf{E_0}$, is spatially constant. The MNP surface interacts capacitively with the external agent, leading to an equivalent *high-pass filter* schematic for MNPs.

$\hat{\boldsymbol{\sigma}} = \hat{\boldsymbol{\sigma}}_\mathbf{1} - i\omega\hat{\boldsymbol{\chi}}_\mathbf{1}$ is a diagonal tensor with components, $\sigma_{\mu\nu} = \sigma\delta_{\mu\nu}$, given by the AC-conductivity, $\sigma = \sigma_0[1 - i\omega\tau]^{-1}$. Its real component describes the conduction of free electrons of charge density $\rho = -en$ within the MNP, $\boldsymbol{j}_\mathbf{1} = -ne\boldsymbol{v} = \hat{\boldsymbol{\sigma}}_\mathbf{1}\mathbf{E}$, while the ionic susceptibility, $\hat{\boldsymbol{\chi}}_\mathbf{1}$, leads to a frequency dependent phase shift, $\boldsymbol{j} - \boldsymbol{j}_\mathbf{1} = -i\omega\hat{\boldsymbol{\chi}}_\mathbf{1}\mathbf{E}$, of the induced current density, $\boldsymbol{j} = -i\omega\mathbf{P}$ [123]. As a result of the transport of free charge to the surface, depolarization of the internal field, $\mathbf{E} = \mathbf{E_0} - \hat{\boldsymbol{B}}\mathbf{P}$, leads to classical dynamics of the free electrons determined by Kirchhoff's equations,

$$\begin{aligned} \mathbf{E_0} &= -i\omega\hat{\boldsymbol{L}}(\boldsymbol{j} - \boldsymbol{j}_\mathbf{1}) + \frac{i}{\omega}\hat{\boldsymbol{B}}\boldsymbol{j}, \\ 0 &= -i\omega\hat{\boldsymbol{L}}(\boldsymbol{j}_\mathbf{1} - \boldsymbol{j}) + \hat{\boldsymbol{R}}\boldsymbol{j}_\mathbf{1}. \end{aligned} \tag{3.1}$$

The ambiguity attached to the optical properties of MNPs is clarified by its analogy to the circuit shown in Fig. 3.1. Here, $\hat{\boldsymbol{R}} = \hat{\boldsymbol{\sigma}}_\mathbf{1}^{-\mathbf{1}}$, $-\omega^2\hat{\boldsymbol{L}} = \hat{\boldsymbol{\chi}}_\mathbf{1}^{-\mathbf{1}}$, and $\hat{\boldsymbol{B}} = 4\pi\hat{\boldsymbol{d}}\,(\mathrm{tr}(\hat{\boldsymbol{d}}) = 1)$ is a diagonal matrix containing the Cartesian geometry factors, $d_\mu = \hat{\boldsymbol{e}}_{\boldsymbol{\mu}}^{\perp} \cdot \hat{\boldsymbol{d}}\hat{\boldsymbol{e}}_{\boldsymbol{\mu}}$ [123]

when projected onto each unit vector $\hat{\boldsymbol{e}}_{\boldsymbol{\mu}}$ ($\mu = x, y, z$).

The displacement of the electron gas from the positive ionic background results in a capacitance per unit length, $\hat{\boldsymbol{C}} = \hat{\boldsymbol{B}}^{-\mathbf{1}}$, due to charge separation at the MNP surface. $\hat{\boldsymbol{C}}$ is determined only by the shape of the MNP, and increases linearly with an embedding medium [123]. At resonant frequencies in the optical and IR regions ($\hat{\boldsymbol{\chi}}_{\mathbf{1}} < 0$), capacitive discharge of stored energy, $\mathcal{U} = (\mathbf{P}^{\dagger} \cdot \hat{\boldsymbol{C}}^{-\mathbf{1}}\mathbf{P})/2$, drives free electrons into coherent oscillations whose change in motion is impeded by the reactivity, $\omega\hat{\boldsymbol{L}}$. For $\boldsymbol{j} = \boldsymbol{j}_{\mathbf{1}} + i\boldsymbol{j}_{\mathbf{2}}$, the Hamiltonian density of the MNP circuit in Fig. 3.1 is

$$\mathcal{H} = \frac{1}{2}(\boldsymbol{j}_{\mathbf{2}}^{\dagger} \cdot \hat{\boldsymbol{L}}\boldsymbol{j}_{\mathbf{2}}) + \frac{1}{2}(\mathbf{P}^{\dagger} \cdot \hat{\boldsymbol{C}}^{-\mathbf{1}}\mathbf{P}) - \mathbf{P} \cdot \mathbf{E}_{\mathbf{0}}, \tag{3.2}$$

while its rate of change is $\mathcal{R}e\{\dot{\mathcal{H}}\} = -\boldsymbol{j}_{\mathbf{1}}^{\dagger} \cdot \mathbf{E}/2$, where $\boldsymbol{j}_{\mathbf{1}}^{\dagger}$ is the transpose-conjugate of the observable current density. By considering Eq. (3.2), the full dynamics of free electrons within MNPs can be investigated.

For a MNP described by the geometry factors, d_{μ}, driven in each Cartesian direction by a field, $E_{\mu} = \hat{\boldsymbol{e}}_{\boldsymbol{\mu}}^{\perp} \cdot \mathbf{E}_{\mathbf{0}}$, the peaks in absorption identify the resonance frequencies of the MNP circuit where the total complex impedance becomes real. Fig. 3.2-**a** shows the time-averaged power loss per unit volume [60], $\mathcal{P}_{avg} = \sum_{\mu} \mathcal{P}_{\mu} = -\mathcal{R}e\{\dot{\mathcal{H}}\}$, within an ellipsoidal MNP, $(x/a)^2 + (y/b)^2 + (z/c)^2 = 1$, of dimensions $a = 2b = 3c$, where $\mathbf{E}_{\mathbf{0}} = (\hat{\boldsymbol{e}}_{\boldsymbol{x}} + \hat{\boldsymbol{e}}_{\boldsymbol{y}} + \sqrt{2}\hat{\boldsymbol{e}}_{\boldsymbol{z}})/2$. The peak locations are determined by considering the conservation of energy, $\mathcal{R}e\{\mathcal{H}\}$, of the free dynamics ($\mathbf{E}_{\mathbf{0}} = \mathbf{0}$) where the conversion from optical to mechanical energy is maximum. Each resonance frequency, ω_{μ}, de-

pends upon the dispersion of free electrons $\hat{\boldsymbol{\varepsilon}}_{\mathbf{1}} = \hat{\mathbf{1}} + 4\pi\hat{\boldsymbol{\chi}}_{\mathbf{1}}$, as well as their dissipation $\hat{\boldsymbol{\varepsilon}}_{\mathbf{2}} = 4\pi\hat{\boldsymbol{\sigma}}_{\mathbf{1}}/\omega$ according to,

$$\varepsilon_1(\omega_\mu) - [1 - \varepsilon_1(\omega_\mu)]\frac{1}{Q_\mu^2} = 1 - \frac{1}{d_\mu}. \tag{3.3}$$

Here, $\hat{\boldsymbol{\varepsilon}} = \hat{\boldsymbol{\varepsilon}}_{\mathbf{1}} + i\hat{\boldsymbol{\varepsilon}}_{\mathbf{2}}$ is the dielectric function of the free electrons and $Q_\mu = [1 - \varepsilon_1(\omega_\mu)]/\varepsilon_2(\omega_\mu)$ are the Cartesian components of the quality factor determined by the MNP circuit in Fig. 3.1. For a DC-conductivity expressed as the bulk plasma frequency [122], $4\pi\sigma_0 = \omega_p^2\tau$, Eq. (3.3) results in the quasi-static Mie resonances, $\omega_\mu^2 = \omega_p^2 d_\mu$. In the optical and near-IR, $Q_\mu = \omega_\mu\tau \gg 1$ for most simple metals. Consequently, Eq. (3.3) then takes on the well known form $\varepsilon_1(\omega_\mu) = 1 - 1/d_\mu$ [3].

The constant line-width, $\Gamma = \hbar\tau^{-1}$, of each absorption peak in Fig. 3.2-**a** characterizes the single decay mechanism of Drude's model of the metallic state [31], and reflects the equal strength of the free electron oscillations in each Cartesian direction within an isotropic material. This is evident by considering the resonance condition of Eq. (3.3). For a free electron gas, the Mie resonances are exactly the frequencies at which the LC-impedance of the MNP circuit in Fig. 3.1 vanish, $\omega_\mu^2 = (L_\mu C_\mu)^{-1}$. This condition leads to electronic current density, $\hat{\boldsymbol{e}}_{\boldsymbol{\mu}}^{\perp} \cdot \boldsymbol{j}_{\mathbf{1}} = -i\omega_\mu C_\mu E_\mu$, whose drift velocity suffers no resistance to flow. For the condition, $\omega_\mu\tau \gg 1$, this impedance match leads to a simple relation concerning the power consumption of excited surface plasmons in each Cartesian direction, $\mathcal{P}_\mu/\mathcal{P}_\nu \approx (E_\mu/E_\nu)^2$. As Fig. 3.2-**a** shows, the power absorbed in the $\hat{\boldsymbol{e}}_{\boldsymbol{x}}$ and $\hat{\boldsymbol{e}}_{\boldsymbol{y}}$ directions is indistinguishable in magnitude, despite the different geometry factors and conductivity associated with each resonance. As a

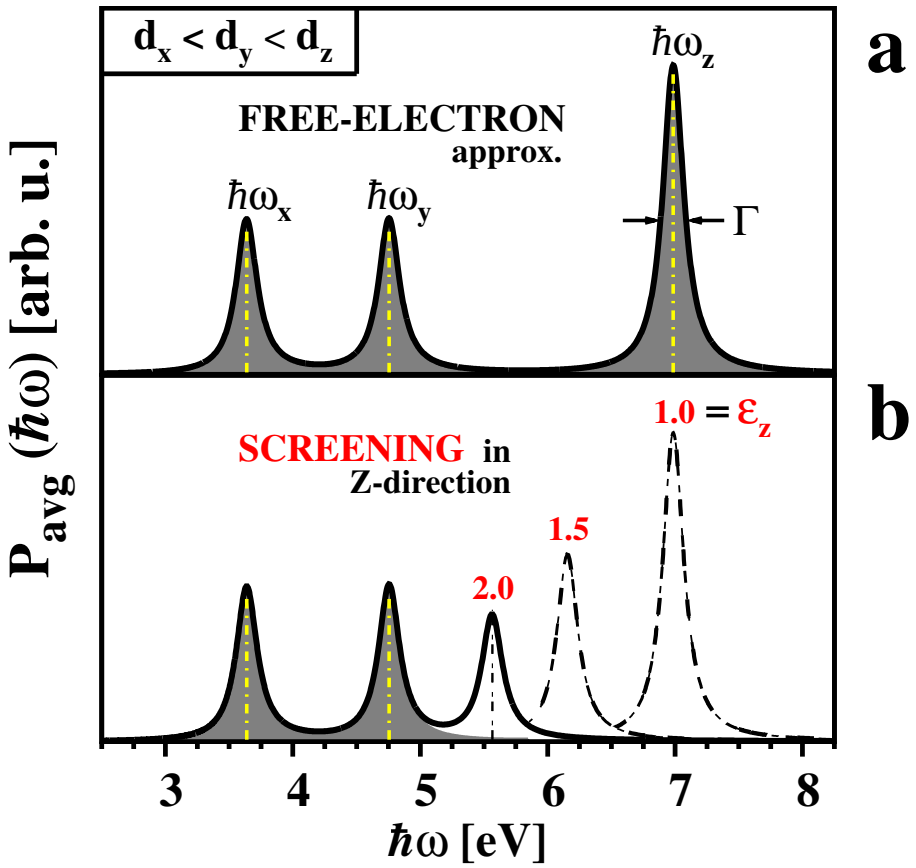

Figure 3.2 : Power loss per unit volume within a metal ellipsoid of dimensions, $a = 2b = 3c$, when excited by a field, $\mathbf{E_0} = (\hat{\boldsymbol{e}}_{\boldsymbol{x}} + \hat{\boldsymbol{e}}_{\boldsymbol{y}} + \sqrt{2}\hat{\boldsymbol{e}}_{\boldsymbol{z}})/2$. **(a)** Free electron metal with relaxation rate of $\Gamma = \hbar\tau^{-1} = 0.2$ eV, and bulk plasma frequency, $\hbar\omega_p = 9.2$ eV. Peak absorption occurs at frequencies where the LC-impedance of the MNP circuit vanishes, $\omega_\mu^2 = (L_\mu C_\mu)^{-1}$. **(b)** Screening in the $\hat{\boldsymbol{e}}_{\boldsymbol{z}}$ direction, $\varepsilon_z = \{1, 1.5, 2\}$, red-shifts the surface plasmon energy, $\hbar\omega_z$. The effective mass due to screening results in a decrease in average power consumption. Peaks due to unscreened ($\hat{\boldsymbol{\Delta}} = \hat{\mathbf{0}}$) excitations in the $\hat{\boldsymbol{e}}_{\boldsymbol{x}}$ and $\hat{\boldsymbol{e}}_{\boldsymbol{y}}$ directions are unchanged in location and magnitude.

result, the power consumption in the $\hat{\boldsymbol{e}}_{\boldsymbol{z}}$ direction is twice that of either orthogonal counterpart, $\mathcal{P}_x \approx \mathcal{P}_y \approx \mathcal{P}_z/2$.

3.2.1 Screening of free electrons

To further model the optical response of MNPs we must account for the changes in dynamics upon screened interactions, such as non-local models, $\hat{\boldsymbol{\sigma}}(\boldsymbol{q},\omega)$, and the influence of the core-potential [124]. We neglect e-e interactions, and first determine the additional MNP circuit components upon changes in the ionic susceptibility, $\hat{\boldsymbol{\chi}}_{\mathbf{1}}^{*} = \hat{\boldsymbol{\chi}}_{\mathbf{1}} + \hat{\boldsymbol{\Delta}}$, where $\hat{\boldsymbol{\varepsilon}}_{\boldsymbol{d}} = \hat{\mathbf{1}} + 4\pi\hat{\boldsymbol{\Delta}}$. To amend Fig. 3.1, we note that previously the complex impedance of the inductive circuit component of the MNP was given as $\hat{\boldsymbol{Z}}_{\boldsymbol{L}} = -i\omega\hat{\boldsymbol{L}} = (-i\omega\hat{\boldsymbol{\chi}}_{\mathbf{1}})^{-1}$. By taking into account the change in the complex conductivity tensor, $\hat{\boldsymbol{\sigma}}^{*} = \hat{\boldsymbol{\sigma}}_{\mathbf{1}} - i\omega\hat{\boldsymbol{\chi}}_{\mathbf{1}}^{*}$, changes to the susceptibility screen the dynamics of free electrons via an effective capacitance, $\hat{\boldsymbol{Z}}_{\boldsymbol{C}} = (i/\omega)\hat{\boldsymbol{\Delta}}^{-\mathbf{1}}$, in parallel with the original inductance of the free electron motion. By Thévenin's theorem an effective capacitance, $\hat{\boldsymbol{C}}^{*} = \hat{\boldsymbol{C}} + \hat{\boldsymbol{\Delta}}$, and a screened source, $\hat{\boldsymbol{C}}^{*}\mathbf{E}_{\mathbf{0}}^{*} = \hat{\boldsymbol{C}}\mathbf{E}_{\mathbf{0}}$, can be constructed to replace the original components in an equivalent MNP circuit, analogous to the bulk metallic response of dressed ions to an electronically screened external field [24].

In Fig. 3.2-**b** the consequences of screening on the average optical power consumed within the previously described ellipsoidal MNP are shown. By increasing the effective capacitance in the $\hat{\boldsymbol{e}}_{\boldsymbol{z}}$-direction ($\varepsilon_z = \hat{\boldsymbol{e}}_{\boldsymbol{z}}^{\perp} \cdot \hat{\boldsymbol{\varepsilon}}_{\boldsymbol{d}}\hat{\boldsymbol{e}}_{\boldsymbol{z}}$) the resonance frequency of the independent electrons decrease via Eq. (3.3) as the effective mass tensor increases as a function of the MNP shape, $\hat{\boldsymbol{m}}^{*} = [\hat{\mathbf{1}} + \hat{\boldsymbol{d}}(\hat{\boldsymbol{\varepsilon}}_{\boldsymbol{d}} - \hat{\mathbf{1}})]\hat{\boldsymbol{m}}$. This reflects the screened geometry factors, $\hat{\boldsymbol{m}}^{*}\hat{\boldsymbol{d}}^{*} = \hat{\boldsymbol{m}}\hat{\boldsymbol{d}}$, that result from the mutual polarization of free electrons and the ionic background. This increased inertia red-shifts the collective

oscillations while reducing the power consumption of surface plasmons by the ratio of the electron's renormalized mass, $\mathcal{P}^*_\mu/\mathcal{P}_\mu \approx (m_\mu/m^*_\mu)^2$.

3.2.2 Lifetime of plasmons

Screened electrons with effective mass reluctantly react to fields when compared to conventional free electrons. Despite this decoherence, the relaxation time of the surface plasmons remained that of the average electron collision interval, τ [125]. We expect conduction to the MNP surface to differ from the free electron case, being characterized by increased conductivity, $\hat{\boldsymbol{\sigma}}^*_{\mathbf{1}} = \hat{\boldsymbol{\sigma}}_{\mathbf{1}} + \hat{\boldsymbol{\delta}}$, at the onset of a collective motion of electrons. Here, the perturbation tensor $\hat{\boldsymbol{\delta}}$ is represented as an additional parallel resistance to the MNP circuit in Eq. (3.1). The bandwidth of oscillating surface plasmons, $\hat{\boldsymbol{\Gamma}}^* = -\hat{\boldsymbol{\chi}}^{-\mathbf{1}}_{\mathbf{1}}\hat{\boldsymbol{\sigma}}^*_{\mathbf{1}}$, results in the relaxation rate for a collective motion of correlated electrons, $\hat{\boldsymbol{\Gamma}}^* = \hat{\boldsymbol{\Gamma}} - \hat{\boldsymbol{\chi}}^{-\mathbf{1}}_{\mathbf{1}}\hat{\boldsymbol{\delta}}$, where $\hat{\boldsymbol{\Gamma}}$ is a diagonal tensor with components, $\Gamma = \hbar\tau^{-1}$. The decay rate of surface plasmons at resonance, $\hbar\omega_\mu$, in each Cartesian direction is now given by,

$$\frac{1}{\tau^*_\mu} = \frac{1}{\tau}\Big[1 + \frac{\delta_\mu}{\sigma_0}(1 + \tau^2\omega^2_\mu)\Big]. \tag{3.4}$$

The surface plasmon bandwidth of Eq. (3.4) goes as $(\hbar\omega_\mu)^2$, as in the low frequency region of weak e-e interactions within Fermi-liquids and is consistent with the shape dependent damping experimentally observed in MNPs [21, 116].

Fig. 3.3-{**a-c**} highlights the importance of Eq. (3.4) when describing the optical absorption of realistic metals. By introducing a positive DC-bias ($\delta_\mu = +|X|\sigma_0$) to

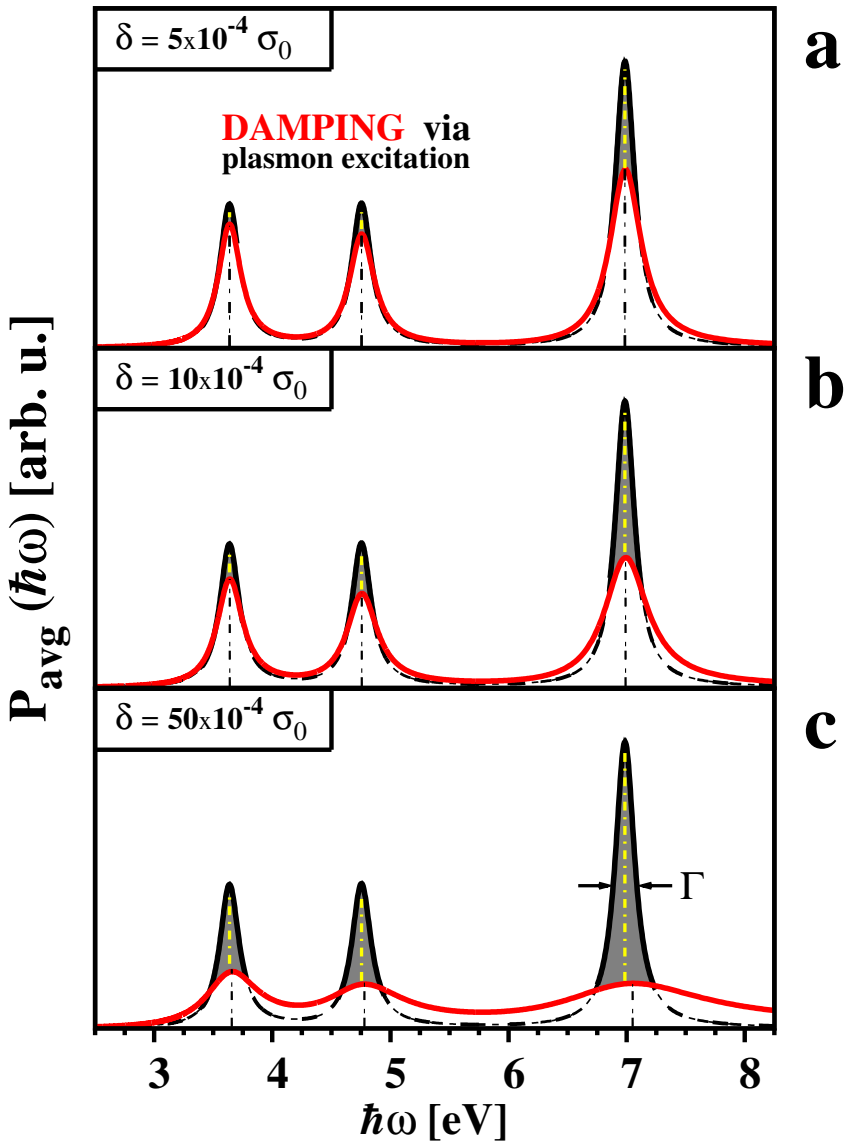

Figure 3.3 : Comparison of power loss per unit volume within a MNP described by free electron oscillations of constant decay rate, $\Gamma = 0.2$ eV, discussed in Fig. 3.2-**a** (filled curves) and when exciting surface plasmons with lifetimes given by Eq. (3.4) (solid red lines) when: **(a)** $\delta/\sigma_0 = 5 \times 10^{-4}$,**(b)** $\delta/\sigma_0 = 10 \times 10^{-4}$, and **(c)** $\delta/\sigma_0 = 50 \times 10^{-4}$. Peaks become increasingly asymmetric at higher energies, with surface plasmons blue-shifting from their free electron resonance as a result of Eq. (3.3). Capacitive screening has been neglected ($\hat{\mathbf{\Delta}} = \hat{\mathbf{0}}$).

the free electron conductivity and neglecting the red-shift due to screening ($\hat{\mathbf{\Delta}} = \hat{\mathbf{0}}$), peak absorption drops disproportionately as shown in Fig. 3.3-**a**. The Mie resonances of Eq. (3.3) no longer provide an impedance match for the LC-components of the MNP circuit. As a result, surface plasmons peak in amplitude when driven at frequencies dependent upon their relaxation rate via Eq. (3.4), and for larger $\delta_\mu (= \delta)$ the absorption profiles become asymmetric, Fig. 3.3-**b**. At still greater, static additions to the conductivity, Fig. 3.3-**c**, one can clearly see that surface plasmons are blue-shifted from the LC-resonance frequency of the free electron gas (filled curves), a condition often reported for noble MNPs approaching the quantum size regime [126]. Here, electronic "spill-out" can be interpreted as an impedance mismatch at the MNP surface [127]. As shown, this is detrimental to the lifetime of the coherent state, quenching the dipole moment while pushing resonant conditions to higher frequencies [126].

3.3 Proximity effects in coupled MNPs

Proximity effects are the hallmark of small particle models [128]. To include capacitive coupling between MNPs, vector components of the electric field in Ohm's law are now distinct multi-poles, $\mathbf{E} = \sum_{lm} \mathbf{E}_{lm}$, where $\mathbf{E}_{lm} = -\nabla\phi_{lm}$ forms a solution to Poisson's equation [60]. Using Eq. (3.1) with capacitive coupling coefficients [60] due to local fields, $\mathbf{E_0} \rightarrow \mathbf{E_0} + \mathbf{E}_i$, within the i^{th} MNP, where $\mathbf{E}_i = \sum_{j \neq i} \hat{\boldsymbol{C}}_{ij}^{-1} \mathbf{P}_j / 2$ describes the external field originating from the j^{th} surrounding MNPs, coupled systems are easily

investigated via Kirchhoff's equations.

As an example, consider two metal spheres with geometry factors $d_l = l/(2l+1)$, aligned along the $\hat{\boldsymbol{e}}_{\boldsymbol{z}}$ direction. Each has a radius of $a = 24\ a_0$ ($a_0 = 0.529$ Å) and is described by a Wigner-Seitz radius of $r_s = 3.0\ a_0$ [121]. The free electrons decay at a rate of $\hbar\tau^{-1} = 0.27$ eV with spatial dispersion characterized by the conductivity

$$\sigma(\omega, q) = \frac{\sigma_0}{1 - i\tau\Omega(\omega, q)}, \tag{3.5}$$

appropriate for the longitudinal hydrodynamic approximation. Spurious reflections [129] are accounted for by incorporating the modified boundary conditions of Fuchs and Dasgupta [130]. Here, $\Omega(\omega, q) = \omega[1 - \frac{3}{5}(v_f q/\omega)^2]$, and the Fermi velocity is $v_f = 1.4 \times 10^8$ cm/sec. A capacitive bias is applied to tune the individual dipole ($l = 1$) surface plasmons to 5 eV while screening from the polarizable background is neglected ($\hat{\boldsymbol{\Delta}} = \hat{\mathbf{0}}$) to compare with *ab initio* solutions [121].

Fig. 3.4 shows $\mathcal{P}_{avg}(\hbar\omega)$ for an incident field polarized along the dimer axis. As the surface-to-surface separation, g, is decreased from $g = a$ (top curve) to the short-circuit limit $g = 0$ (red points) all optically active modes red-shift, but do not diverge [128]. Within the charge transfer regime ($g/a_0 < 4$) [121], the hybridized dipole mode red-shifts out of view (green curve) and is no longer amplified [102]. Higher order plasmon modes are now driven to larger amplitudes [131], forming an absorption band at the onset of a charge transfer plasmon [102, 121]. Classically no new eigenmodes appear [102], the optical sum rule conserves the spectral weight by shifting power uptake to higher order modes, while the hybridized dipole (green curve)

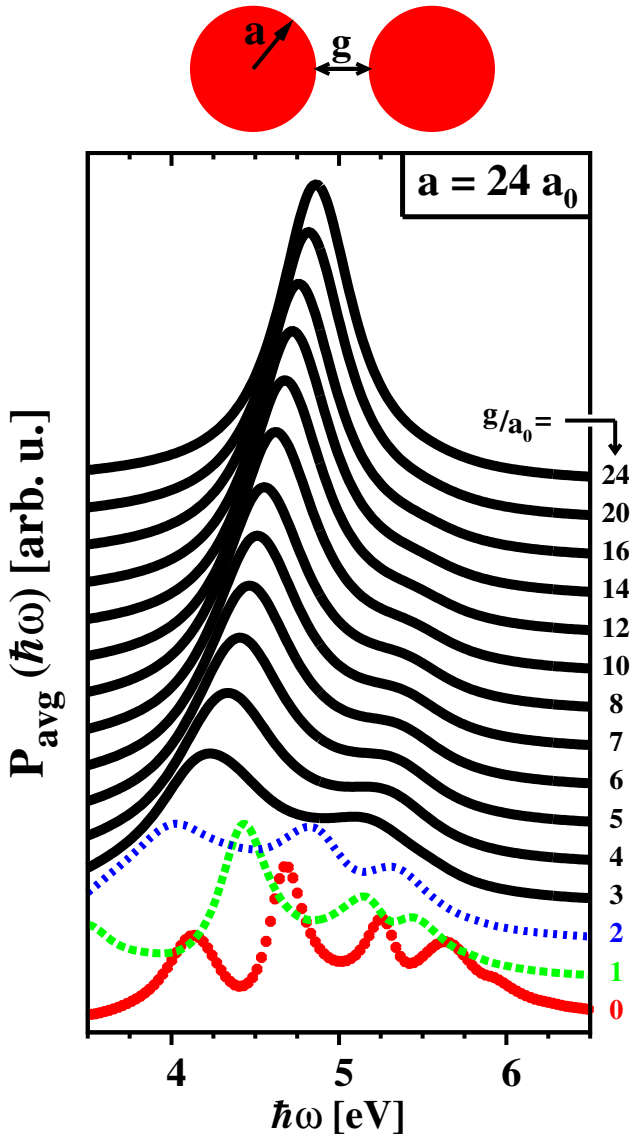

Figure 3.4 : Power loss per unit volume within a dimer of $a = 24\ a_0$ MNPs each described by $r_s = 3.0\ a_0$ and $\hbar\tau^{-1} = 0.27$ eV. As g/a_0 decreases from 24 (top curve) to $\{20, 16, 14, 12, 10, 8, 7, 6, 5, 4, 3\}$ all optically active modes red-shift. At $g/a_0 = 2$ (blue curve) higher order modes become dominant in amplitude. At $g/a_0 = 1$ (green curve) the dipole mode red-shifts out of view, decreasing in amplitude. When touching $g = 0$ (red points), higher order plasmon modes are left to harvest light at the MNP surface.

and quadrupole modes (red points) become quenched at close separations [131]. For continuity between previous quantum calculations [121] and Kirchhoff's solution, the impedance mismatch due to electron spill-out at the jellium edge [124] needs to be considered. As previously discussed, this should broaden surface plasmon modes while further blue shifting their resonant energies.

3.4 Conclusions

Starting with Ohm's law we have shown that the dynamics of MNPs can be described by Kirchhoff's equations. This model correctly identifies the conditions involving resonance, consistently accounting for screening of free electrons upon excitation into a surface plasmon. At resonance, these coherent states show a distinct relaxation rate when changes from the constituent free electron conductivity take place. An example showing the optical response of MNP dimers provides a classical description of the charge transfer regime, and further highlights MNPs analogy to passive circuits [120], as well as the insight provided when using a simple Kirchhoff solution to MNPs.

Chapter 4

Absorption and scattering in strongly coupled 1D MNP assemblies[3]

In this chapter we no longer consider just the quasi-static limit of MNPs, but move into systems of considerable size, where scattering and absorption share equal roles in the plasmonic response of MNP structures. Here we use vector wave solutions to Maxwell's equations, and consider a MNP to be described by a spherical geometry.

First we characterize perfectly linear 1D structures of MNPs. The saturation of the optical resonance energy with growing structure size is briefly discussed and its importance to sub-wavelength energy propagation is alluded to. By considering higher order multipole modes in the solution to the coupled plasmonic system, we show that closely spaced MNPs lead to the formation of super and sub-radiant plasmon modes, which are then defined by characteristic surface charge plots. Relative amounts of absorption and scattering losses are compared at the super-radiant plasmon mode, and larger MNP structures with small interparticle gaps are shown to be highly

[3] This chapter is based upon the manuscripts: (1) "Low absorption losses of strongly coupled surface plasmons in nanoparticle assemblies" by Wei-Shun Chang, Britain Willingham, Liane S. Slaughter, Bishnu P. Khanal, Leonid Vigderman, Eugene R. Zubarev, and Stephan Link, PNAS USA, vol. 108, pp. 19879–19884, 2011. (2) "Energy transport in metal nanoparticle chains via sub-radiant plasmon modes" by Britain Willingham and Stephan Link, Opt. Express, vol. 19, pp. 6450–6461, 2011.

suitable for the design of efficient plasmonic nano-antennas.

Finally realistic quasi-1D structures of chemically prepared MNPs are optically characterized. The limitations of capacitive coupling are identified using full scattering solutions, while conductive overlap of MNPs (resolved using finite-element-methods) is shown to be responsible for peaks in the near-IR of experimental spectra.

4.1 The importance of higher order plasmon modes in optical spectra

One-dimensional, hybridized MNP plasmons form plasmonic antennas which can couple to guided modes confined to sub-wavelength dimensions [132], or can be converted into intense local field distributions within MNP junctions [133]. In order to optimize energy propagation along fabricated structures, such as linear chains, or facilitate large electromagnetic field enhancements, exploited for localizing and amplifying radiation in nanoscale structures, it is necessary to understand interparticle coupling as well as energy decay channels [134, 135]. For a particle assembly, optical spectra provide a means to analyze these important factors [136–139].

The largest local field enhancements are found within structures with small interparticle gaps between constituent MNPs [140, 141]. Here, the near-field strength is directly related to the red-shift of the coupled MNP plasmons, as seen in the optical response of smaller assemblies of dimers and trimers [141–143], and results from the increased hybridization between higher order plasmon modes [63]. Studies have

shown that this spectral dependence of the electromagnetic field enhancements in MNP structures often follows the collective scattering response [141, 144, 145].

Using the coupled dipole approximation, it has been shown that the energy difference between scattering peaks for the longitudinal, L, and transverse, T, polarized dipole resonances [45] along linear 1D chains is directly related to the bandwidth of propagating surface plasmon polaritons, and therefore the coupling strength between constituent MNPs. The largest propagation lengths were then predicted at the single MNP plasmon resonance [15]. As interparticle separations decrease dipole interactions [45, 67, 146–151] are no longer sufficient and the increasing importance of multipolar modes for decreasing particle separations becomes evident in optical spectra and waveguiding applications [152]. Here, the appropriate inclusion of higher order modes into scattering solutions results in the formation of super and sub-radiant plasmon modes, whose characterization via optical spectra provide essential information about propagating surface plasmon polaritons [153, 154].

Because stronger coupling occurs for closely spaced MNPs, more efficient plasmonic antennas can also be realized for excitation at energies corresponding to super-radiant plasmon modes rather than at the single MNP response, unless the magnitude of ohmic loss also increases and absorption losses become prohibitive. Therefore, measuring both absorption and scattering cross-sections for coupled MNP plasmons which include higher order modes is necessary to understand the interplay between electromagnetic field enhancements and ohmic loss.

4.2 Optical characteristics of finite chains of MNPs

First, as shown in Fig. 4.1, we demonstrate that the energy splitting, ΔE, between the longitudinal and transverse polarized dipole resonances is highly dependent on both particle separations and numbers, N. Using the partial scattering solution to Mie's theory [2] for multiple spherical particles as described by Gèrardy and Ausloos [69], the optical spectra of finite linear chains are obtained to gain significant physical insight into the characteristics of propagating SPPs. Multipoles up to $l = 20$ were included in the calculations and all results have been independently tested for smaller chains of particles using the finite-element method.

In Fig. 4.1(a), we compare ΔE as a function of N for two interparticle separations $\sigma = 2.1$ and $\sigma = 3.0$, where σ is defined as the ratio of center-to-center distance, d, and nanoparticle radius, a, i.e. $\sigma = d/a$. The shift of the dipole resonance for longitudinal and transverse modes converges for particle chains of roughly $N = 10$, independent of σ [155]. The structure analyzed is shown in the lower corner of Fig. 4.1. The constituent particles have $a = 25$ nm and are surrounded by vacuum. In all cases, the optical cross-sections are normalized by N, while the incident wave vector, $\boldsymbol{k}$, is fixed perpendicular to the chain of particles situated along the z-axis. The material response neglects small particle effects, and is described by a Drude fit to the dielectric function of Ag, where the bulk resonance frequency is $\omega_b = 9.5$ eV, the non-radiative decay is given by $\Gamma = 0.1$ eV, and the high-frequency limit is $\varepsilon_\infty = 5.0$ [63]. For all calculations the surface-to-surface separations are ≥ 1 nm so that non-local dielectric

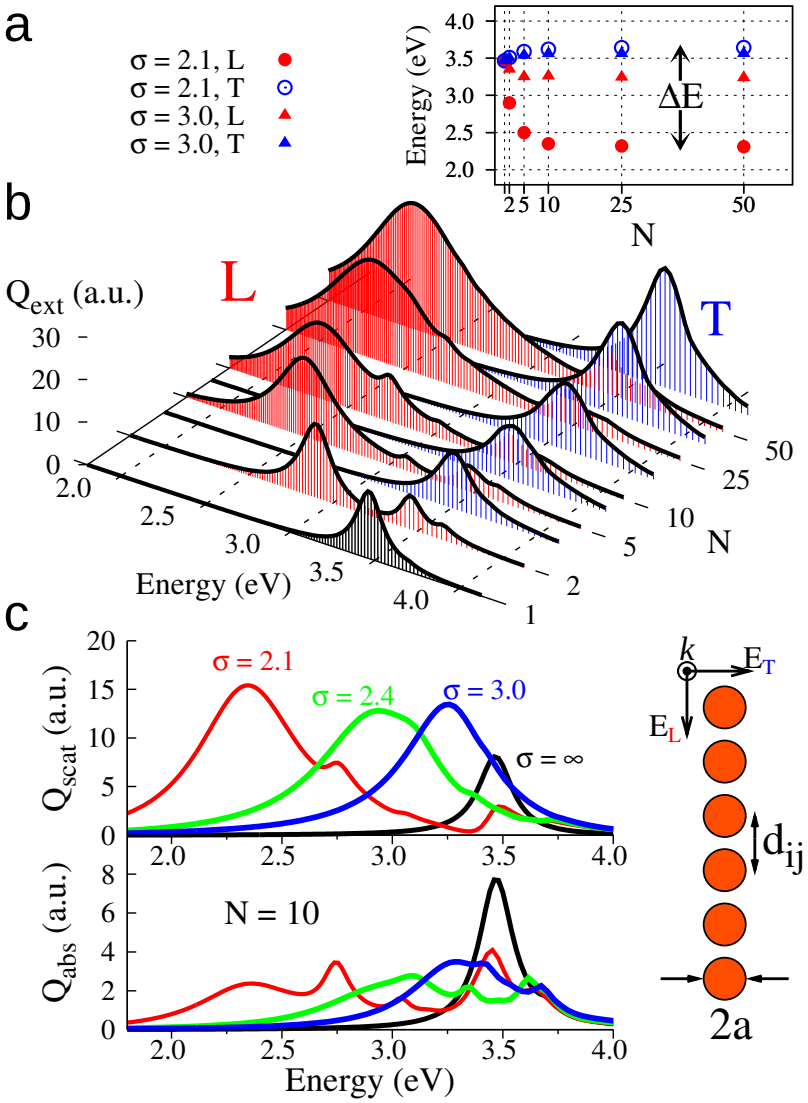

Figure 4.1 : Optical properties of finite chains with varying particle numbers N and center-to-center separations $d(\sigma) = \sigma a$, calculated by generalized Mie theory for Ag spheres with radius $a = 25$ nm. **(a)** Energy splitting, ΔE, between the longitudinal L(red) and transverse T(blue) dipole modes as a function of N for $\sigma = 2.1$, and $\sigma = 3.0$. **(b)** Optical extinction spectra of linear chains for L and T incident polarization and varying N at $\sigma = 2.1$. **(c)** Dependence of the optical absorption and scattering spectra of chains with $N = 10$ on σ for L-polarization. Note the different scales for Q_{abs} and Q_{scat}.

effects can be neglected [121].

The energy splitting, ΔE, which does not increase further upon addition of more particles, is a direct measure of the particle-particle interaction strength and alludes to an upper limit of the group velocity of SPPs [137]. If excited optically, chains with smaller interparticle separations should provide larger group velocities with enhanced propagation lengths, something not found in previous studies [15].

To determine the presence of higher order plasmon modes, we turn to the extinction spectra calculated for varying N at constant interparticle separation, $\sigma = 2.1$ (Fig. 4.1(b)). We first consider the longitudinal mode, which shows a drastic red-shift from the single particle response at 3.46 eV to the eventual saturation at 2.31 eV as N increases. The red-shift, due to increasing N and hybridization of higher order plasmon modes between particles at close separations, is accompanied by a broadening of the dipole peak. Radiative damping as well as additional dipole-like modes, seen as ripples to the blue of the main peak, contributes substantially to the width for $N \geq 5$.

For comparison, Fig. 4.1(b) also shows the extinction for transverse polarization, resulting from the formation of anti-bonding hybridized modes which slightly blue-shift to 3.64 eV at $N = 50$. This much smaller shift in resonance energy is due to reduced plasmonic interactions of the anti-bonding modes compared to the bonding modes for longitudinal polarized excitation [63].

By studying the effect of interparticle separation on the scattering and absorp-

tion spectra separately, we can determine the contributions of super and sub-radiant plasmon modes to the collective optical properties of finite particle chains. This is shown in Fig. 4.1(c), where scattering and absorption cross-sections, Q_{scatt} and Q_{abs}, of chains with $N = 10$ are compared for longitudinal polarization while varying σ. Important differences are seen for different σ in the scattering and absorption contributions to the overall extinction. Excluding the single particle Mie spectra at $\sigma = \infty$, it is clear that there are multiple peaks at increasingly distributed energies for smaller σ. Regardless of σ, however, the super-radiant dipole mode in the Q_{scatt} plots, having all particle dipoles aligned parallel to the chain, forms the most efficient antenna, losing energy predominantely through far-field scattering.

At $\sigma = 2.1$, the secondary dipole peaks between the main super-radiant mode at 2.35 eV and the quadrupole resonance at 3.47 eV are sub-radiant in nature. As shown below (Fig. 4.2), for sub-radiant modes, the surface charge density due to the induced polarization forms domains of dipole nature which alternate along the chain in standing wave configurations [153]. These optically active, or "bright", sub-radiant plasmon modes have non-zero dipole strength at close interparticle separations and hence contribute to Q_{scatt}, but always remain weaker than the super-radiant mode. Absorptive losses, as inferred from the Q_{abs} plots, exhibit a different trend. The super-radiant dipole resonance broadens and decreases in intensity due to dynamic depolarization [59], while the bright sub-radiant modes, like the one at 2.74 eV for $\sigma = 2.1$, display enhanced Q_{abs} compared to the main dipole peak. For small σ, the

Q_{scatt} and Q_{abs} plots illustrate that the most efficient coupling of light to the chain occurs at energies corresponding to sub-radiant and higher order modes, where losses due to far-field scattering are minimized.

4.3 Identifying super and sub-radiant modes

We can identify super and sub-radiant plasmon modes by their distinctive surface charge densities. Analysis of the induced polarization charge density waves can characterize the resonant nature of optical features, like those discussed in Fig. 4.1. Shown in Fig. 4.2 are the real surface charge densities, $\mathcal{R}e\{\rho_{pol}\}$, for the super-radiant and two lowest energy, bright sub-radiant modes of the $N = 10$ particle chain at $\sigma = 2.1$, corresponding to Q_{abs} of Fig. 4.1(c). From this vantage point, the incident wave vector, $\boldsymbol{k}$, is directed out of the page and is longitudinally polarized along the length of the chain.

The induced polarization charge density wave at 2.35 eV is characteristic of a super-radiant plasmon mode. A line segment (black line) taken along the surface of each particle through the chain axis, highlights the opposing concentrations of positive and negative charge. A standing wave pattern is visible in the surface charge density and is indicated by the magenta line, which identifies the plasmon mode as a collective dipole antenna, whose wavelength, λ_0, is equivalent to twice the length of the nanoparticle chain.

At 2.74 eV and 3.04 eV, the surface charge density also displays standing wave

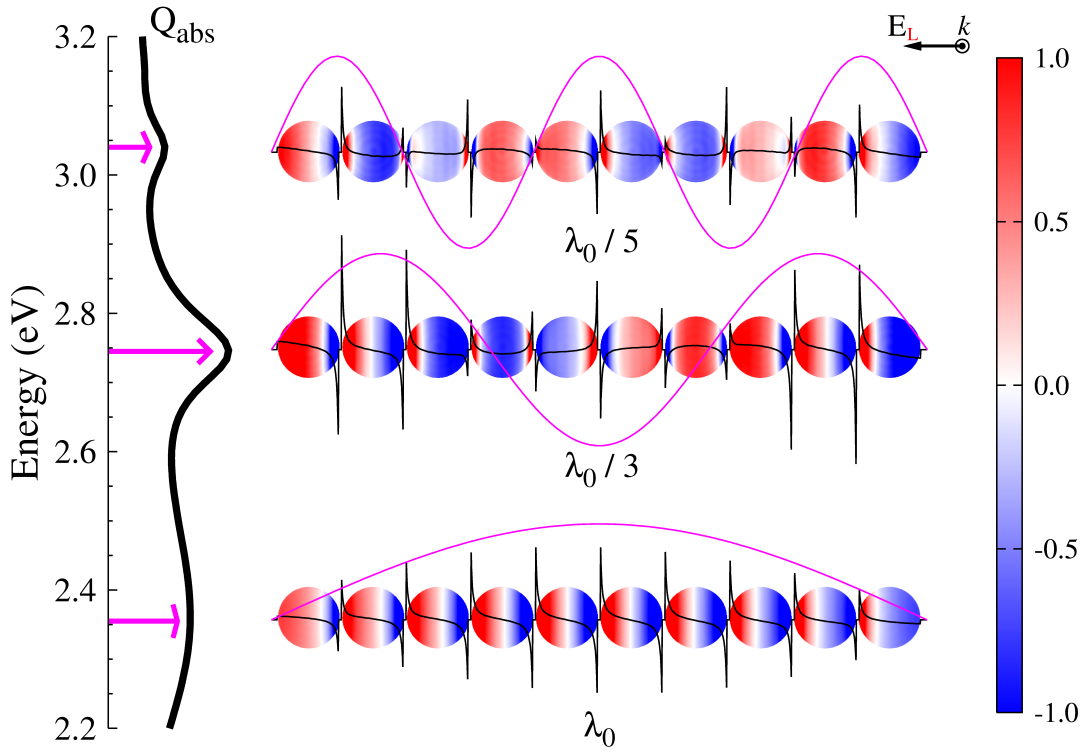

Figure 4.2 : Surface charge density, $\mathcal{R}e\{\rho_{pol}\}$, along a chain of $N = 10$ Ag nanoparticles of radii $a = 25$ nm at interparticle separations of $\sigma = 2.1$. Polarization induced charge density waves are highlighted by the magenta lines and have standing wavelengths of λ_0/n, which is further illustrated by a line segment (black line) of the surface charge density taken along the surface of each particle through the chain axis. Collective excitation at energies corresponding to Q_{abs}, shown on the left, induces optically active plasmon modes of both super- ($n = 1$) and sub-radiant ($n = 3, 5$) nature.

patterns due to the induced polarization (magenta lines) within the MNPs. These standing waves have wavelengths that are equal to integer fractions of the wavelength for the super-radiant mode, i.e. λ_0/n. The overall dipole moment for these collective resonances is diminished as localized charge distributions form dipole-like domains which alternate along the chain's length. Bright sub-radiant modes, like those shown

in Fig. 4.2 are identified by odd fractions of the fundamental charge density wave, $n = 1, 3, 5, ...$, and possess net dipole moments when excited in a collective manner. Dark sub-radiant modes, characterized by even integer fractions $n = 2, 4, 6, ...$, possess no net dipole moment when excited collectively, and therefore cannot be seen in the optical spectra in Fig. 4.1. Both bright and dark sub-radiant plasmon modes give rise to suppressed scattering, and can increase coupling to the incident field when excited asymmetrically (see section 4.4), as the surface charge density wave now forms nodal patterns which decay in magnitude along its length. Therefore it is expected that intrinsic sub-radiant eigenmodes should support propagation of low-loss SPPs along finite chains of metal nanoparticles [153].

4.4 The origin of sub-radiant plasmon modes

To further understand the physical nature of sub-radiant modes for particle chains, we again assume each MNP to be within the Rayleigh size regime and perform quasi-static calculations, as illustrated in Fig. 4.3. In the non-retarded limit, surface modes are defined by conservative polarizations which are irrotational $\boldsymbol{\nabla} \times \mathbf{P} = \mathbf{0}$ [156].

Assuming a quasi-static response of the polarization $\mathbf{P}$ of each particle and insisting that no bound charge is induced except within an infinitesimal volume at the surface $\boldsymbol{\nabla} \cdot \mathbf{P} = \mathbf{0}$, the macroscopic fields are described by the solutions to Laplace's equation [157]. Because of the time-harmonic nature of the material response, a polarization current, $\boldsymbol{j} = \partial \mathbf{P}/\partial t$ with constant charge carrier density is included. Using

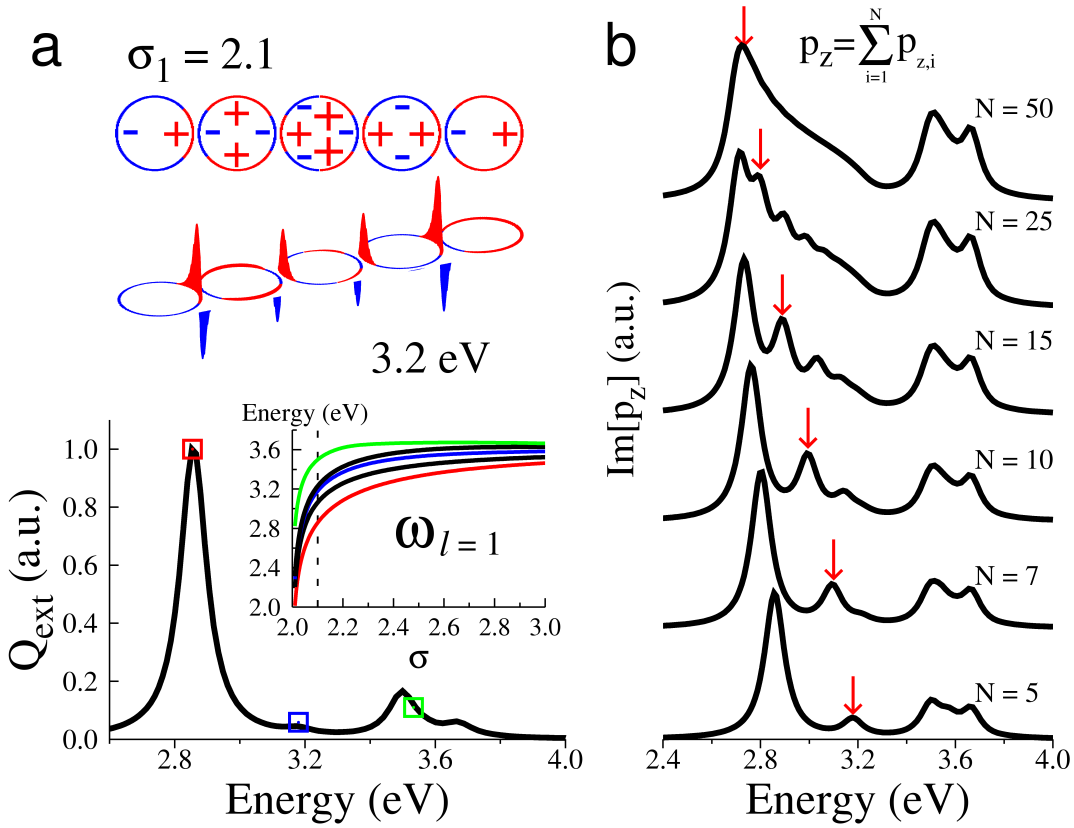

Figure 4.3 : Quasi-static calculations of chains for $\sigma = 2.1$ **(a)** Extinction spectrum for longitudinally polarized collective excitation and with $N = 5$. The inset illustrates the trends of the $l = 1$ plasmon modes as a function of σ. The charge plot taken at 3.2 eV confirms the identity of sub-radiant modes. **(b)** End-excitation of finite particle chains shows a progressive increase of the cumulative sum of the dipole moment at sub-radiant modes for increasing N.

the Hamilton relations, this leads to the equations of motion for the multipolar moments of each particle [60]. By solving for **P** in spherical coordinates and neglecting the contribution of the energy contained within the magnetic fields, the multipolar moments, q_{lmi}, are obtained by solving

$$\frac{l}{2l+1}\, q_{lmi} + \sum_{pk}\sum_{j\neq i}^{N} \mathrm{H}_{pkj}^{lmi}\, q_{pkj} = \frac{\omega_l^2}{\omega_b^2}\, q_{lmi} \tag{4.1}$$

where the ω_l's are the resonant modes of the system of spheres and $\hat{\mathrm{H}}$ is a Hermitian matrix representing the interaction of multiple particles [47]. The dipole per unit volume of the i^{th} sphere with unit vector $\hat{\mathbf{n}}_i$ normal to its surface is then given by

$$\mathbf{P}_i = \nabla_i(\sum_{lm} \frac{q_{lmi}}{l a_i^{2l+1}} \, r_i^l \, \mathrm{Y}_{lm}(\theta_i, \phi_i)), \tag{4.2}$$

where r_i is the radial distance from the center of the particle and Y_{lm} are the spherical harmonics. By adding to the Hamiltonian the energy loss of a system of dielectric spheres placed in an alternating, uniform field in vacuum, we can solve for the induced surface charge density $\rho_{pol,i} = \mathbf{P}_i \cdot \hat{\mathbf{n}}_i$ and the fields attributed to it. In Fig. 4.3(a) we show the $\boldsymbol{k} = \mathbf{0}$ quasi-static results from collectively exciting a small chain with $N = 5$ particles at a separation of $\sigma = 2.1$.

The largest resonant peaks occur at the super-radiant dipole and quadrupole modes at 2.86 eV and 3.5 eV, respectively, as shown in the lower plot of Fig. 4.3(a). However, secondary peaks due to bright sub-radiant dipole modes are also visible in the optical cross-section at 3.19 eV and 3.53 eV. Here, the energies are blue-shifted compared to generalized Mie theory calculations due to the lack of phase retardation. The inset plots the energy of the N non-degenerate eigenvalues [67] as a function of σ. At large σ, all modes converge to the $l = 1$ mode of an isolated sphere. Only the super-radiant and the two bright sub-radiant modes marked by the colored boxes can be excited optically by a symmetric field, while the two dark sub-radiant modes are optically inactive as a result of the mirror symmetry of their charge distribution [113, 153, 158].

The physical mechanism behind the sub-radiant mode at 3.18 eV is illustrated by plotting $\mathbf{P}\cdot\hat{\mathbf{n}}$ in the upper part of Fig. 4.3(a). The charge density varies asymmetrically with respect to the center particle, which leads to near-fields that have odd parity upon negation of their coordinates [113]. Hence, they possess a finite dipole moment and can thus be optically excited. In contrast, dark sub-radiant modes, which lie close in energy to their bright counterparts (black lines in the eigenvalue plot in the inset of Fig. 4.3(a)) can become optically active upon end-excitation [153]. The charge density obtained by quasi-static calculations shown in Fig. 4.3(a) agrees well with the results from generalized Mie theory (section 4.3).

In chapter 5 we will consider conditions appropriate for waveguiding along MNP structures, shown in Fig. 4.3(b) are the results of exciting the leading particle within chains of increasing N at a separation of $\sigma = 2.1$, which demonstrate that end-excitation creates a sub-radiant band of energies at which radiative decay is minimized and efficient coupling to particle chains occurs. The cumulative dipole moments along the z-axis are plotted for chains with varying N. For $N = 5$, the sub-radiant mode at 3.18 eV gains magnitude with respect to the lowest energy super-radiant dipole mode at 2.86 eV. This trend continues for larger N and is accompanied by a gradual red-shift as indicated by the red arrow. We can further conclude that for chains with larger N and at small σ, a broad band emerges consisting of low energy sub-radiant modes. This is evident from the appearance of additional peaks associated with both bright and dark sub-radiant modes, which at $N = 50$ become a broad featureless

shoulder at the high energy side of the super-radiant dipole mode. The results of these quasi-static calculations should also apply to larger metallic nanoparticles governed by Maxwell's equations, with local dielectric properties that are governed by a free electron response.

4.5 MNP chains as efficient nano-antennas

As was stated earlier, MNP structures of sufficient size exhibit large field enhancements and intense scattering at super-radiant plasmon modes, making them excellent candidates for antennas in sub-wavelength plasmonic circuits [159, 160]. Small interparticle distances in assemblies of many MNPs, as in self-assembled MNP rings [19, 94], allow for a comparison between absorption and scattering losses resulting from strongly coupled MNP plasmons.

We illustrate this in Fig. 4.4, where partial scattering solutions to Mie theory are used to solve for the optical absorption (magenta) and scattering (blue) efficiencies of linear chains of varying length composed of 40 nm Au MNPs [33], surrounded by an effective index of refraction, $n = 1.5$. Each panel shows efficiencies of MNP chains with interparticle gaps of 1 nm (solid line) and 20 nm (dash line), composed of $N = 2$ **(A)**, 3 **(B)**, 6 **(C)**, and 10 **(D)** MNPs. For gaps of $g = 1$ nm, the super-radiant dipole mode is red-shifted from 685 nm for a dimer ($N = 2$) to 862 nm for $N = 10$, while for 20 nm gaps, weak plasmon coupling reduces the spectral shift to only 20 nm, which is further illustrated in the inset of Fig. 4.4A for chain lengths of up to $N = 15$. For

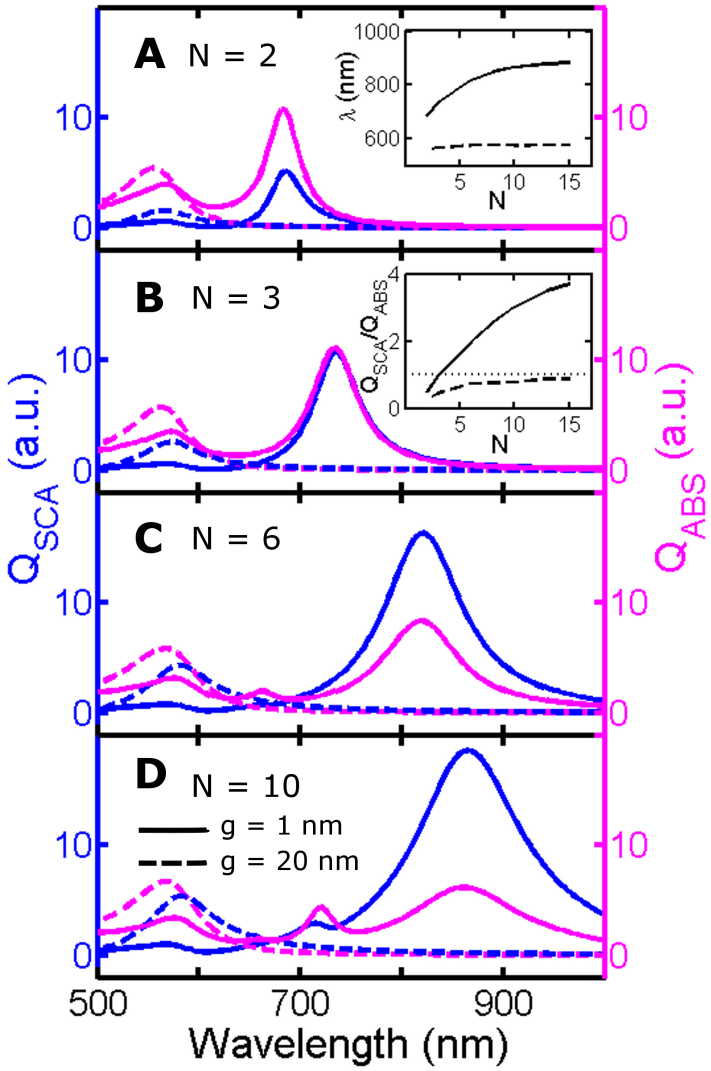

Figure 4.4 : Absorption and scattering efficiency of ordered MNP chains. **(A-D)** Scattering (Q_{SCA}, blue) and absorption (Q_{ABS}, magenta) efficiencies of linear chains composed of $N = 2$ **(A)**, 3 **(B)**, 6 **(C)**, and 10 **(D)** 40 nm gold MNPs. The efficiency Q is defined as the optical cross-section normalized by the geometric cross-section of the total number of MNPs. Spectra were calculated for gaps of $g = 1$ nm (solid line) and $g = 20$ nm (dashed line) between neighboring MNPs. The insets in **A** and **B** show the resonance maximum and the ratio of scattering and absorption efficiencies at the super-radiant plasmon mode for gaps of 1 and 20 nm as a function of MNP number, N. The dotted horizontal line in the inset in **B**, $Q_{SCA}/Q_{ABS} = 1$, is given as a reference to illustrate when scattering becomes more dominant than absorption.

both interparticle distances, the scattering efficiency at the super-radiant plasmon mode furthermore increases relative to the absorption efficiency with increasing N. This is shown in the inset of Fig. 4.4B where the ratio of Q_{SCA}/Q_{ABS} is plotted vs. N. However, only for $g = 1$ nm does scattering become more dominant than absorption for the ordered linear chains in Fig. 4.4. The larger scattering amplitude is due to the hybridization of higher order modes which result from increased coupling of closely spaced MNPs, insuring an increasing dipole moment as more MNPs are added along the length of the 1D MNP chain.

These results are consistent with calculations of MNP dimers [161] and heptamers [162], showing that radiation dominates the competition between scattering and absorption at the super-radiant mode, implying smaller ohmic losses and larger local fields at red-shifted plasmon energies. This allows one to minimize absorptive losses while maximizing electromagnetic field enhancements using closely spaced, strongly coupled MNPs in the design of efficient plasmonic nano-antennas.

4.6 Characterizing conductive contact using optical spectra

To take advantage of strongly coupled MNP plasmons in devices such as the before mentioned nano-antennas or in waveguiding applications, extremely small interparticle gaps of a few nanometers must be realized. This can be achieved using chemically prepared, self-assembled MNP structures [86, 163–165]. Large, periodic assemblies of MNPs can then be fabricated with a wide distribution of interparticle gaps, created

at high throughput via pre-designed patterns. Here, we look to characterize a single section of an experimentally prepared ring of MNPs [19, 86] assembled using a bottom-up approach.

Fig. 4.5A shows the SEM image of the Au MNPs under consideration taken from a section of the experimentally fabricated ring structure [94]. In order to access the entire surface plasmon response of the MNP segment, electrodynamic simulations of the local ring segment were carried out to validate and further interpret the experimental results of broadband extinction collected over a spectral range of $500 - 1,800$ nm. Fig. 4.5B shows the extinction spectra recorded with linear polarization both parallel and perpendicular to the local alignment of the MNPs, as indicated by the blue and red arrows in Fig. 4.5A, and plotted in Fig. 4.5B. The spectra for parallel polarization displays a strong peak at $1,400$ nm which showed strong polarization dependence along the quasi 1D MNP structure, as well as multiple peaks between 500 nm and $1,000$ nm.

Using the experimental MNP arrangement, we calculated polarized extinction spectra using the previously mentioned, partial scattering solution to Mie's theory, or generalized Mie theory (GMT) [69,78]. Fig. 4.5C shows the arrangement of 26 MNPs that were all assumed to be 40 nm spheres, spaced at least 1 nm apart. Although this presents a simplification of the actual system where the MNPs are highly faceted, GMT has the advantage of being able to compute the collective optical response of a large number of MNPs while including many multipoles. The calculated polarized

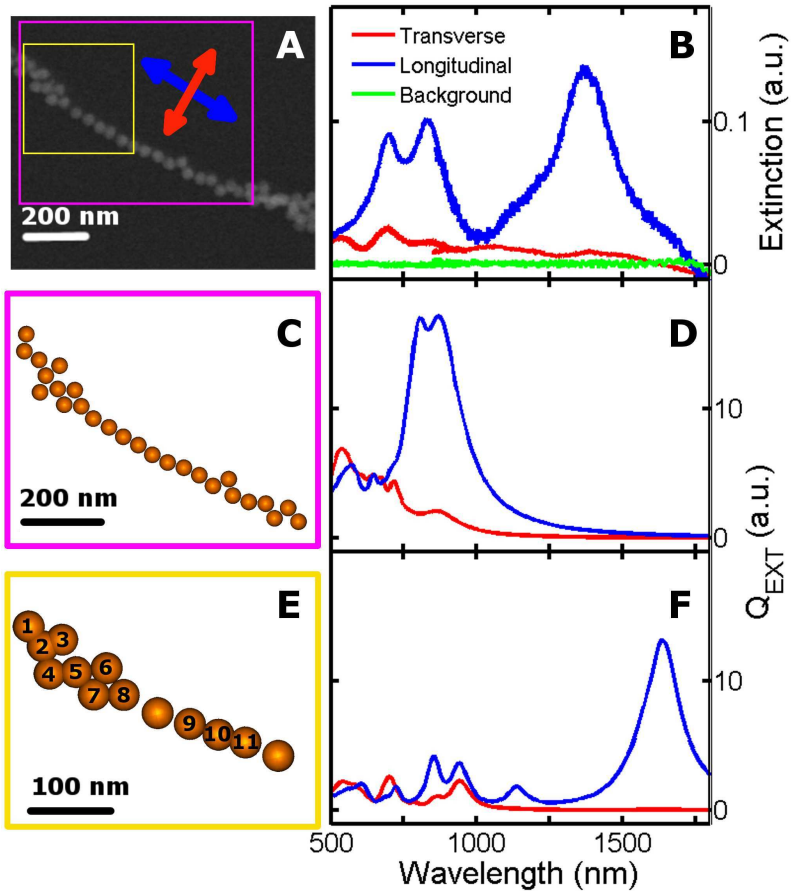

Figure 4.5 : Experimental and simulated extinction spectra for a segment of an MNP ring. **(A)** SEM image of a ring segment composed of 40 nm Au MNPs. **(B)** Extinction spectra of the ring segment in **A** recorded with excitation polarization parallel (blue) and perpendicular (red) to the 1D MNP alignment direction. **(C** and **D)** Calculated extinction for the ring segment marked by the magenta square in **A**. The modeled MNP arrangement in **C** was taken from the SEM image, keeping the minimum surface-to-surface separation between neighboring MNPs greater than 1 nm. **(E** and **F)** finite-element calculations for the ring segment marked by the yellow square in **A**. For the finite-element calculations, the MNPs labeled $1-8$ and $9-11$ were allowed to touch and hence coupled conductively.

extinction spectra (Fig. 4.5D) show multiple plasmon resonances for wavelengths shorter than $1,000$ nm, qualitatively reproducing the experimental results except for the plasmon peak at $1,400$ nm, which is absent in the GMT calculations. Increasing

the number of MNPs in the calculations did not push the longest wavelength surface plasmon peak beyond $1,000$ nm, consistent with previous results showing that the infinite chain limit is reached for about 10 MNPs [78, 155]. Because GMT matches the experimental results well for wavelengths below $1,000$ nm the collective response in this wavelength range is assigned to mostly capacitive plasmon coupling between non-touching MNPs.

The longest wavelength surface plasmon resonance can be explained by conductive plasmon coupling for touching MNPs. Because GMT can only solve the optical response for non-touching MNPs, we used finite element methods requiring significantly more computer resources to solve Maxwell's equations, and simulate the MNP assembly shown in Fig. 4.5E containing only the first 13 MNPs. The calculated extinction spectrum with longitudinal polarization in Fig. 4.5F shows a strong surface plasmon resonance at $1,600$ nm as well as several multipolar peaks with lower intensities. For this MNP arrangement conductive contact for MNPs $1-8$ and $9-11$ was assumed. However, because of the limited resolution of SEM it was not clear which MNPs were actually touching. Therefore, different MNP arrangements with varying numbers of touching MNPs were simulated. The geometry shown in Fig. 4.5E resulted in the best qualitative agreement between the experimental (Fig. 4.5B) and calculated spectra (Fig. 4.5F). Further optimization of the MNP shape and assembly geometry could in principle lead to better agreement between experiment and theory, but the main conclusion here is that it is necessary to consider touching MNPs to

explain the longest wavelength plasmon mode in the experimental spectra.

4.7 Conclusions

In conclusion, we investigated the effects of higher order plasmon modes of finite MNP chains on their collective optical properties. We showed that close interparticle spacings between MNPs facilitate strong plasmon coupling resulting in the formation of super and sub-radiant plasmon modes in linear 1D chains of MNPs, which can be characterized by intrinsic eigenmodes or their unique charge density profiles. By considering energy decay via ohmic loss or far-field radiation at energies corresponding to the super-radiant plasmon mode, linear chains of sufficient size were shown to be model candidates for future plasmonic antennas. Finally, by analyzing the optical extinction in fabricated MNP assemblies with both analytical scattering methods and grid-based techniques, the effects of conductive contact and capacitive coupling were identified by noting simple differences in their respective optical spectra.

Chapter 5

Energy transport along MNP structures via sub-radiant plasmon modes[4]

Thus far, we have demonstrated that when MNP separations become small, higher order plasmon modes play a significant role in the optical characteristics of MNP chains. Close interparticle distances result in strong plasmonic coupling, a pre-requisite for the formation of super and sub-radiant dipole modes. Our next task is to apply these results to understand how sub-radiant plasmon modes contribute to transport properties when MNP structures, such as the 1D chains considered previously, are excited at one end, as would be performed in a waveguiding experiment.

5.1 Finite MNP structures for waveguiding

A fundamental challenge in systems tasked with energy transport at the nanoscale, is to overcome signal attenuation along structures with subwavelength dimensions. Finite structures of MNPs have the potential to transport electromagnetic energy via

[4] This chapter is based upon the manuscripts: (1) "Energy transport in metal nanoparticle chains via sub-radiant plasmon modes" by Britain Willingham and Stephan Link, Opt. Express, vol. 19, pp. 6450–6461, 2011. (2) "Electromagnetic Energy Transport in Nanoparticle Chains via Dark Plasmon Modes" by David Solis, Jr., Britain Willingham, Scott L. Nauert, Liane S. Slaughter, Jana Olson, Pattanawit Swanglap, Aniruddha Paul, Wei-Shun Chang, and Stephan Link, Nano Lett., vol. 12, pp. 1349–1353, 2012.

the excitation of their localized surface plasmons [15, 166]. The efficient coupling of light to surface plasmons provides a pathway to distribute and direct energy among an ensemble of particles [45, 167–169], but is often accompanied by losses due to ohmic heating and far-field scattering at optical frequencies. Radiative relaxation can be minimized by coupling to coherent electron oscillations whose optical properties show a sub-radiant nature, providing a useable bandwidth at which leaky transmission is suppressed.

To date, energy propagation in MNP assemblies has mainly been investigated by determining the dispersion curves of surface plasmon polaritons (SPPs) along infinite structures [45, 146–151]. Calculations that include far-field interactions as well as retardation and losses for linear 1D assemblies of MNPs with finite sizes give rise to complex dispersion curves with large bandwidths and substantial SPP group velocities [67,149]. However, these studies were limited to large interparticle distances on the order of the particle radius since only dipole interactions were considered [45, 67, 146–151].

In comparison to infinite structures, the use of finite MNP chains as optical waveguides provides a more realistic system [151, 155, 170, 171], as practical applications would involve well defined finite assemblies of MNPs [172–175]. Here, non-degenerate dipole modes appear as sub-radiant plasmon resonances that have suppressed radiative losses when compared to super-radiant plasmon modes [79, 154, 176, 177].

In order to appropriately establish MNPs as prospective candidates for topical

waveguides, close interparticle spacing and strong coupling which involves the hybridization between higher order plasmon modes must be considered. As previously discussed, a bottom-up aproach using chemically synthesized MNPs in finite nanostructures allows for strong coupling throughout, but sacrifices periodic positioning obtained by top-down methods, often resulting in structures with random positions and variable interparticle spacings [178]. Thus, a theoretical investigation that considers the relationship between optical spectra and SPP propagation in finite MNP chains at close interparticle separations, but also includes the effects of local disorder in particle positions, demands further attention.

5.2 SPP propagation in linear, finite chains of MNPs

Here, we use the exact solution to Maxwell's equations for spheres to demonstrate that the propagation of SPPs shows reduced decay with decreasing interparticle separations. End excitation of linear 1D chains of MNPs reveals a band of sub-radiant modes whereby the decay of surface plasmon polaritons due to radiative losses is minimized. Optical spectra are used to locate sub-radiant modes, and confirm that their excitation results in the most efficient energy transfer throughout the optical spectrum.

Fig. 5.1 displays SPP near-field intensities along a chain of $N = 50$ Ag nanoparticles with $a = 25$ nm for different σ, where the coefficients for the incident field were set to zero for all but the first MNP. The intensity profiles support the notion that

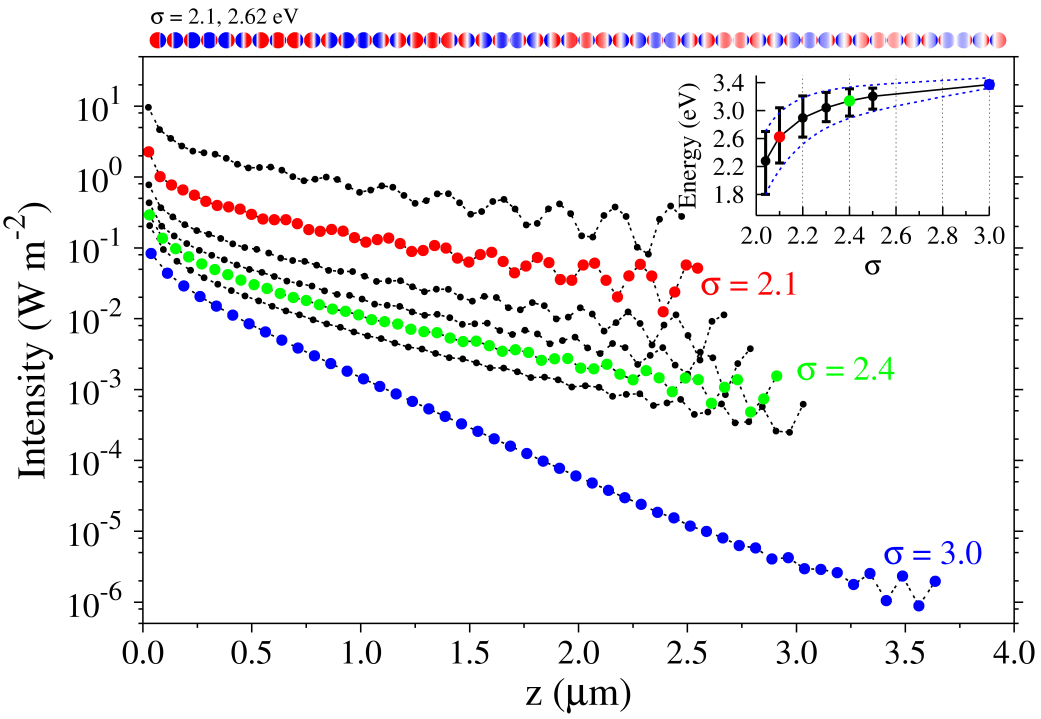

Figure 5.1 : SPP near-field intensity profiles along Ag nanoparticle chains with $a =$ 25 nm and $N = 50$ as σ is varied. The chains are excited at the end particle and the intensity values are taken at the interparticle gaps. Excitation energies (eV) are chosen to maximize SPP propagation and are shown in the inset as a function of σ. Error bars represent the bandwidth for SPP propagation via sub-radiant plasmon modes. Top: Real part of the surface charge density along the z-axis for a chain with $\sigma = 2.1$ after end excitation at 2.62 eV.

sub-radiant modes efficiently absorb incident radiation, sustain suppressed radiative losses, and thereby minimize SPP decay. The near-field intensity $I = |\boldsymbol{E_s}|^2\sqrt{\varepsilon_0/\mu_0}$ was determined at successive centers of the particle junctions along the z-axis, where $\boldsymbol{E_s}$ is the total scattered electric field including near and far-field contributions, and ε_0 and μ_0 are the vacuum permittivity and permeability, respectively. The chain was

end-excited with multiple wavelengths of longitudinally polarized plane waves, exciting both bright and dark sub-radiant modes [153]. I was then fit to an exponential decay, $I = I_0 e^{-bz}$ with decay constant, b. Fig. 5.1 shows the intensity profiles for the excitation energies that yield maximum SPP propagation at each σ. For $\sigma = 3.0$, the decay follows previous calculations showing maximum SPP propagation for excitation energies near the single particle resonance [15]. However, smaller separations minimize SPP decay at excitation energies corresponding to sub-radiant modes, which is a direct result of plasmon interactions through higher order modes in finite particle chains.

The inset to Fig. 5.1 relates the energies at which maximum propagation takes place to each interparticle separation, σ. With decreasing σ, an increasingly broad band of energies is observed where exponential decay of I takes place, coinciding with the sub-radiant modes described in chapter 4. Here the loss is mainly dominated by absorption as the intensity of the sub-radiant modes increases upon end-excitation (see section 4.4). The SPP amplitudes decay exponentially like a system of damped harmonic oscillators, consistent with a free electron response. Shown on top of Fig. 5.1 is the surface charge density, $\mathcal{R}e\{\rho_{pol}\}$, at an excitation energy of 2.62 eV and an interparticle spacing $\sigma = 2.1$. The induced polarization charge density alternates along the chain, and displays even symmetry with respect to the center of the nanoparticle chain. This is characteristic of exciting a dark sub-radiant plasmon mode [153], which supports maximum SPP propagation with minimal radiative decay [79].

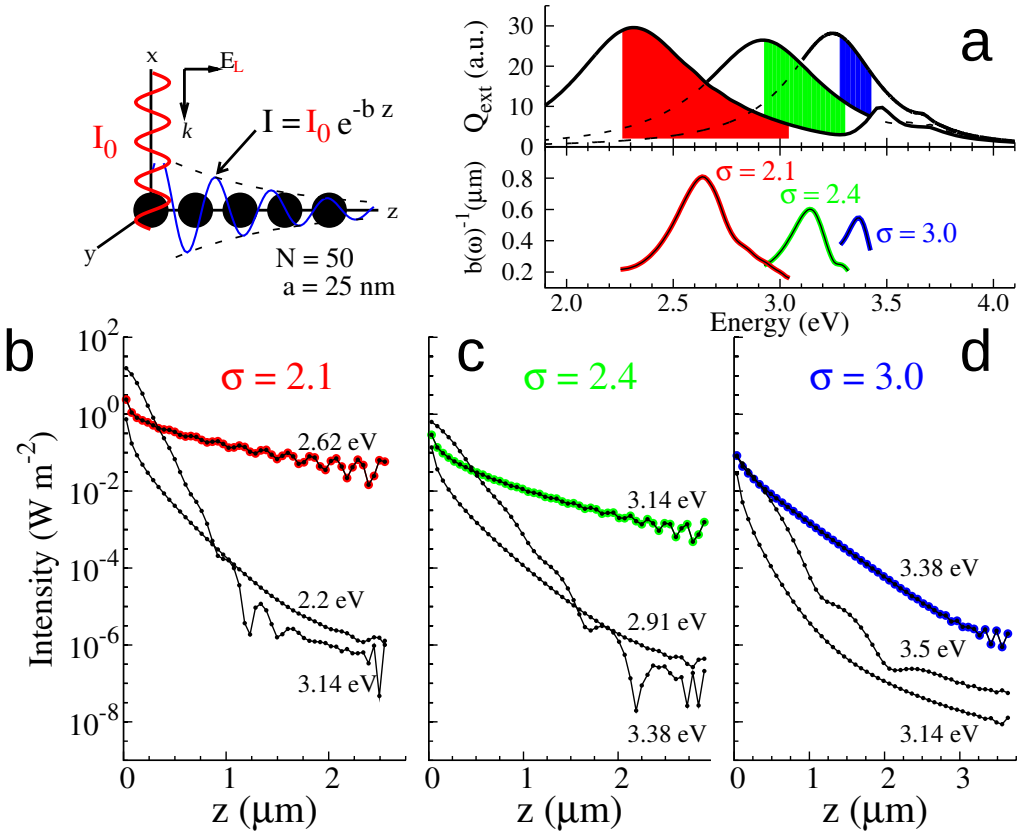

Figure 5.2 : Correlation between optical spectra and SPP decay for $N = 50$ chains of Ag nanoparticles with a radius of $a = 25$ nm for varying $\sigma = 2.1, 2.4$, and 3.0. Upper left panel schematically illustrates the asymmetric end-excitation used in the calculations of SPP propagation, where intensity values are sampled at the nanoparticle gaps. **(a)** Plot of the $1/e$ decay length for each σ showing an energy band where maximum SPP propagation takes place. Accompanying optical extinction spectra confirm the assignment of this energy band to sub-radiant plasmon modes. **(b)**, **(c)**, and **(d)** show intensity profiles where a maximum decay length is obtained at each separation σ (color plots), compared to excitation at energies just outside the bands highlighted in **(a)**, which leads to strongly non-exponential intensity profiles.

In Fig. 5.2 we further verify the sub-radiant nature of SPP propagation in finite nanoparticle chains by correlating energies at which maximum propagation takes place to the optical extinction when the chain is excited collectively. Shown in the lower part of Fig. 5.2(a) are the $1/e$ SPP decay lengths as a function of excitation

energy for the three interparticle separations highlighted in Fig. 5.1. Comparison to the corresponding optical extinction spectra (top part of Fig. 5.2(a)) illustrates that maximum SPP propagation takes place at energies which correspond to sub-radiant plasmon modes for all σ considered. At energies which lie outside this energy band, the intensity fails to decay exponentially, uncharacteristic of pure propagating SPPs. This can be seen from the intensity profiles for the three analyzed separations at different excitation energies, as shown in Figs. 5.2(b)-5.2(d). In particular, at $\sigma = 2.1$, (Fig. 5.2(b)), an excitation energy of 2.62 eV results in a maximum $1/e$ decay length of 0.81 μm. Excitation at energies outside the band corresponding to sub-radiant modes (and highlighted in Fig. 5.2(a)), e.g. at 3.14 eV and 2.2 eV, drastically reduces SPP propagation. The same trend is also observed for separations of $\sigma = 2.4$ and $\sigma = 3.0$, shown in Fig. 5.2(c) and Fig. 5.2(d). These results suggest that low-loss SPP propagation occurs via excitations of sub-radiant dipole modes.

Interestingly, for the smallest interparticle separations, the excitation band for maximum SPP propagation partially overlaps with the super-radiant plasmon mode, possibly due to enhanced near-field coupling at close distances. Although an exponential intensity decay is observed (which is the definition of the energy band in Fig. 5.2(a) and the inset of Fig. 5.1), the SPP decay length is significantly shorter for excitation at energies corresponding to the super-radiant mode.

5.3 Group velocity of SPPs in finite chains of MNPs

The results presented so far have shown that SPP damping is strongly suppressed for sub-radiant modes. However, it is also necessary to examine the group velocity of the propagating SPPs, which can be obtained from the SPP dispersion [45]. Shown in Fig. 5.3 is a dispersion curve at energies corresponding to the sub-radiant plasmon modes for an $N = 50$ chain of Ag nanoparticles with $a = 25$ nm separated by $\sigma = 2.1$. The association between SPP propagation and sub-radiant plasmon modes in this finite chain is illustrated by the red colored region, corresponding to the same colored part in the optical extinction spectrum plotted in Fig. 5.2(a). The wave-number, $k_{||}$, for a particular incident excitation energy with longitudinal polarization was obtained by fitting the $\boldsymbol{E_s} \cdot \hat{\mathbf{z}}$ components along the particle chain to the equation of a damped harmonic oscillator (shown in inset). For excitation at 2.62 eV, corresponding to a sub-radiant mode, the decay constant, b, of the damped harmonic oscillator equation is taken to be the exponential decay parameter in Fig. 5.2(a). For comparison, near the single particle plasmon resonance at 3.45 eV, excitation of localized plasmons leads to large radiative and intrinsic damping and therefore inefficient coupling along the Ag nanoparticle chain.

The slope of the dispersion curve determines the SPP group velocity ν_g [152]. In the region of minimum SPP decay, ~ 2.62 eV, we find that the group velocity is $\nu_g/c \sim 0.3$, where c is the speed of light in vacuum. In addition to the small damping and large group velocity for SPPs excited via sub-radiant plasmon modes, it is important to

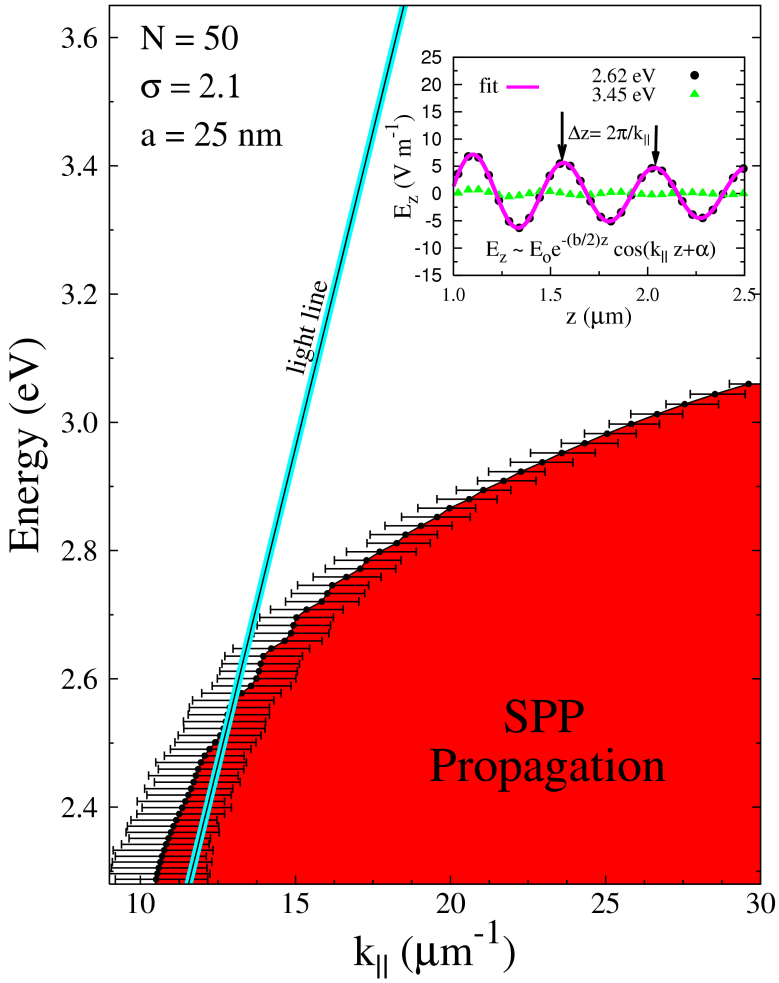

Figure 5.3 : Dispersion relation for SPPs supported by a Ag nanoparticle chain with $a = 25$ nm and $N = 50$ at $\sigma = 2.1$. The red colored region denotes the energy band formed by the sub-radiant plasmon modes at which minimum SPP decay is found. The inset illustrates the method used to extract the propagating wave-number $k_{||}$ within the sub-radiant band and compares collective (2.62 eV) to localized excitation (3.45 eV).

point out that the dispersion curve in Fig. 5.3 lies below the light line within the error of the fitting analysis. This is consistent with low losses due to minimized radiative decay as observed from the optical scattering spectra. Furthermore, it should be

pointed out that the dispersion relation for the sub-radiant plasmon modes in these Ag particle chains resembles the behavior of continuous plasmonic nanowires [179], which support long propagation distances due to reduced radiative decay [180–182].

In Table 5.1, we present SPP propagation decay constants b [μm^{-1}] for linear chains of $N = 50$ Ag nanoparticles with sizes ranging from the quasi-static limit to $a = 50$ nm. For increasing σ and decreasing a, the decay constant increases, denoting smaller propagation lengths. Smaller σ results in reduced decay constants as multipolar contributions lead to suppressed radiative losses when excited at energies corresponding to the sub-radiant modes. For $a = 50$ nm and $\sigma = 2.1$ the $1/e$ propagation length is ~ 3 μm when excited at 2.47 eV, nearly twice as large when compared to interparticle separations of $\sigma = 3.0$. For each particle size, the excitation energies that yield minimum SPP decay are easily correlated to the optical spectra, and lie between the main dipole resonance and the quadrupole mode. The width of this band broadens for close interparticle separations, providing a unique optical window for excitation of sub-radiant modes within which efficient energy transfer takes place. Particles with sizes near the quasi-static limit displayed decay profiles that were in very good agreement with electrostatic calculations. The energy propagation in chains of such small sizes is interpreted to be supported by the optical near-field and its dependence on higher order multipole modes, especially for small separations σ.

Table 5.1 : **Decay constants $b(\sigma)$ as function of Nanoparticle Radius a.**

a[nm]	$b(2.1)[\mu\text{m}^{-1}]$	$b(2.4)[\mu\text{m}^{-1}]$	$b(3.0)[\mu\text{m}^{-1}]$
0[a]	12.0	18.3	NA[b]
10	6.9	9.4	NA[b]
25	1.23	1.66	2.2
50	0.35	0.46	0.67

[a]quasi-static limit

[b]the intensity profiles could not be fit to an exponential decay

5.4 The effects of local disorder on SPP propagation along close-packed 1D structures

At optical energies, sub-radiant plasmon modes have shown to provide the backbone for propagating SPPs along linear 1D structures. The large bandwidth occurring for close interparticle separations is expected to apply to more general MNP systems as well, like the one shown in Fig. 5.4, where the lack of local symmetry can lift the eigenmode degeneracy, resulting in even broader sub-radiant bands, with large group velocities and minimal signal attenuation for a number of frequencies in the optical spectrum.

To create structures that have been fabricated from the combination of top-down methods and the self-assembly of MNPs [6,178], we used a collision-driven, molecular dynamics algorithm [183, 184] to create close-packed 2D structures within an imaginary box, containing $N = 1,200$ Au MNPs placed in random positions within a single

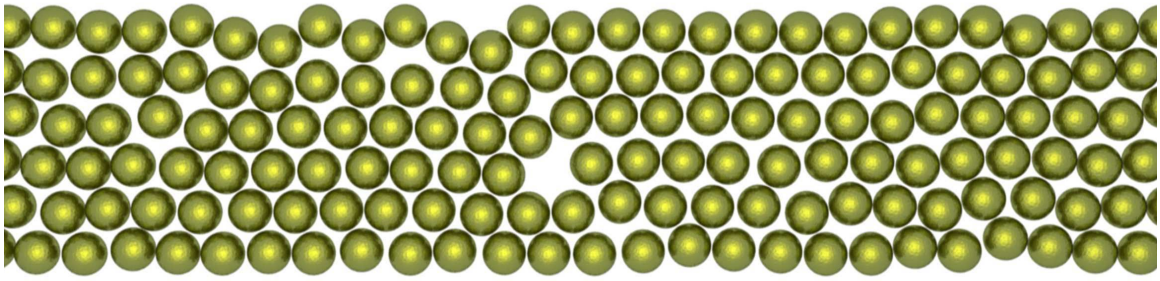

Figure 5.4 : Section of a MNP assembly, containing $N = 1,200$ MNPs, showing closely spaced 50 nm Au MNPs with random positions to account for local disorder. All particle-to-particle separations are ≥ 1 nm.

layer (Fig. 5.4).

To perform waveguiding calculations on par with an experiment, 15 multipole modes were used in the expansion of scattering fields from each MNP, while the solution method was altered to accommodate large collections of spherical particles as well as incident fields corresponding to the fundamental TEM_{00} mode of a laser. Here, the integral representations of the beam expansion coefficients were approximated as analytical expressions [185]. The Gaussian beam, expressed within its local frame, is then translated to particle centers using the vector spherical wave addition theorem. Incident coefficients are subsequently implemented within the system of linear equations, and the appropriate partial scattering solutions are solved as in the plane wave case [69].

Fig. 5.5 shows the near-field intensity along the entire MNP assembly of Fig. 5.4, embedded in a refractive index of $n = 1.5$, resulting from laser excitation polarized along its length (the x-axis) at 785 nm. Energy propagation due to the capacitive

coupling and strong hybridization between higher order modes is clearly seen. Intensity is present at lengths $\sim$ 10 μm from the laser source, a noticeable increase in propagation when compared to 1D assemblies of MNPs with larger interparticle distances which couple primarily via dipole modes [166, 171].

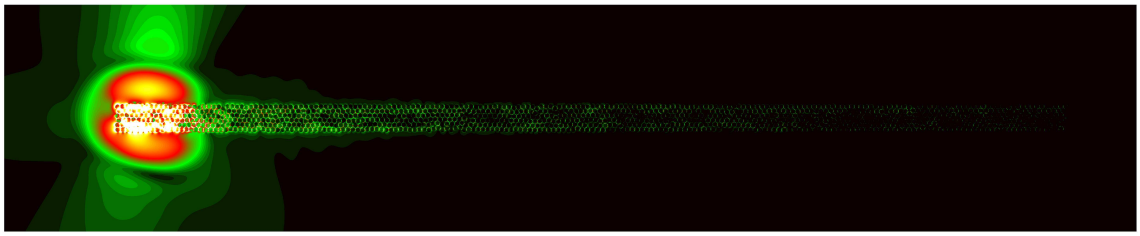

Figure 5.5 : Near-field intensity of the laser profile and plasmon propagation in a 1,200 MNP chain for an excitation wavelength of 785 nm. The propagation length corresponding to a $1/e$ decay length and determined by a width-average line-section was $L_0 = 1.7$ μm.

To access the propagation length along each MNP structure, width-averaged line sections were obtained by averaging the intensity values of the calculated near-field for each $1,200$ MNP chain over a $n_x \times n_y$ grid in the MNP plane at $(z = 0)$. External values of the electromagnetic fields were sampled just outside the structure boundary and throughout the interstitial space between constituent MNPs. Values lying in the y-direction, perpendicular to the long-axis of the chain and at the same x-coordinate, were then summed up for each of the n_x columns. Of the n_y positions at each x, only values external to the particle surfaces were accumulated to form the width-averaged line section, allowing each final value along x to be normalized by the total number of collected points at each respective position.

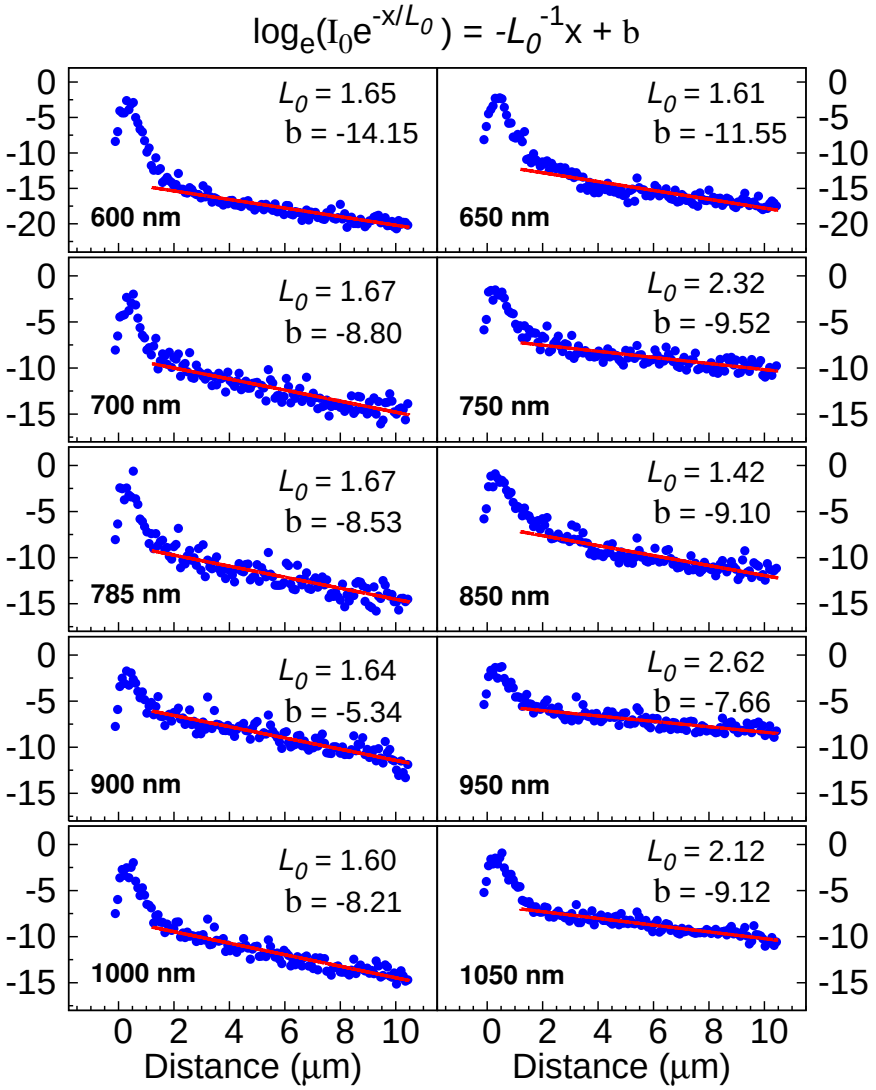

Figure 5.6 : Decay of the width-averaged near-field intensity along a MNP chain for different excitation wavelengths. The intensity is plotted on a logarithmic scale and fitting of the data points starting at the right of the laser response yielded $1/e$ propagation distances L_0.

Fig. 5.6 shows calculated decay lengths for propagation along a MNP structure for different laser excitation wavelengths. As in linear 1D chains, an excitation bandwidth is formed where efficient surface plasmon propagation occurs. From $600 - 1050$ nm

$L_0 > 1.6$ μm with a $1/e$ propagation distance as long as 2.62 μm at 950 nm. In comparison, for laser excitation near the single particle Mie resonance of 550 nm, no long range energy propagation was found [6]. Here, bridging the momentum gap between the SPP and incident radiation via the excitation of localized surface plasmons becomes increasingly difficult at such high energies and in close proximity to Au's interband edge [181, 186].

The previous calculations show that by creating larger 2D structures of closely packed MNPs an increase in propagation length was found when compared to 1D linear chains (see section 5.3), a trade off between propagation length and subwavelength confinement observed in other plasmonic waveguides [187]. As of now, it is unclear whether the mechanism behind such large propagation distances is a sub-radiant response. Due to the broadening of the sub-radiant band at closer interparticle separations, we expect the disordered arrangements previously considered to possess collective sub-radiant resonances within the eigenmode spectrum of an ordered 2D MNP arrangement with all interparticle spacings set at the minimum distance of 1 nm. Therefore, to verify a sub-radiant mode through charge plots of a hexagonal closed-packed (hcp) system at the same excitation energy, would further lend weight to the sub-radiant nature of energy propagation seen in realistic arrangements with local disorder.

In Fig. 5.7(A) we plot the induced polarization charge density along a hcp array of MNPs when excited collectively by a plane wave polarized along x-axis at 785 nm.

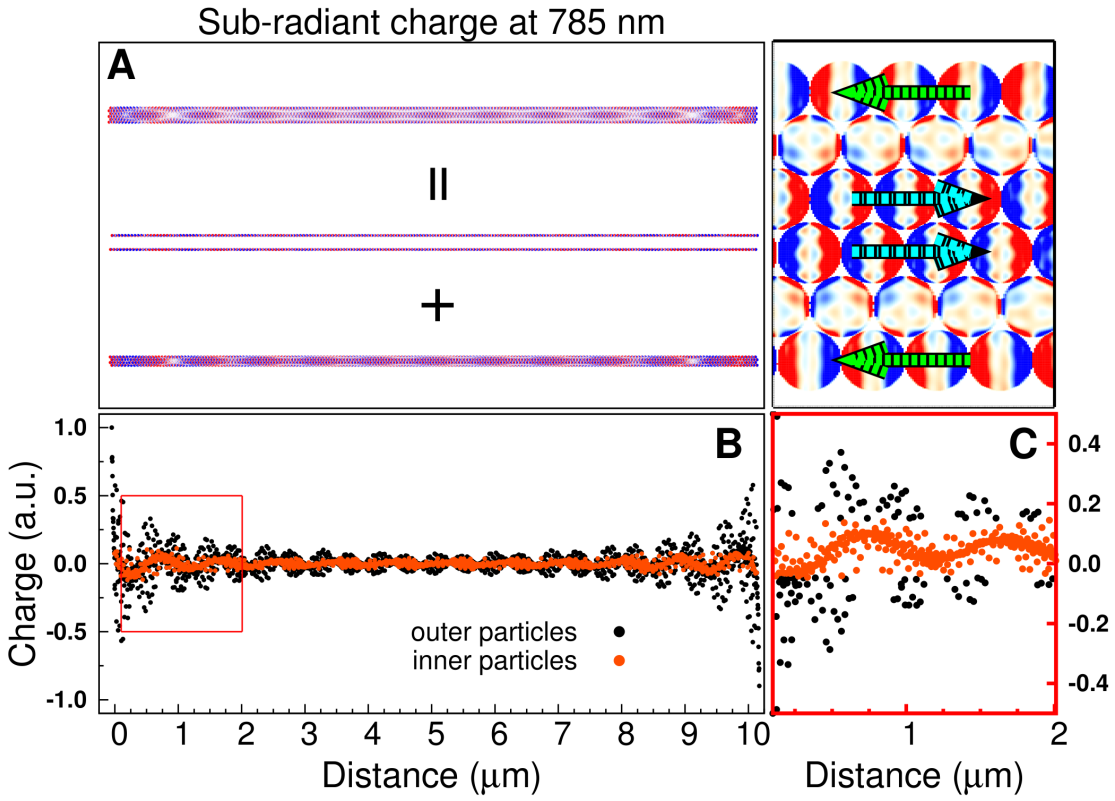

Figure 5.7 : Sub-radiant response of a hexagonal close-packed array of 50 nm Au MNPs upon coherent plane wave excitation at 785 nm. **(A)** The sub-radiant nature of the excited plasmon modes is identified by bands of alternating positive (red) and negative (blue) charge domains along the length of the chain. Charge contributions can be separated into domains of different phase, localized to regions on the edge and within the interior of the MNP assembly as further highlighted by the higher magnification charge plot in the right-hand panel. **(B)** Width-averaged line section of the surface charge highlights the standing wave oscillations, characteristic of the sub-radiant eigenmode of the system. **(C)** Closer inspection (red-box) of the charge oscillations illustrates that the resonant domains are roughly 180° out of phase.

As in the 1D chain considered in section 4.3 of chapter 4, the sub-radiant response is characterized by positive and negative charge domains which alternate along the length of the MNP structure [78]. This phase difference also extends along the y-direction, as can be seen in the upper right panel, where MNPs offset in the y-direction

to one another also possess dipole domains that are $\sim 180^{\circ}$ out of phase. To further see this, in Fig. 5.7(B) we plot width-averaged line section values for the surface charge plot* collected along MNPs forming the edge of the 2D assembly (black points) and along the interior MNPs (orange points). As shown, the charge oscillations show standing wave patterns characteristic of a normal mode of the system, while closer inspection (red-box and Fig. 5.7(C)) of the charge indeed confirms the phase difference of each domain and the sub-radiant optical response at 785 nm.

Having confirmed the sub-radiant nature of the hcp arrangement, we now compare the effects of local disorder on the sub-radiant plasmon propagation at 785 nm. In Fig. 5.8 we compare the propagation lengths of the hcp MNP structures against assemblies in which MNP positions were randomly created. In all cases considered, local disorder resulted in an increased plasmon propagation distance, similar to results observed in photonic quasicrystals [188]. These results show that energy propagation increases for local disorder. Propagation along hcp structures at even lower energies may sample sub-radiant energies outside the eigenmode spectrum of the disordered arrays resulting in very large propagation lengths. Though, this would also occur if MNPs were simply placed in even closer, more tightly spaced disordered arrangements or possibly in conductive contact. Either result or system points to a very promising future for chemically prepared, self-assembled structures whose intrinsic heterogeneity

*Calculations of the width-averaged charge followed the same method as that of the near-field intensity, deviating only by accumulating x and y values within the boundaries and along the surface of individual particles

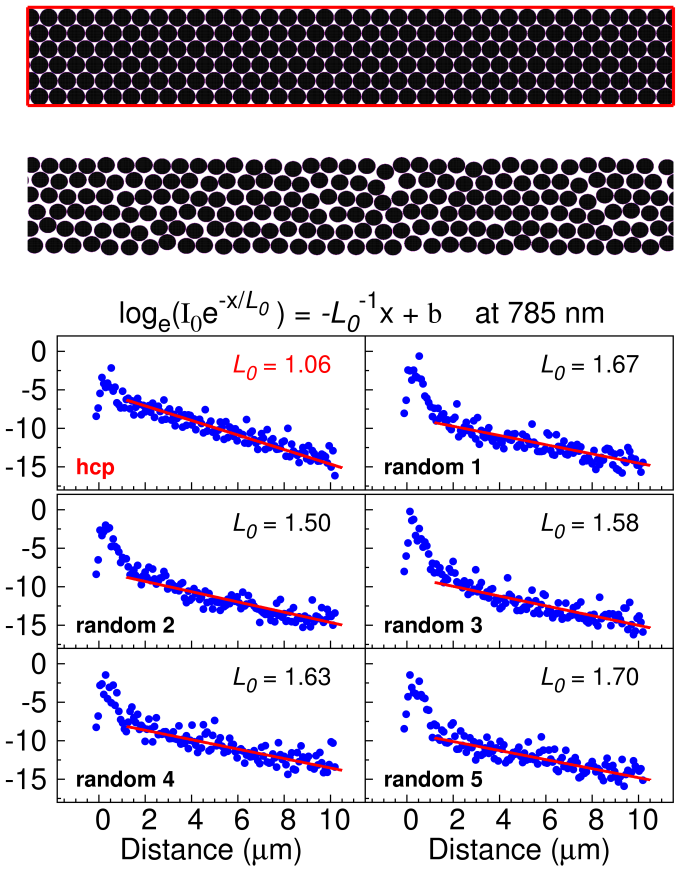

Figure 5.8 : Comparison of the plasmon propagation distances for a 2D hexagonal closed-packed Au MNP chain vs. five randomly created MNP assemblies in which disorder has been introduced. Excitation at 785 nm for a hexagonal close-packed arrangement of 50 nm Au MNPs resulted in a shorter propagation distance compared to chain structures of the same length with added local disorder.

would act to suppress unwanted signal attenuation, allow for excitation along any part of a MNP waveguide, and provide large bandwidths for information transport in printed nanocircuits of the future.

5.5 Conclusions

In conclusion, using generalized Mie theory we have shown that propagating SPPs along linear chains of Ag nanoparticles exhibit maximum propagation distances at small separations when exciting sub-radiant plasmon modes. As the number of particles increases, these discrete modes form an excitation band at which radiative losses are minimized, becoming increasingly broad at small interparticle separations.

Laser excitation of surface plasmons along assemblies of 1,200 Au MNPs arranged to replicate experimentally fabricated structures consistently resulted in $1/e$ propagation lengths over 1 μm, while local disorder was shown to increase propagation along these closed-packed arrays. Electromagnetic energy transport by optically induced SPPs in collections of closely spaced MNPs offers distinct advantages for creating optical interconnects between other waveguides since SPPs can easily be transported around sharp corners or can be split, for example, into two SPPs in a 'T' - like nanoparticle geometry. The results presented here also point to the use of chemical methods to arrange nanoparticles in close proximity to each other, thereby maximizing SPP propagation as well as the excitation bandwidth formed by the sub-radiant plasmon modes.

Bibliography

[1] I. Freestone, N. Meeks, M. Sax, and C. Higgitt, "The lycurgus cup - a roman nanotechnology," *Gold Bulletin*, vol. 40, pp. 270–277, 2007.

[2] G. Mie, "Beitrge zur optik trber medien, speziell kolloidaler metallsungen," *Ann. Phys.*, vol. 25, p. 377, 1908.

[3] U. Kreibig and M. Vollmer, *Optical properties of metal clusters*. New York: Springer, 1995.

[4] C. Bohren and D. Huffman, *Absorption and Scattering of light by small particles*. New York: John Wiley & Sons, 1983.

[5] K. Willets and R. P. V. Duyne, "Localized surface plasmon resonance spectroscopy and sensing," *Annu. Rev. Phys. Chem.*, vol. 58, pp. 267–297, 2007.

[6] D. Solis Jr., B. Willingham, S. L. Nauert, L. S. Slaughter, J. Olson, P. Swanglap, A. Paul, W.-S. Chang, and S. Link, "Electromagnetic energy transport in nanoparticle chains via dark plasmon modes," *Nano Lett.*, vol. 12, pp. 1349–1353, 2012.

[7] S. Lal, S. Link, and N. J. Halas, "Plasmonics: From surface plasmon sensing to plasmon waveguiding," *Nat. Photonics*, vol. 1, pp. 641–648, 2007.

[8] C. Langhammer, I. Zoric, B. Kasemo, and B. M. Clemens, "Hydrogen storage in Pd nanodisks characterized with a novel nanoplasmonic sensing scheme," *Nano Lett.*, vol. 7, pp. 3122–3127, 2007.

[9] S. Dominguez-Medina, S. McDonough, P. Swanglap, C. F. Landes, and S. Link, "In situ measurement of bovine serum albumin interaction with gold nanospheres," *Langmuir*, vol. 28, pp. 9131–9139, 2012.

[10] R. A. Sperling, P. R. Gil, F. Zhang, M. Zanella, and J. W. Parak, "Biological applications of gold nanoparticles," *Chem. Soc. Rev.*, vol. 37, pp. 1896–1908, 2008.

[11] V. M. Shalaev, "Optical negative-index metamaterials," *Nat. Photonics*, vol. 1, pp. 41–48, 2007.

[12] N. Liu, H. Guo, L. Fu, S. Kaiser, H. Schweizer, and H. Giessen, "Three-dimensional photonic metamaterials at optical frequencies," *Nat. Mater.*, vol. 7, pp. 31–37, 2008.

[13] H. J. Lezec, J. A. Dionne, and H. A. Atwater, "Negative refraction at visible frequencies," *Science*, vol. 316, pp. 430–432, 2007.

[14] J. Valentine, S. Zhang, T. Zentgraf, E. Ulin-Avila, D. A. Genov, and G. Bartal, "Three-dimensional optical metamaterial with a negative refractive index," *Nature*, vol. 455, pp. 376–U32, 2008.

[15] M. Quinten, A. Leitner, J. R. Krenn, and F. R. Aussenegg, "Energy transport in Ag metal nanoparticle chains," *Opt. Lett.*, vol. 23, pp. 1331–1333, 1998.

[16] S. A. Maier and H. A. Atwater, "Plasmonics: Localization and guiding of electromagnetic energy in metal/dielectric structures," *J. Appl. Phys.*, vol. 98, p. 011101, 2005.

[17] A. Tcherniak, J. W. Ha, S. Dominguez-Medina, L. S. Slaughter, and S. Link, "Probing a century old prediction one plasmonic particle at a time," *Nano Lett.*, vol. 10, pp. 1398–1404, 2010.

[18] L. Slaughter, W.-S. Chang, , and S. Link, "Characterizing plasmons in nanoparticles and their assemblies with single particle spectroscopy," *J. Phys. Chem. Lett.*, vol. 2, pp. 2015–2023, 2011.

[19] W.-S. Chang, L. S. Slaughter, B. P. Khanal, P. Manna, and E. R. Zubarev, "One-dimensional coupling of gold nanoparticle plasmons in self-assembled ring superstructures," *Nano Lett.*, vol. 9, pp. 1152–1157, 2009.

[20] L. Novotny, "Effective wavelength scaling for optical antennas," *Phys. Rev. Lett.*, vol. 98, p. 266802, 2007.

[21] C. Sönnichsen, T. Franzl, T. Wilk, G. von Plessen, J. Feldmann, O. Wilson, and P. Mulvaney, "Drastic reduction of plasmon damping in gold nanorods," *Phys. Rev. Lett.*, vol. 88, p. 077402, 2002.

[22] J. J. Mock, M. Barbic, D. R. Smith, D. A. Schultz, and S. Schultz, "Shape effects in plasmon resonance of individual colloidal silver nanoparticles," *J. Chem. Phys.*, vol. 116, pp. 6755–6759, 2002.

[23] L. S. Slaughter, Y. Wu, B. A. Willingham, P. Nordlander, and S. Link, "Effects of symmetry breaking and conductive contact on the plasmon coupling in gold nanorod dimers," *ACS Nano*, vol. 4, pp. 4657–4666, 2010.

[24] N. W. Ashcroft and N. D. Mermin, *Solid State Physics*. Saunders Co., 1976.

[25] M. Scheffler, M. Dressel, M. Jourdan, and H. Adrian, "Extremely slow drude relaxation of correlated electrons," *Nature*, vol. 438, pp. 1135–1137, 2005.

[26] P. B. Allen, "Theory of thermal relaxation of electrons in metals," *Phys. Rev. Lett.*, vol. 59, pp. 1460–1463, 1987.

[27] J. Harris and G. S. Painter, "Oxygen chemisorption of a small aluminium cluster," *Phys. Rev. Lett.*, vol. 36, pp. 151–154, 1976.

[28] H. E. Johnson and C. M. Aikens, "Electronic structure and TDDFT optical absorption spectra of silver nanorods," *J. Phys. Chem. A*, vol. 113, pp. 4445–4450, 2009.

[29] D. J. Chadi and M. L. Cohen, "Special points in the brillouin zone," *Phys. Rev. B*, vol. 8, pp. 5747–5753, 1973.

[30] I. Campillo, J. M. Pitarke, A. Rubio, and P. M. Echenique, "Role of occupied d states in the relaxation of hot electrons in Au," *Phys. Rev. B*, vol. 62, pp. 1500–1503, 2000.

[31] H. Ehrenreich and H. R. Philipp, "Optical properties of Ag and Cu," *Phys. Rev.*, vol. 128, pp. 1622–1629, 1962.

[32] R. H. Ritchie, "Plasma losses by fast electrons in thin films," *Phys. Rev.*, vol. 106, pp. 874–881, 1957.

[33] P. B. Johnson and R. W. Christy, "Optical constants of the nobel metals," *Phys. Rev. B*, vol. 6, pp. 4370–4379, 1972.

[34] R. T. Beach and R. W.Christy, "Electron-electron scattering in the intraband optical conductivity of Cu, Ag, and Au," *Phys. Rev. B*, vol. 16, pp. 5277–5284, 1977.

[35] T.-C. Chiang, "Photoemission studies of quantum well states in thin films," *Surf. Sci. Rep.*, vol. 39, pp. 181–235, 2000.

[36] H. Duan, A. I. Fernàndez-Domìnguez, M. Bosman, S. A. Maier, and J. K. W. Yang, "Nanoplasmonics: Classical down to the nanometer scale," *Nano Lett.*, vol. 12, pp. 1683–1689, 2012.

[37] W. Ekardt, "Size-dependent photoabsorption and photoemission of small metal particles," *Phys. Rev. B*, vol. 31, pp. 6360–6370, 1985.

[38] W. Ekardt, "Work function of small metal particles: Self-consistent spherical jellium-background model," *Phys. Rev. B*, vol. 29, pp. 1558–1564, 1984.

[39] W. Ekardt, "Dynamical polarizability of small metal particles: Self-consistent spherical jellium background model," *Phys. Rev. Lett.*, vol. 52, pp. 1925–1928, 1984.

[40] J. Zuloaga, E. Prodan, and P. Nordlander, "Quantum plasmonics: Optical properties and tunability of metallic nanorods," *ACS Nano*, vol. 4, pp. 5269–5276, 2010.

[41] A. Zangwill and P. Stoven, "Density-functional approach to local-field effects in finite systems: Photoabsorption in the rare gases," *Phys. Rev. A*, vol. 21, pp. 1561–1571, 1980.

[42] E. Prodan and P. Norlander, "Structural tunability of the plasmon resonances in metallic nanoshells," *Nano Lett.*, vol. 3, pp. 543–547, 2003.

[43] B. Willingham and S. Link, "A Kirchhoff solution to metal nanoparticles," *submitted for review*, vol. xxx, pp. xxxx–xxxx, 2012.

[44] E. Prodan, C. Radloff, N. J. Halas, and P. Nordlander, "A hybridization model for the plasmon response of complex nanostructures," *Science*, vol. 302, pp. 419–422, 2003.

[45] M. L. Brongersma, J. W. Hartman, and H. A. Atwater, "Electromagnetic energy transfer and switching in nanoparticle chain arrays below the diffraction limit," *Phys. Rev. B*, vol. 62, pp. R16356–R16359, 2000.

[46] J. Aizpurua, G. W. Bryant, L. J. Richter, and F. J. Garcia de Abajo, "Optical properties of coupled metallic nanorods for field-enhanced spectroscopy," *Phys. Rev. B*, vol. 71, p. 235420, 2005.

[47] D. J. Bergman, "Dielectric constant of a two-component granular composite: A practical scheme for calculating the pole spectrum," *Phys. Rev. B*, vol. 19, pp. 2359–2368, 1979.

[48] P. Nordlander, C. Oubre, E. Prodan, K. Li, and M. I. Stockman, "Plasmon hybridization in nanoparticle dimers," *Nano Lett.*, vol. 4, pp. 899–903, 2004.

[49] D. E. Gómez, K. C.Vernon, and T. J. Davis, "Symmetry effects on the optical coupling between plasmonic nanoparticles with applications to hierarchical structures," *Phys. Rev. B*, vol. 81, p. 075414, 2010.

[50] M. I. Stockman, "Nanoplasmonics: The physics behind the applications," *Phys. Today*, vol. 64, pp. 39–44, 2011.

[51] L. C. Kennedy, L. R. Bickford, N. A. Lewinski, J. A. Coughlin, Y. Hu, E. S. Day, J. L. West, and R. A. Drezek, "A new era for cancer treatment: Gold-nanoparticle-mediated thermal therapies," *Small*, vol. 7, pp. 169–183, 2010.

[52] P. K. Jain, X. Huang, I. H. El-Sayed, and M. A. El-Sayed, "Noble metals on the nanoscale: Optical and photothermal properties and some applications in imaging, sensing, biology, and medicine," *Acc. Chem. Res.*, vol. 41, pp. 1578–1586, 2008.

[53] B. Khlebtsov, V. Zharov, A. Melnikov, V. Tuchin, and N. Khlebtsov, "Optical amplification of photothermal therapy with gold nanoparticles and nanoclusters," *Nanotechnology*, vol. 17, pp. 5167–5179, 2006.

[54] Y. Seol, A. E. Carpenter, and T. T. Perkins, "Gold nanoparticles: enhanced optical trapping and sensitivity coupled with significant heating," *Opt. Lett.*, vol. 31, pp. 2429–2431, 2006.

[55] Y. S. Joe, A. M. Satanin, and C. S. Kim, "Classical analogy of fano resonances," *Phys. Scr.*, vol. 74, pp. 259–266, 2006.

[56] D. A. Wells, "Application of the lagrangian equations to electrical circuits," *J. Appl. Phys.*, vol. 9, pp. 312–320, 1938.

[57] D. Pines and D. Bohm, "A collective description of electron interactions: II. collective vs individual particle aspects of the interactions," *Phys. Rev.*, vol. 85, pp. 338–353, 1952.

[58] J. M. Gèrardy and M. Ausloos, "Absorption spectrum of clusters of spheres from the general solution of maxwell's equations. The long-wavelength limit," *Phys. Rev. B*, vol. 22, pp. 4950–4959, 1980.

[59] M. Meier and A. Wokaun, "Enhanced fields on large metal particles: dynamic depolarization," *Opt. Lett.*, vol. 8, pp. 581–583, 1983.

[60] J. D. Jackson, *Classical Electrodynamics*. John Wiley & Sons, 2nd ed., 1975.

[61] J. C.-E. Sten, "Ellipsoidal harmonics and their application in electrostatics," *Journal of Electrostatics*, vol. 64, pp. 647–654, 2006.

[62] E. Prodan and P. Nordlander, "Plasmon hybridization in spherical nanoparticles," *J. Chem. Phys.*, vol. 120, pp. 5444–5454, 2004.

[63] B. Willingham, D. Brandl, and P. Nordlander, "Plasmon hybridization in nanorod dimers," *Appl. Phys. B: Lasers Opt.*, vol. 93, pp. 209–216, 2008.

[64] E. Hao and G. C. Schatz, "Electromagnetic fields around silver nanoparticles and dimers," *J. Chem. Phys.*, vol. 120, pp. 357–366, 2004.

[65] D. R. Fredkin and I. D. Mayergoyz, "Resonant behavior of dielectric objects (electrostatic resonances)," *Phys. Rev. Lett.*, vol. 91, p. 253902, 2003.

[66] L. S. Slaughter, W.-S. Chang, P. Swanglap, A. Tcherniak, B. P. Khanal, E. R. Zubarev, and S. Link, "Single-particle spectroscopy of gold nanorods beyond the quasi-static limit: Varying the width at constant aspect ratio," *J. Phys. Chem. C*, vol. 114, pp. 4934–4938, 2010.

[67] W. H. Weber and G. W. Ford, "Propagation of optical excitations by dipolar interactions in metal nanoparticle chains," *Phys. Rev. B*, vol. 70, p. 125429, 2004.

[68] J. A. Stratton, *Electromagnetic Theory*. Hoboken, New Jersey: John Wiley & Sons, Inc., 1941.

[69] J. M. Gèrardy and M. Ausloos, "Absorption spectrum of clusters of spheres from the general solution of maxwell's equations. ii. optical properties of aggregated metal spheres," *Phys. Rev. B*, vol. 25, pp. 4204–4229, 1982.

[70] J. A. Fan, C. Wu, K. Bao, J. Bao, R. Bardhan, N. J. Halas, V. N. Manoharan, P. Nordlander, G. Shvets, and F. Capasso, "Self-assembled plasmonic nanoparticle clusters," *Science*, vol. 328, pp. 1135–1138, 2010.

[71] M. I. Tribelsky, S. Flach, A. E. Miroshnickenko, A. V. Gorbach, and Y. S. Kivshar, "Light scattering by a finite obstacle and fano resonances," *Phys. Rev. Lett*, vol. 100, p. 043903, 2008.

[72] F. Hao, P. Nordlander, M. T. Burnett, and S. A. Maier, "Enhanced tunability and linewidth sharpening of plasmon resonances in hybridized metallic ring/disk nanocavities," *Phys. Rev. B*, vol. 76, p. 245417, 2007.

[73] F. Hao, P. Nordlander, Y. Sonnefraud, P. V. Dorpe, and S. A. Maier, "Tunability of subradiant dipolar and fano-type plasmon resonances in metallic ring/disk cavities: Implications for nanoscale optical sensing," *ACS Nano*, vol. 3, pp. 643–652, 2009.

[74] J. M. Reed, H. Wang, W. Hu, and S. Zou, "Shape of fano resonance line spectra calculated for silver nanorods," *Opt. Lett.*, vol. 36, pp. 4386–4388, 2011.

[75] J. Zhou, T. Koschny, M. Kafesaki, E. N. Economou, J. B. Pendry, and C. M. Soukoulis, "Saturation of the magnetic response of split-ring resonators at optical frequencies," *Phys. Rev. Lett.*, vol. 95, p. 223902, 2005.

[76] A. Alú, A. Salandrino, and N. Engheta, "Negative effective permeability and left-handed materials at optical frequencies," *Opt. Express*, vol. 14, pp. 1557–1567, 2006.

[77] S. N. Sheikholeslami, A. Garcìa-Etxarri, and J. A. Dionne, "Controlling the interplay of electric and magnetic modes via fano-like plasmon resonances," *Nano Lett.*, vol. 11, pp. 3927–3934, 2011.

[78] B. Willingham and S. Link, "Energy transport in metal nanoparticle chains via sub-radiant plasmon modes," *Opt. Express*, vol. 19, pp. 6450–6461, 2011.

[79] M. Liu, T.-W. Lee, S. K. Gray, P. Guyot-Sionnest, and M. Pelton, "Excitation of dark plasmons in metal nanoparticles by a localized emitter," *Phys. Rev. Lett.*, vol. 102, p. 107401, 2009.

[80] K. A. Willets, S. M. Stranahan, and M. L. Weber, "Shedding light on surface-enhanced raman scattering hot spots through single-molecule super-resolution imaging," *J. Phys. Chem. Lett.*, vol. 10, pp. 1286–1294, 2012.

[81] M. R. Jones, K. D. Osberg, R. J. Macfarlane, M. R. Langille, and C. A. Mirkin, "Templated techniques for the synthesis and assembly of plasmonic nanostructures," *Chem. Rev.*, vol. 111, pp. 3736–3827, 2011.

[82] C. A. Mirkin, R. L. Letsinger, R. C. Mucic, and J. J. Storhoff, "A DNA-based method for rationally assembling nanoparticles into macroscopic materials," *Nature*, vol. 382, pp. 607–609, 1996.

[83] A. S. Blum, C. M. Soto, C. D. Wilson, J. D. Cole, M. Kim, B. Gnade, A. Chatterji, W. F. Ochoa, T. W. Lin, J. E. Johnson, and B. R. Ratna, "Cowpea mosaic virus as a scaffold for 3-D patterning of gold nanoparticles," *Nano Lett.*, vol. 4, pp. 867–870, 2004.

[84] J. Henzie, J. Lee, M. H. Lee, W. Hasan, and T. W. Odom, "Nanofabrication of plasmonic stuctures," *Annu. Rev. Phys. Chem.*, vol. 60, pp. 147–165, 2009.

[85] L. Gunnarsson, T. Rindzevicius, J. Prikulis, B. Kasemo, M. Kall, S. Zou, and G. C. Schatz, "Confined plasmons in nanofabricated single silver particle pairs - experimental observations of strong interparticle interactions," *J. Phys. Chem. B*, vol. 109, pp. 1079–1087, 2005.

[86] B. P. Khanal and E. R. Zubarev, "Rings of nanorods," *Angew. Chem. Int. Ed.*, vol. 46, pp. 2195–2198, 2007.

[87] T. Ming, X. S. Kou, J. H. Chen, T. Wang, H. L. Tam, K. W. Cheah, J. Y. Chen, and J. F. Wang, "Ordered gold nanostructure assemblies formed by droplet evaporation," *Angew. Chem. Int. Ed.*, vol. 47, pp. 9685–9690, 2008.

[88] A. K. Boal, F. Ilhan, J. E. DeRouchey, T. Thurn-Albrecht, T. P. Russell, and V. M. Rotello, "Self-assembly of nanoparticles into structured spherical and network aggregates," *Nature*, vol. 404, pp. 746–748, 2000.

[89] L. J. E. Anderson, K. M. Mayer, R. D. Fraleigh, Y. Yang, S. Lee, and J. H. Hafner, "Quantitative measurements of individual gold nanoparticle scattering cross sections," *J. Phys. Chem. C*, vol. 114, pp. 11127–11132, 2010.

[90] D. Boyer, P. Tamarat, A. Maali, B. Lounis, and M. Orrit, "Photothermal imaging of nanometer-sized metal particles among scatterers," *Science*, vol. 297, pp. 1160–1163, 2002.

[91] A. Taflove and S. C. Hagness, *Computational Electrodynamics: The Finite-Difference Time Domain Method*. Norwood, MA: Artech House, INC., 2005.

[92] A. Dhawan, S. J. Norton, M. D.Gerhold, and T. Vo-Dinh, "Comparison of fdtd numerical computations and analytical multipole expansion method for plasmonics-active nanosphere dimers," *Opt. Express*, vol. 17, pp. 9688–9703, 2009.

[93] C. L. Nehl, N. K. Grady, G. P. Goodrich, F. Tam, N. J. Halas, and J. H. Hafner, "Scattering spectra of single gold nanoshells," *Nano Lett.*, vol. 4, pp. 2355–2359, 2004.

[94] W.-S. Chang, B. A. Willingham, L. S. Slaughter, B. P. Khanal, L. Vigderman, E. R. Zubarev, and S. Link, "Low absorption losses of strongly coupled surface plasmons in nanoparticle assemblies," *Proc. Nat. Acad. Sci. U.S.A.*, vol. 108, pp. 19879–19884, 2011.

[95] M. Moskovits and D. H. Jeong, "Engineering nanostructures for giant optical fields," *Chem. Phys. Lett.*, vol. 397, pp. 91–95, 2004.

[96] F. Le, D. W. Brandl, Y. A. Urzhumov, H. Wang, J. Kundu, N. J. Halas, J. Aizpurua, and P. Nordlander, "Metallic nanoparticle arrays: A common substrate for both surface-enhanced raman scattering and surface-enhanced infrared absorption," *ACS Nano*, vol. 2, pp. 707–718, 2008.

[97] C. J. Murphy, T. K. San, C. J. Orendorff, J. X. Gao, L. Gou, S. E. Hunyadi, and T. Li, "Anisotropic metal nanoparticles : synthesis, assembly, and optical applications," *J. Phys. Chem. B*, vol. 109, pp. 13857–13870, 2005.

[98] P. R. Evans, G. A. Wurtz, R. Atkinson, W. Hendren, D. O'Connor, W. Dickinson, R. J. Pollard, and A. V. Zayats, "Plasmonic coreshell nanorod arrays : subattoliter controlled geometry and tunable optical properties," *J. Phys. Chem. C*, vol. 111, pp. 12522–12527, 2007.

[99] B. N. Khlebtsov and N. G. Khlebtsov, "Multipole plasmons in metal nanorods: Scaling properties and dependence on particle size, shape, orientation, and dielectric environment," *J. Phys. Chem. C*, vol. 111, pp. 11516–11527, 2007.

[100] S. Link, M. B. Mohamed, and M. A. El-Sayed, "Simulation of the optical absorption spectra of gold nanorods as a function of their aspect ratio and the effect of the medium dielectric constant," *J. Phys. Chem. B*, vol. 103, pp. 3073–3077, 1999.

[101] F. Hao, C. L. Nehl, J. H. Hafner, and P. Nordlander, "Plasmon resonances of a gold nanostar," *Nano Lett.*, vol. 7, pp. 729–732, 2007.

[102] J. Aizpurua, G. W. Bryant, L. J. Richter, and F. J. G. de Abajo, "Optical properties of coupled metallic nanorods for field-enhanced spectroscopy," *Phys. Rev. B*, vol. 71, p. 235420, 2005.

[103] P. K. Jain, S. Eustis, and M. A. El-Sayed, "Plasmon coupling in nanorod assemblies: Optical absorption discrete dipole approximation simulation and exciton-coupling model," *J. Phys. Chem. B*, vol. 110, pp. 18243–18253, 2006.

[104] H. X. Xu, J. Aizpurua, M. Kall, and P. Apell, "Electromagnetic contributions to single-molecule sensitivity in surface-enhanced raman scattering," *Phys. Rev. E*, vol. 62, pp. 4318–4324, 2000.

[105] H. Wang, D. W. Brandl, P. Nordlander, and N. J. Halas, "Plasmonic nanostructures: Artificial molecules," *Acc. Chem. Res.*, vol. 40, pp. 53–62, 2007.

[106] D. W. Brandl and P. Nordlander, "Plasmon modes of curvilinear metallic core/shell particles," *J. Chem. Phys.*, vol. 126, p. 144708, 2007.

[107] M. L. Boas, *Mathematical methods in the physical sciences*. New York: John Wiley & Sons, 1983.

[108] D. W. Brandl, C. Oubre, and P. Nordlander, "Plasmon hybridization in nanoshell dimers," *J. Chem. Phys.*, vol. 123, p. 024701, 2005.

[109] W. Magnus, F. Oberhettinger, and R. P. Soni, *Formulas and Theorems for the Special Functions of Mathematical Physics*. New York: Springer, 1966.

[110] C. Oubre and P. Nordlander, "Finite-difference time-domain studies of the optical properties of nanoshell dimers," *J. Phys. Chem. B*, vol. 109, pp. 10042–10051, 2005.

[111] Y.-P. Wu and P. Nordlander, "Plasmon hybridization in nanoshells with a nonconcentric core," *J. Chem. Phys.*, vol. 125, p. 124708, 2006.

[112] P. K. Jain and M. A. El-Sayed, "Plasmonic coupling in noble metal nanostructures," *Chem. Phys. Lett.*, vol. 487, pp. 153–164, 2010.

[113] K. Li, X. Li, M. I. Stockman, and D. J. Bergman, "Surface plasmon amplification by stimulated emission in nanolenses," *Phys. Rev. B*, vol. 71, p. 115409, 2005.

[114] J. M. McMahon, S. K. Gray, and G. C. Schatz, "Nonlocal optical response of metal nanostructures with arbitrary shape," *Phys. Rev. Lett.*, vol. 103, p. 097403, 2009.

[115] J. Bosbach, C. Hendrich, F. Stietz, T. Vartanyan, and F. Träger, "Ultrafast dephasing of surface plasmon excitation in silver nanoparticles: Influence of particle size, shape, and chemical surrounding," *Phys. Rev. Lett.*, vol. 89, p. 257404, 2002.

[116] M. G. Blaber, A.-I. Henry, J. M. Bingham, G. C. Schatz, and R. P. V. Duyne, "LSPR imaging of silver triangular nanoprisms: Correlating scattering with structure using electrodynamics for plasmon lifetime analysis," *J. Phys. Chem. C*, vol. 116, pp. 393–403, 2012.

[117] A. Trügler, J.-C. Tinguely, J. R. Krenn, A. Hohenau, and U. Hohenester, "Influence of surface roughness on the optical properties of plasmonic nanoparticles," *Phys. Rev. B*, vol. 83, p. 081412, 2011.

[118] G. Dresselhaus, A. F. Kip, and C. Kittel, "Cyclotron resonance of electrons and holes in silicon and germanium crystals," *Phys. Rev.*, vol. 98, pp. 368–384, 1955.

[119] F. Hubenthal, C. Hendrich, and F. Träger, "Damping of the localized surface plasmon polariton resonance of gold nanoparticles," *Appl. Phys. B: Lasers Opt.*, vol. 100, pp. 225–230, 2010.

[120] N. Engheta, A. Salandrino, and A. Alù, "Cicuit elements at optical frequencies: Nanoinductors, nanocapacitors, and nanoresistors," *Phys. Rev. Lett.*, vol. 95, p. 095504, 2005.

[121] J. Zuloaga, E. Prodan, and P. Nordlander, "Quantum description of the plasmon resonances of a nanoparticle dimer," *Nano Lett.*, vol. 9, pp. 887–891, 2009.

[122] M. Dressel and M. Scheffler, "Verifying the drude response," *Ann. Phys.*, vol. 15, pp. 535–544, 2006.

[123] R. C. Jones, "A generalization of the dielectric ellipsoid problem," *Phys. Rev.*, vol. 68, pp. 93–96, 1945.

[124] A. Liebsch, "Surface plasmon dispersion of Ag," *Phys. Rev. Lett.*, vol. 71, pp. 145–148, 1993.

[125] A. O. Pinchuk, G. von Plessen, and U. Kreibig, "Influence of interband electronic transitions on the optical absorption in metallic nanoparticles," *J. Phys. D: Appl. Phys.*, vol. 37, pp. 3133–3139, 2004.

[126] J. A. Scholl, A. L. Koh, and J. A. Dionne, "Quantum plasmon resonances of individual metallic nanoparticles," *Nature*, vol. 483, pp. 421–427, 2012.

[127] V. V. Kresin, "Collective resonances in silver clusters: Role of d electrons and the polarization-free surface layer," *Phys. Rev. B*, vol. 51, pp. 1844–1849, 1995.

[128] R. Fuchs and F. Claro, "Multipolar response of small metallic spheres: Nonlocal theory," *Phys. Rev. B*, vol. 35, pp. 3722–3727, 1987.

[129] S. Raza, G. Toscano, A.-P. Jauho, M. Wubs, and N. A. Mortensen, "Unusual resonances in nanoplasmonic structures due to nonlocal response," *Phys. Rev. B*, vol. 84, p. 121412(R), 2011.

[130] B. B. Dasgupta and R. Fuchs, "Polarizability of a small sphere including nonlocal effects," *Phys. Rev. B*, vol. 24, pp. 554–561, 1981.

[131] R. Rojas and F. Claro, "Electromagnetic response of an array of particles: Normal-mode theory," *Phys. Rev. B*, vol. 34, pp. 3730–3736, 1986.

[132] W. L. Barnes, A. Dereux, and T. W. Ebbesen, "Suface plasmon subwavelength optics," *Nature*, vol. 424, pp. 824–830, 2003.

[133] J. A. Schuller, E. S. Barnard, W. Cai, Y. C. Jun, J. S. White, and M. L. Brongersma, "Plasmonics for extreme light concentration and manipulation," *Nat. Mater*, vol. 9, pp. 193–204, 2010.

[134] C. Dahmen, B. Schmidt, and G. von Plessen, "Radiation damping in metal nanoparticle pairs," *Nano Lett.*, vol. 7, pp. 318–322, 2007.

[135] A. O. Pinchuk and G. C. Schatz, "Nanoparticle optical properties: Far- and near-field electrodynamic coupling in a chain of silver spherical nanoparticles," *Mater. Sci. Eng. B*, vol. 149, pp. 251–258, 2008.

[136] K. L. Kelly, E. Coronado, L. L. Zhao, and G. C. Schatz, "The optical properties of metal nanoparticles: the influence of size, shape, and dielectric environment," *J. Phys. Chem. B*, vol. 107, pp. 668–677, 2003.

[137] S. A. Maier, P. G. Kik, and H. A. Atwater, "Observation of coupled plasmon-polariton modes in au nanoparticle chain waveguides of different lengths: Estimation of waveguide loss," *Appl. Phys. Lett.*, vol. 81, pp. 1714–1716, 2002.

[138] S. A. Maier, M. L. Brongersma, P. G. Kik, and H. A. Atwater, "Observation of near-field coupling in metal nanoparticle chains using far-field polarization spectroscopy," *Phys. Rev. B*, vol. 65, no. 19, p. 193408, 2002.

[139] M. D. Arnold, M. G. Blaber, M. J. Ford, and N. Harris, "Universal scaling of local plasmons in chains of metal spheres," *Opt. Express*, vol. 18, pp. 7528–7542, 2010.

[140] A. Kinkhabwala, Z. Yu, S. Fan, Y. Avlasevich, K. Müllen, and W. E. Moerner, "Large single-molecule fluorescence enhancements produced by a bowtie nanoantenna," *Nat. Photonics*, vol. 3, pp. 654–657, 2009.

[141] A. Sundaramurthy, K. B. Crozier, G. S. Kino, D. P. Fromm, P. J. Schuck, and W. E. Moerner, "Field enhancement and gap-dependent resonance in a system of two opposing tip-to-tip au nanotriangles," *Phys. Rev. B*, vol. 72, p. 165409, 2005.

[142] C. Sönnichsen, B. M. Reinhard, J. Liphardt, and A. P. Alivisatos, "A molecular ruler based on plasmon coupling of single gold and silver nanoparticles," *Nature Biotechnol*, vol. 23, pp. 741–745, 2005.

[143] K. L. Wustholz, A.-I. Henry, J. M. McMahon, R. G. Freeman, N. Valley, M. E. Piotti, M. J. Natan, G. C. Schatz, and R. P. V. Duyne, "Structure-activity relationships in gold nanoparticle dimers and trimers for surface-enhanced raman spectroscopy," *J. Am. Chem. Soc.*, vol. 132, pp. 10903–10910, 2010.

[144] B. M. Ross and L. P. Lee, "Comparison of near- and far-field measures for plasmon resonance of metallic nanoparticles," *Opt. Lett.*, vol. 34, pp. 896–898, 2009.

[145] B. Yan, S. V. Boriskina, and B. M. Reinhard, "Optimizing gold nanoparticle cluster configurations (n $<$ 7) for array applications," *J. Phys. Chem. C*, vol. 115, pp. 4578–4583, 2011.

[146] K. H. Fung and C. T. Chan, "Plasmonic modes in periodic metal nanoparticle chains: a direct dynamic eigenmode analysis," *Opt. Lett.*, vol. 32, pp. 973–975, 2007.

[147] A. A. Govyadinov and V. A. Markel, "From slow to superluminal propagation: Dispersive properties of surface plasmon polaritons in linear chains of metallic nanospheroids," *Phys. Rev. B*, vol. 78, p. 035403, 2008.

[148] A. Alù and N. Engheta, "Theory of linear chains of metamaterial/plasmonic particles as subdiffraction optical nanotransmission lines," *Phys. Rev. B*, vol. 74, p. 205436, 2006.

[149] A. F. Koenderink and A. Polman, "Complex response and polariton-like dispersion splitting in periodic metal nanoparticle chains," *Phys. Rev. B*, vol. 74, p. 033402, 2006.

[150] C. R. Simovski, A. J. Viitanen, and S. A. Tretyakov, "Resonator mode in chains of silver spheres and its possible application," *Phys. Rev. E*, vol. 72, p. 066606, 2005.

[151] D. S. Citrin, "Coherent excitation transport in metal nanoparticle chains," *Nano Lett.*, vol. 4, pp. 1561–1565, 2004.

[152] S. Y. Park and D. Stroud, "Surface-plasmon dispersion relations in chains of metallic nanoparticles: An exact quasistatic calculation," *Phys. Rev. B*, vol. 69, p. 125418, 2004.

[153] P. Nordlander, "Plasmonics: Subwavelength imaging in colour," *Nat. Photonics*, vol. 2, no. 1749-4885, pp. 387–388, 2008.

[154] C. Ropers, D. J. Park, G. Stibenz, G. Steinmeyer, J. Kim, D. S. Kim, and C. Lienau, "Femtosecond light transmission and subradiant damping in plasmonic crystals," *Phys. Rev. Lett.*, vol. 94, no. 11, p. 113901, 2005.

[155] D. S. Citrin, "Plasmon polaritons in finite-length metal-nanoparticle chains: the role of chain length unravelled," *Nano Lett.*, vol. 5, pp. 985–989, 2005.

[156] R. Fuchs, "Theory of the optical properties of ionic crystal cubes," *Phys. Rev. B*, vol. 11, pp. 1732–1740, 1975.

[157] R. Brako, "Optical properties of composite media," *J. Phys. C Solid State Phys.*, vol. 11, p. 3345, 1978.

[158] F. Claro, "Theory of resonant modes in particulate matter," *Phys. Rev. B*, vol. 30, pp. 4989–4999, 1984.

[159] N. Engheta, "Circuits with light at nanoscales: Optical nanocircuits inspired by metamaterials," *Science*, vol. 317, pp. 1698–1702, 2007.

[160] E. Ozbay, "Plasmonics: Merging photonics and electronics at nanoscale dimensions," *Science*, vol. 311, pp. 189–193, 2006.

[161] A. Alú and N. Engheta, "Hertzian plasmonic nanodimer as an efficient optical nano-antenna," *Phys. Rev. B*, vol. 78, p. 195111, 2008.

[162] N. A. Mirin, K. Bao, and P. Nordlander, "Fano resonances in plasmonic nanoparticle aggregates," *J. Phys. Chem. A*, vol. 113, pp. 4028–4034, 2009.

[163] M. Chandra, A.-M. Dowgiallo, and K. L. Knappenberger, "Controlled plasmon resonance properties of hollow gold nanosphere aggregates," *J. Am. Chem. Soc.*, vol. 132, pp. 15782–15789, 2010.

[164] J. A. Fan et. al, "Self-assembled plasmonic nanoparticle clusters," *Science*, vol. 328, pp. 1135–1138, 2010.

[165] Z. Nie et. al, "Self-assembly of metal-polymer analogues of amphiphilic triblock copolymers," *Nat. Mater.*, vol. 6, pp. 609–614, 2007.

[166] S. A. Maier, P. G. Kik, H. A. Atwater, S. Meltzer, E. Harel, B. E. Koel, and A. A. Requicha, "Local detection of electromagnetic energy transport below the diffraction limit in metal nanoparticle plasmon waveguides," *Nat. Mater.*, vol. 2, no. 1476-1122, pp. 229–232, 2003.

[167] S. Kawata, A. Ono, and P. Verma, "Subwavelength colour imaging with a metallic nanolens," *Nat. Photonics*, vol. 2, pp. 438–442, 2008.

[168] A. V. Malyshev, V. A. Malyshev, and J. Knoester, "Frequency-controlled localization of optical signals in graded plasmonic chains," *Nano Lett.*, vol. 8, pp. 2369–2372, 2008.

[169] M. Sukharev and T. Seidman, "Phase and polarization control as a route to plasmonic nanodevices," *Nano Lett.*, vol. 6, pp. 715–719, 2006.

[170] S. Zou and G. C. Schatz, "Metal nanoparticle array waveguides: Proposed structures for subwavelength devices," *Phys. Rev. B*, vol. 74, p. 125111, 2006.

[171] V. A. Markel and A. K. Sarychev, "Propagation of surface plasmons in ordered and disordered chains of metal nanospheres," *Phys. Rev. B*, vol. 75, p. 085426, 2007.

[172] Q.-H. Wei, K.-H. Su, S. Durant, and X. Zhang, "Plasmon resonance of finite one-dimensional au nanoparticle chains," *Nano Lett.*, vol. 4, pp. 1067–1071, 2004.

[173] K. B. Crozier, E. Togan, E. Simsek, and T. Yang, "Experimental measurement of the dispersion relations of the surface plasmon modes of metal nanoparticle chains," *Opt. Express*, vol. 15, pp. 17482–17493, 2007.

[174] A. F. Koenderink, R. de Waele, J. C. Prangsma, and A. Polman, "Experimental evidence for large dynamic effects on the plasmon dispersion of subwavelength metal nanoparticle waveguides," *Phys. Rev. B*, vol. 76, p. 201403, 2007.

[175] R. Quidant, C. Girard, J.-C. Weeber, and A. Dereux, "Tailoring the transmittance of integrated optical waveguides with short metallic nanoparticle chains," *Phys. Rev. B*, vol. 69, p. 085407, 2004.

[176] M. I. Stockman, S. V. Faleev, and D. J. Bergman, "Localization versus delocalization of surface plasmons in nanosystems: Can one state have both characteristics?," *Phys. Rev. Lett.*, vol. 87, p. 167401, 2001.

[177] J. J. Choquette, K.-P. Marzlin, and B. C. Sanders, "Superradiance, subradiance, and suppressed superradiance of dipoles near a metal interface," *Phys. Rev. A*, vol. 82, p. 023827, 2010.

[178] T. Kraus, L. Malaquin, H. Schmid, W. Riess, N. D. Spencer, and H. Wolf, "Nanoparticle printing with single-particle resolution," *Nat. Nanotechnol.*, vol. 2, pp. 570–576, 2007.

[179] G. Schider, J. R. Krenn, A. Hohenau, H. Ditlbacher, A. Leitner, F. R. Aussenegg, W. L. Schaich, I. Puscasu, B. Monacelli, and G. Boreman, "Plasmon dispersion relation of au and ag nanowires," *Phys. Rev. B*, vol. 68, p. 155427, 2003.

[180] H. Ditlbacher, A. Hohenau, D. Wagner, U. Kreibig, M. Rogers, F. Hofer, F. R. Aussenegg, and J. R. Krenn, "Silver nanowires as surface plasmon resonators," *Phys. Rev. Lett.*, vol. 95, p. 257403, 2005.

[181] R. M. Dickson and L. A. Lyon, "Unidirectional plasmon propagation in metallic nanowires," *J. Phys. Chem. B*, vol. 104, pp. 6095–6098, 2000.

[182] Y. Fang, Z. Li, Y. Huang, S. Zhang, P. Nordlander, N. J. Halas, and H. Xu, "Branched silver nanowires as controllable plasmon routers," *Nano Lett.*, vol. 10, pp. 1950–1954, 2010.

[183] B. D. Lubachevsky and F. H. Stillinger *J. Stat. Phys.*, vol. 60, p. 561, 1990.

[184] B. D. Lubachevsky, F. H. Stillinger, and E. N. Pinson *J. Stat. Phys.*, vol. 64, p. 501, 1991.

[185] T. Wriedt and A. Doicu *Appl. Opt.*, vol. 36, p. 2971, 1997.

[186] J. Renger, R. Quidant, N. van Hulst, S. Palomba, and L. Novotny, "Free-space excitation of propagating surface plasmon polaritons by nonlinear four-wave mixing," *Phys. Rev. Lett.*, vol. 103, p. 266802, 2009.

[187] S. Maier, *Plasmonics: Fundamentals and Applications*. New York: Springer, 2007.

[188] L. Levi, M. Rechtsman, T. Freedman, B. Schwartz, O. Manela, and M. Segev, "Disorder-enhanced transport in photonic quasicrystals," *Science*, vol. 332, pp. 1541–1544, 2011.